















## Physics-Based Simulation of the 2013 April 11 SEP Event

WEIHAO LIU <sup>1</sup>, IGOR V. SOKOLOV <sup>1</sup>, LULU ZHAO <sup>1</sup>, TAMAS I. GOMBOSI <sup>1</sup>, XIAOHANG CHEN <sup>1</sup>,  
NISHTHA SACHDEVA <sup>1</sup>, GÁBOR TÓTH <sup>1</sup>, WARD B. MANCHESTER IV <sup>1</sup>, DAVID LARIO <sup>2</sup>,  
KATHRYN WHITMAN <sup>3,4</sup>, ALESSANDRO BRUNO <sup>2,5</sup>, CHRISTINA M. S. COHEN <sup>6</sup>,  
M. LEILA MAYS <sup>2</sup> AND HAZEL M. BAIN <sup>7,8</sup>

<sup>1</sup>*Department of Climate and Space Sciences and Engineering, University of Michigan, Ann Arbor, MI 48109, USA*

<sup>2</sup>*Heliophysics Science Division, NASA Goddard Space Flight Center, Greenbelt, MD 20771, USA*

<sup>3</sup>*Space Radiation Analysis Group, NASA Johnson Space Center, Houston, TX 77058, USA*

<sup>4</sup>*KBR, Houston, TX 77002, USA*

<sup>5</sup>*Department of Physics, Catholic University, Washington, DC 20064, USA*

<sup>6</sup>*California Institute of Technology, Pasadena, CA 91125, USA*

<sup>7</sup>*Cooperative Institute for Research In Environmental Sciences, University of Colorado Boulder, Boulder, CO 80309, USA*

<sup>8</sup>*NOAA Space Weather Prediction Center, Boulder, CO 80305, USA*

Submitted to ApJ

### ABSTRACT

Solar energetic particles (SEPs) can pose hazardous radiation risks to both humans in space and spacecraft electronics. Numerical modeling based on first principles offers valuable insights into SEPs, providing synthetic observables for SEPs at any time and location in space. In this work, we present a high-resolution scheme based on integral relations for Poisson brackets to solve the kinetic equation for particle acceleration and transport processes. We implement this scheme within the Space Weather Modeling Framework (SWMF), developed at the University of Michigan, to conduct a comprehensive study of solar energetic protons during the 2013 April 11 SEP event. In addition, a shock capturing tool is developed to study the coronal-mass-ejection-driven shock starting from the low solar corona. Multi-point spacecraft observations, including *SOHO/ERNE*, *SDO/AIA*, *GOES* and *ACE* at Earth, and *STEREO-A/B*, are used for model-data comparison and validation. New synthetic observables such as white-light images, shock geometry and properties, as well as SEP intensity-time profiles and spectra provide insights for SEP studies. The influences of the mean free path on SEP intensity-time profiles and spectra are also discussed. The results demonstrate: (1) the successful implementation of the Poisson bracket scheme with a self-consistent particle tracker within the SWMF, (2) the capability of capturing the time-evolving shock surface in the SWMF, and (3) the complexity of the mean free path impacts on SEPs. Overall, this study contributes to both scientific research and operational objectives by

advancing our understanding of particle behaviors and showing the readiness for more accurate SEP predictions.

*Keywords:* Solar energetic particles (1491), Solar coronal mass ejection shocks (1997), Heliosphere (711), Space weather (2037), Computational methods (1965)

## 1. INTRODUCTION

Solar energetic particles (SEPs) consist of protons, heavier ions, and electrons, originating from the Sun, and accelerated over a wide range of energies ranging from suprathermal (a few keVs) up to relativistic (a few GeVs) energies (Reames 1999, 2021; Klein & Dalla 2017). Generally, the SEP events can be classified as impulsive or gradual ones (Cane et al. 2006; Reames 2013). Impulsive SEP events are believed to be associated with the magnetic reconnection within solar flares, whose intensity-time profiles show an impulsive onset and a fast decay with a duration typically less than one day (e.g., Nitta et al. 2006; Mason 2007; Bučík 2020). On the other hand, shock acceleration by coronal-mass-ejection- (CME) driven shocks is responsible for widespread and large gradual SEP events (Kahler et al. 1978, 1984; Desai & Giacalone 2016), typically lasting for a few days and potentially causing significant radiation hazards (e.g., Aschwanden 2012; Miroshnichenko 2018; Cliver et al. 2022).

The diffusive shock acceleration (DSA), also called first-order Fermi acceleration (Fermi 1949), is believed to be the primary acceleration mechanism producing energetic particles in many heliophysics and astrophysical systems (e.g., Axford et al. 1977; Krymskii 1977; Bell 1978a,b; Blandford & Ostriker 1978; Blandford & Eichler 1987; Jokipii 1982, 1987; Armstrong et al. 1985; Zank et al. 2000; Petrosian 2012). Particles can get accelerated as they travel across the shock front with strong plasma compressions (see Chapter 13.4.2 of Gombosi 1998, and the references therein). This acceleration process can naturally lead to a universal power-law momentum distribution  $f(p) \propto p^{-\gamma}$ , where  $f$  is the omni-directional distribution function and  $p$  denote the particle momentum. The power-law index  $\gamma$  is only dependent on the shock compression ratio, i.e., the ratio of the plasma downstream density to the upstream one (Drury 1983; Jones & Ellison 1991; Melrose & Pope 1993; Sokolov et al. 2006b; Giacalone & Neugebauer 2008). Furthermore, there is usually an exponential rollover in SEP energy spectra, which shows a double power-law feature (Ellison & Ramaty 1985; Band et al. 1993), with the break energy depending on the ion charge-to-mass ratio (e.g. Cohen et al. 2005; Mewaldt et al. 2005; Tylka et al. 2005; Li et al. 2009; Yu et al. 2022). It is suggested by, e.g. Zhao et al. (2016b, 2017); Kong et al. (2019), that the probable explanations are the shock finite lifetimes and sizes for particle acceleration, as well as the adiabatic cooling effect during particle transport.

CMEs, especially the fast ones, can drive shock waves propagating through the solar corona (SC) (Sime & Hundhausen 1987; Vourlidis et al. 2003), which sometimes can survive to a large radial distance up to many astronomical units (AUs) from the Sun (Chen 2011; Webb & Howard 2012). As the shock wave propagates across SC and through the interplanetary (IP) medium, it may continue accelerating particles from the ambient plasma or from contiguous and/or previous solar events (e.g., Gopalswamy et al. 2002; Rouillard et al. 2011; Luhmann et al. 2020). Multi-spacecraft observations have shown that the time-intensity profiles of SEP events often exhibit significant variations at widely separated heliospheric locations (e.g. Lario et al. 2016, 2017a), which suggests the significance of the magnetic connectivity between the observers and the shock wave front (see Lario et al. 2013, 2017b, 2020; Chen et al. 2022; Zhao 2023, and references therein). Finally, these energetic particles

can propagate through the SC and IP space and reach the Earth, posing risky radiation threats to astronauts in space, passengers and crew on flights, as well as spacecraft electronics and instruments (Jones et al. 2005; Zheng et al. 2019; Guo et al. 2021, 2024; Buzulukova & Tsurutani 2022; Fogtman et al. 2023; Jun et al. 2024). Therefore, a better understanding of the acceleration and transport of SEPs and the capability of accurate predictions of the radiation hazard caused by SEPs, particularly the protons due to their dominating abundances (e.g., Mewaldt 2006; Xapsos et al. 2007; Schmelz et al. 2012), become critical to human endeavor for deep space exploration.

In order to investigate the underlying physics of SEPs, and anticipate and assess the potential risks they pose on space exploration, numerous SEP models have been developed to provide statistical and/or numerically modeled predictions of the energetic particle properties. A recent review by Whitman et al. (2023) summarizes a multitude of SEP models developed by the community of predicting the SEP event occurrence probability and/or properties. These SEP models can be classified as empirical models, machine-learning (ML) models, and physics-based models. Empirical models are often grounded on correlations with the observational data, and can offer quick predictions with the fitted formulas or pre-existing relations (e.g., Posner 2007; Balch 2008; Falconer et al. 2011, 2014; Dierckxsens et al. 2015; Anastasiadis et al. 2017; Richardson et al. 2018; Bruno & Richardson 2021; Papaioannou et al. 2022). ML models are built upon potential causality relations between the observables and predictable. Based on the theories in probability and statistics, there is a variety of ML algorithms and models developed nowadays (e.g., Laurenza et al. 2009; Núñez 2011; Boubrahimi et al. 2017; Lavasa et al. 2021; Kasapis et al. 2022, 2024; Baydin et al. 2023; Chatterjee et al. 2024; Hosseinzadeh et al. 2024), which may provide fast and robust predictions. However, such models lack the underlying physics and are mostly data-driven, with restrictions of energy channels and also large uncertainties for the predicted SEP flux and/or event occurrence probability in realistic practice. The quality of the data used to develop the empirical and ML models can even impact the performance of these models, and it is hard for these models to predict and validate the SEP properties at locations in space where no spacecraft has ever traveled to (see Whitman et al. 2023; Chen et al. 2024b, for more details).

On the other hand, the physics-based models are developed based on the first principles in physics and different kinds of sophisticated computational techniques (e.g., Ng & Reames 1994; Ng et al. 2003; Sokolov et al. 2004; Kóta et al. 2005; Aran et al. 2006; Luhmann et al. 2007; Zhang et al. 2009; Dröge et al. 2010; Strauss & Fichtner 2015; Hu et al. 2017; Zhang & Zhao 2017; Borovikov et al. 2018; Linker et al. 2019; Wei et al. 2019; Wijzen et al. 2019; Li et al. 2021; Tenishev et al. 2021; Zhang et al. 2023; Palmerio et al. 2024; Zhao et al. 2024). These models leverage our current understanding of particle acceleration and transport in the SC and IP space to analyze the properties associated with SEP events. They are usually computationally expensive to obtain meaningful results, and need much attention and efforts in model validation and evaluations (Bain et al. 2023; Zheng et al. 2024). Moreover, there are still a lot of challenges and open questions for SEP modeling as reported by Anastasiadis et al. (2019), such as the underlying physical mechanisms (e.g., Giacalone 2005a,b; Lee et al. 2012; Verkhoglyadova et al. 2015), suprathermal seed particles injected into acceleration processes (e.g., Li et al. 2012; Ding et al. 2015; Zhuang et al. 2021; Wijzen et al. 2023a), and the interaction of energetic particles with the turbulent magnetic field in heliosphere (e.g., Giacalone et al. 2000; Zank et al. 2014; Engelbrecht 2019; Shalchi 2020). In spite of high demands of computational resources and techniques to strive for meaningful results, the physical-based models are still attractive

in the community, since these models are able to provide synthetic observables such as the shock properties, and the time profiles and energy spectra of SEPs at any time and location of interest in SC and the inner heliosphere (IH). These synthetic observables can offer a unique insight to analyze the SEP events and interpret the underlying physics, advancing our knowledge of particle acceleration and transport processes.

The structure of the paper is as follows. In Section 2, we describe our numerical models in details, including the magnetohydrodynamics (MHD) code to simulate the solar wind plasma, the CME flux rope initialization tool, and in particular, our SEP model setup, with a newly implemented scheme that proves to be more computationally efficient. Subsequently, an overview of the SEP event investigated in this work, the 2013 April 11 SEP event, is introduced in Section 3. By means of the numerical modeling tools, we simulate the solar energetic protons during this event. Notably, we have developed a shock capturing tool and leveraged this tool to investigate the shock evolution in this event. In Section 4, we show our simulation results and conduct model-data comparisons in depth by providing different kinds of observables. In Section 5, we further discuss the discrepancy between our model results and the observational data. Results and conclusions are finally summarized in Section 6.

## 2. METHODOLOGY

In order to simulate SEPs by a physics-based model, we need to have modules to simulate the background solar wind, CME generation and propagation, and the particle acceleration and transport processes. In this study, we employ the Space Weather Modeling Framework (SWMF<sup>1</sup>) developed at the University of Michigan, which provides a high-performance computational capability to simulate the space weather environment from the upper solar chromosphere to the Earth’s upper atmosphere and/or the outer heliosphere (Tóth et al. 2005, 2012; Gombosi et al. 2021). The SWMF has integrated various components that represent different physical domains of the space environment, each offering several models available. Our focus here is on the SC and IH components for a 3D global solar wind simulations, the Eruptive Event generator (EE) for the CME study, and the particle acceleration and transport model for SEPs.

### 2.1. Background Solar Wind

The three-dimensional (3D) global solar wind plasma across both the SC (from 1 to 24 solar radii,  $R_s$ ) and IH (from 24 to 500  $R_s$ ) regions is modeled by the Alfvén Wave Solar-atmosphere Model(-Realtime) (AWSoM-R, van der Holst et al. 2010, 2014; Oran et al. 2013; Gombosi et al. 2018; Sokolov et al. 2013, 2021, 2022). The AWSoM-R is an Alfvén wave-driven and self-consistent solar atmosphere model and has been validated by comparing simulations and observations of both the *in-situ* macroscopic properties of the solar wind and the line-of-sight appearance of the corona observed in different wavelengths (e.g., Jian et al. 2015; Meng et al. 2015; Sachdeva et al. 2019, 2021, 2023; van der Holst et al. 2019, 2022; Shi et al. 2022). In AWSoM-R, the Block-Adaptive-Tree-Solarwind-Roe-Upwind-Scheme (BATS-R-US) code plays a critical role in solving the MHD equations that describe the plasma dynamics (Powell et al. 1999). The steady-state solar wind solution is obtained with the local time stepping and second-order shock-capturing scheme (Tóth et al. 2012). The inner boundary condition of the magnetic field is specified by solar magnetograms. In this study, we use

<sup>1</sup> <https://github.com/SWMFsoftware>

the synoptic magnetograms collected by the Global Oscillation Network Group of the National Solar Observatory (NSO/GONG<sup>2</sup>, Harvey et al. 1996; Hill 2018).

However, because of the limitations of the observed geometry, there can be a significant uncertainty of the radial magnetic field measurements in the polar regions (e.g., Petrie 2015; Reiss et al. 2023). In order to reduce this uncertainty and achieve better agreement of the global simulation results with observations, it is customary to modify the photospheric radial magnetic field in the polar regions (e.g., Nikolić 2019; Sokolov & Gombosi 2023; Huang et al. 2024b). Specifically, the GONG-observed radial field,  $B_r^{\text{GONG}}$ , used as the boundary condition at  $r = R_s$ , is intensified in the weak-field regions:

$$B_r|_{r=R_s} = \text{sign}(B_r^{\text{GONG}}) \times \min(3.75 |B_r^{\text{GONG}}|, |B_r^{\text{GONG}}| + 5 \text{ Gs}). \quad (1)$$

Figure 1(a) shows the processed-GONG magnetogram as of 2013 April 11 06:04 UT, as the input for AWSoM-R in SWMF. To get a 3D distribution of the strapping field configuration, the Potential Field Source Surface (PFSS, Altschuler & Newkirk 1969; Schatten et al. 1969) model is applied to express the intensified field as a series of spherical harmonics to the order of 180 in this study (Tóth et al. 2011).

In AWSoM-R, the coronal plasma is heated by the dissipation of two discrete turbulence populations that propagate parallel and antiparallel to the magnetic field (Sokolov et al. 2013). By using physically consistent treatments of wave reflection, dissipation, and heat partitioning between electrons and protons, the AWSoM-R has been showed the capability to realistically reproduce the solar corona with only three free parameters: the Poynting flux parameter for the energy input ( $S_A/B$ ), correlation length for Alfvén wave dissipation ( $L_\perp \sqrt{B}$ ), and the stochastic heating exponent and amplitude ( $h_S, A_S$ ) (Fisk & Schwadron 2001; Chandran et al. 2011; Sokolov et al. 2013; van der Holst et al. 2014; Hoppock et al. 2018). A recent study by Huang et al. (2024b) utilized the GONG magnetograms and explored various parameter sets over an entire solar cycle for solar wind uncertainty quantification in numerical modeling. Building on their findings, we adopt the optimal parameters determined following the methodologies outlined in Huang et al. (2023, 2024b); Jivani et al. (2023):  $S_A/B = 0.3 \text{ MW m}^{-2} \text{ T}^{-1}$ ,  $L_\perp \sqrt{B} = 1.5 \times 10^5 \text{ m T}^{1/2}$ , and  $(h_S, A_S) = (0.21, 0.18)$ . These parameters are employed to simulate the steady-state solar wind for the 2013 April 11 event of our interest.

As known, a validated background solar wind solution is essential for modeling the transport processes of energetic particles, as it provides the magnetic field configuration where particles propagate, thereby enabling the computation of the energetic particle properties observed by spacecraft at specific heliospheric locations (e.g., Hinterreiter et al. 2019; Jin et al. 2022; Zhao et al. 2024). Nevertheless, current numerical solutions of the ideal or resistive MHD equations have struggled to reproduce the aligned interplanetary stream lines and magnetic field lines in corotating frames. One of the reasons for this discrepancy is the numerical reconnection across the heliospheric current sheet (HCS): the reconnected field is directed across the HCS, while the global solar wind streams along the HCS, thus resulting in the “V-shaped” magnetic field lines and significant misalignment between the magnetic field lines and stream lines (e.g., Brchneleva et al. 2022; Sokolov et al. 2022). It is unfeasible to follow the trajectory of particles in such “V-shaped” magnetic field lines, and thus, stream lines are usually used instead (e.g., Young et al. 2021). Recently, Sokolov et al. (2022) has introduced the stream-aligned MHD method that “nudges” the magnetic field lines and plasma stream

<sup>2</sup> <https://gong.nso.edu/data/magmap/>

lines to restore their alignments. Further details can be found in Sokolov et al. (2022), and this stream-aligned AWSoM-R model has recently been validated in steady-state solar wind simulations by Wraback et al. (2024); Zhao et al. (2024). In this study, we utilize the stream-aligned AWSoM-R model to obtain a steady-state solar wind plasma background where CMEs and SEPs propagate.

## 2.2. Eruptive Event Generator

With the steady-state solar wind simulation results, the CME flux rope is then generated by the EE module in SWMF, which has been extensively used and validated to model the CME initialization and propagation (e.g., Manchester IV et al. 2004a,b,c, 2006, 2008, 2014a,b; Lugaz et al. 2005a,b, 2007, 2013; Kataoka et al. 2009; van der Holst et al. 2009; Jin et al. 2013, 2016, 2017a,b; Shiota & Kataoka 2016; Kilpua et al. 2019). Currently, there are a few different flux rope models embedded into the EE module, such as the breakout model (Antiochos et al. 1999), the flux-emergence model (e.g. Manchester IV et al. 2004a), and the analytical flux rope model including the Gibson-Low flux rope (GL, Gibson & Low 1998), and the Titov-Démoulin flux rope (Titov & Démoulin 1999; Roussev et al. 2003; Titov et al. 2014, 2022; Sokolov & Gombosi 2023) with the STatistical InjecTIon of Condensed Helicity (STITCH) initialization mechanism (Antiochos 2013; Dahlin et al. 2022).

In this study, we use the spheromak-type magnetic field configuration anchored to the inner boundary adopting the Gibson-Low model for the initial condition to initiate the flux rope, which is called the Eruptive Event Generator Gibson-Low configuration (EEGGL<sup>3</sup>, e.g., Gibson & Low 1998; Borovikov et al. 2017; Jin et al. 2017a,b). The processed-GONG magnetogram shown in Figure 1(a), the active region (AR) location, and the observed CME speed, from Coordinated Data Analysis Web (CDAW) catalog<sup>4</sup> (Yashiro et al. 2004; Gopalswamy et al. 2009) and/or the Space Weather Database Of Notifications, Knowledge, Information (DONKI) database<sup>5</sup>, are used to calculate the GL flux rope parameters. Figure 1(b) shows the zoomed-in AR field with the chosen locations for filament footpoints as well as the polarity inversion line (PIL) identified by EEGGL. In addition, EEGGL can offer an efficient parameter setup for CME initiation based on empirical features of pre-event conditions (e.g., Borovikov et al. 2017; Gombosi et al. 2021; Zhao et al. 2024), as shown in Figure 1(c). With the force-imbalanced flux rope initialized by EEGGL and inserted on top of the AR, the CME propagation in the SC and IH components are subsequently modeled using stream-aligned AWSoM-R with time-accurate simulations (Sokolov et al. 2022).

## 2.3. Particle Solver

### 2.3.1. Governing Equation

As SEP population forms a suprathermal tail of particle distribution in the solar wind, whose distribution is far from the Maxwellian (e.g., Pierrard & Lazar 2010; Kahler & Ling 2019; Lario et al. 2019), we characterize SEPs by a canonical distribution function  $F(\mathbf{r}, \mathbf{p}, t)$  of coordinates,  $\mathbf{r}$ , and momentum,  $\mathbf{p}$ , and time,  $t$ , such that the number of particles,  $dN$ , within the elementary volume,  $d^3\mathbf{r}$ , is given by the following normalization integral:  $dN = d^3\mathbf{r} \int d^3\mathbf{p} F(\mathbf{r}, \mathbf{p}, t)$ . In a magnetized moving plasma, it is convenient to consider the distribution function at any given point,  $\mathbf{r}$ , in a frame of reference moving with the local plasma velocity,  $\mathbf{u}(\mathbf{r}, t)$ . Also, we introduce the spherical coordinates ( $p = |\mathbf{p}|, \mu = \mathbf{b} \cdot \mathbf{p}/p, \varphi$ ) in the momentum space with its polar axis aligned with the

<sup>3</sup> Available on <https://github.com/SWMFsoftware> and <https://ccmc.gsfc.nasa.gov/analysis/EEGGL/>.

<sup>4</sup> [https://cdaw.gsfc.nasa.gov/CME\\_list/](https://cdaw.gsfc.nasa.gov/CME_list/)

<sup>5</sup> <https://kauai.ccmc.gsfc.nasa.gov/DONKI/search/>

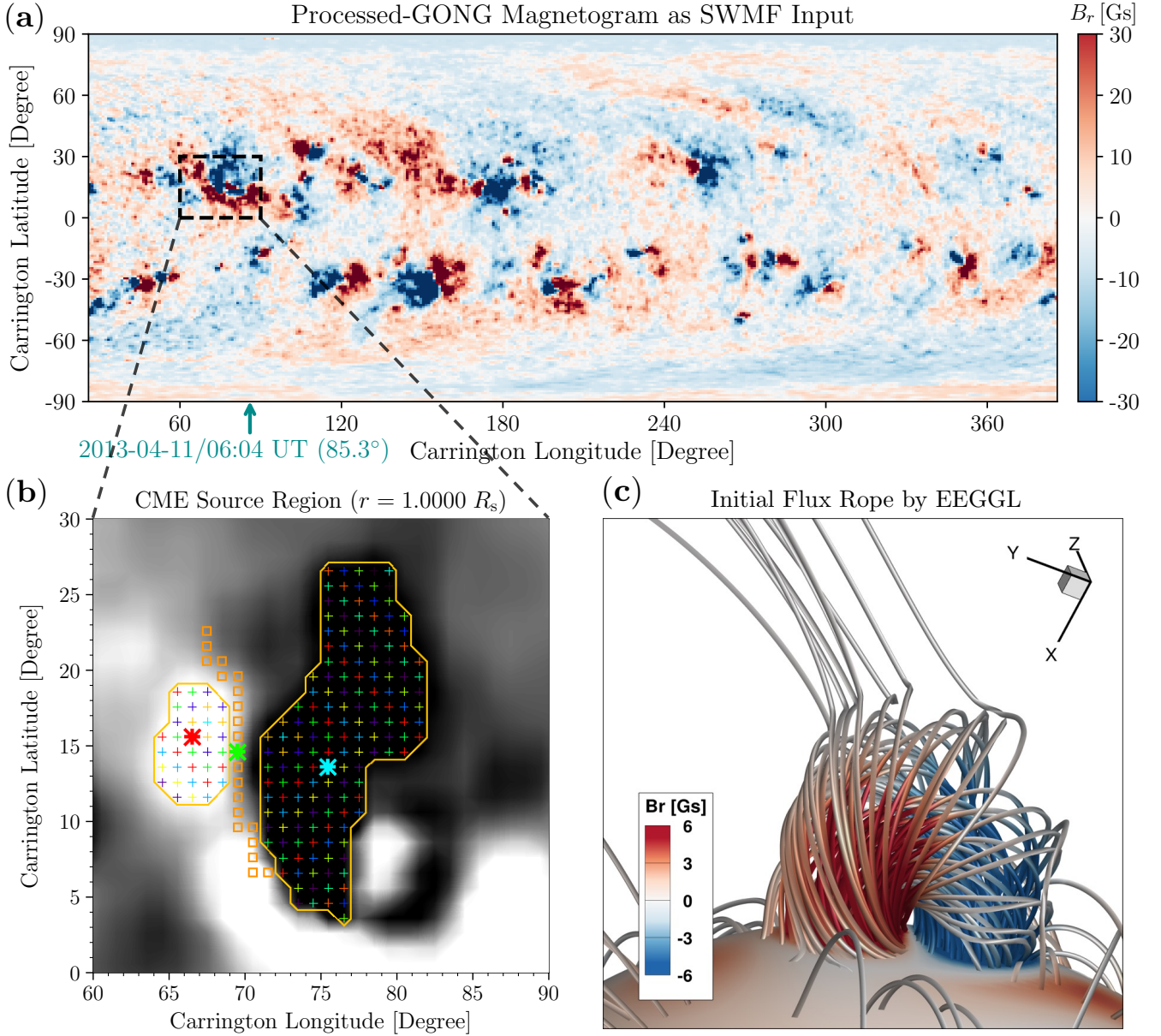


**Figure 1.** (a): Processed-GONG magnetogram as of 2013 April 11 06:04 UT, with the green arrow representing the Carrington longitude of the Earth. The magnetogram region  $60^\circ$  eastward of the green arrow remains unchanged from the previous Carrington rotation. Weak magnetic fields in the original GONG magnetogram have been enhanced as described by Equation 1. The black dashed box shows the area as the CME source region for EEGGL. (b): Zoomed-in AR field at the inner boundary,  $r = 1.0000 R_s$ . The red and blue asterisks indicate the chosen locations for the current filament positive and negative footpoints, respectively, and the green asterisk indicates the center of the configuration. A series of orange squares denote the polarity inversion line. (c): The 3D topology of the flux rope initialized by EEGGL, superposed with the radial magnetic field of the AR adjusted to simulate the CME event of 2013 April 11.

direction,  $\mathbf{b} = \mathbf{B}/B$ , of the magnetic field,  $\mathbf{B}(\mathbf{r}, t)$ . Here,  $B$  denotes the magnetic field amplitude ( $= |\mathbf{B}(\mathbf{r}, t)|$ ), and  $\mu$  is the cosine value of pitch angle. The normalization integral in these new

variables finally gives:

$$dN = d^3\mathbf{r} \int_0^{+\infty} p^2 dp \int_{-1}^1 d\mu \int_0^{2\pi} d\varphi F(\mathbf{r}, p, \mu, \varphi, t). \quad (2)$$

Using the canonical distribution function, one can define a gyrotropic distribution function,  $\mathcal{F}(\mathbf{r}, p, \mu, t) = \frac{1}{2\pi} \int_0^{2\pi} d\varphi F(\mathbf{r}, p, \mu, \varphi, t)$ , to describe the particle motion averaged over the phase of gyration about the magnetic field. The isotropic (omni-directional) distribution function,  $f(\mathbf{r}, p, t) = \frac{1}{2} \int_{-1}^1 d\mu \mathcal{F}(\mathbf{r}, p, \mu, t)$  is additionally averaged over the pitch angle. The normalization integrals in Equation 2 becomes:

$$\begin{aligned} dN &= 2\pi d^3\mathbf{r} \int_0^{+\infty} p^2 dp \int_{-1}^1 d\mu f(\mathbf{r}, p, t) \\ &= 4\pi d^3\mathbf{r} \int_0^{+\infty} p^2 dp f(\mathbf{r}, p, t). \end{aligned} \quad (3)$$

The kinetic equation for the isotropic part of the distribution function,  $f(\mathbf{r}, p, t)$ , was introduced in Parker (1965):

$$\frac{\partial f}{\partial t} = \underbrace{-\mathbf{u} \cdot \nabla f}_{\text{Advection}} + \underbrace{\nabla \cdot (\overset{\leftrightarrow}{\kappa} \cdot \nabla f)}_{\text{Diffusion}} + \underbrace{\frac{1}{3} (\nabla \cdot \mathbf{u}) \frac{\partial f}{\partial \ln p}}_{\text{Adiabatic Term}} + \underbrace{Q}_{\text{Additional Source/Sink}}, \quad (4)$$

where  $\overset{\leftrightarrow}{\kappa} = D_{xx} \mathbf{b}\mathbf{b}$  is the tensor of parallel diffusion along the magnetic field,  $D_{xx}$  is the parallel diffusion coefficient, and  $Q$  denotes the additional acceleration source or sink terms. The term proportional to the divergence of  $\mathbf{u}$  accounts for the adiabatic cooling for  $\nabla \cdot \mathbf{u} > 0$ , or the first-order Fermi acceleration in compression or shock waves or  $\nabla \cdot \mathbf{u} < 0$  (Fermi 1949). As the transport equation in Equation 4 captures the effects of IMF and IP plasma properties on the SEP acceleration and transport processes, we will use Equation 4 for the SEP numerical modeling in this study.

### 2.3.2. M-FLAMPA

In SWMF, the Multiple Field-Line-Advection Model for Particle Acceleration (M-FLAMPA, Sokolov et al. 2004; Borovikov et al. 2018, 2019) has been developed to simulate the particle acceleration and transport processes, where the particles are accelerated at the shocks driven by CMEs through the first-order Fermi acceleration mechanism (Fermi 1949). With no loss in generality, M-FLAMPA reduces a 3D problem of particle propagation in the IMF to a multitude of simpler 1D problems of the particle transport along a single line of the IMF. As the simulation begins, AWSoM-R and M-FLAMPA run simultaneously. At each time step, the time-evolving magnetic field lines, as well as the plasma properties, are extracted from the stream-aligned AWSoM-R solutions, along which the particle distribution function is solved (Borovikov et al. 2015, 2018). Moreover, as proposed by Sokolov et al. (2004), novel mathematical approaches are applied to the extracted magnetic field lines to sharpen the shock geometry, enhancing the efficiency of the DSA process.

In M-FLAMPA, the particles are assumed to couple with the magnetic field lines. The motion of the particles consist of the displacement of the particle's guiding center along the IMF lines, and the joint advection of both the guiding center and the IMF line together with plasma where the magnetic field is frozen. Mathematically, this method employs the Lagrangian coordinate,  $\mathbf{R}_L$ , which stays



with the advecting fluid elements in space (Landau & Lifshitz 1987). Herewith, the partial time derivative at the constant Lagrangian coordinate,  $\mathbf{r}_L$ , and time,  $\tau$ , is denoted as  $\frac{d}{dt}$  or  $\frac{\partial}{\partial \tau}$ , while the notation  $\frac{\partial}{\partial t}$  denotes the partial time derivative at the constant Eulerian coordinate,  $\mathbf{r}$ , with the relations:  $\frac{\partial}{\partial \tau} = \frac{d}{dt} = \frac{\partial}{\partial t} + \mathbf{u} \cdot \nabla$ . Certain terms in Equation 4 can be expressed in term of the Lagrangian derivatives and spatial derivative along lines, combining the plasma motion equations. Equation 4 can be eventually rewritten as (Borovikov et al. 2018, 2019; Sokolov et al. 2023):

$$\frac{\partial f}{\partial \tau} = \frac{df}{dt} = -\frac{1}{3} \frac{D \ln \rho}{Dt} \frac{\partial f}{\partial \ln p} + \nabla \cdot \left( \overset{\leftarrow}{\kappa} \cdot \nabla f_0 \right) + Q, \quad (5)$$

where  $\rho$  is the mass density of the plasma.

In addition, the Strang splitting method (e.g., Strang 1968; MacNamara & Strang 2016) is applied in M-FLAMPA to split the advection and diffusion terms, in order to solve Equation 5 efficiently in M-FLAMPA. Here, we implement high-resolution Poisson bracket scheme for advectations (Sokolov et al. 2023) and use the theoretical derivations for the diffusion coefficient based on the quasi-linear theory (QLT, Jokipii 1966) and the turbulent magnetic field (see Li et al. 2003; Sokolov et al. 2004; Borovikov et al. 2019, and references therein). More details are demonstrated later in Sections 2.3.3 and 2.3.4, respectively.

### 2.3.3. High-Resolution Poisson Bracket Scheme

In order to simulate the fluxes of shock-accelerated SEPs, we are going to solve the kinetic equation throughout the whole computational domain including the shock wave region through DSA processes as a part of our SEP model. In this case, it is important to use a particle conserving scheme. Otherwise, the prediction for the SEP flux may be contaminated by the fake particle productions due to approximation errors at high spatial gradients at the shock.

In classical physics (Landau & Lifshitz 1987), with  $H$  being the Hamiltonian function, the Poisson bracket for the distribution function,  $f$ , is introduced as:

$$\{f; H\} \equiv \sum_{\ell} \{f; H\}_{q_{\ell}, p_{\ell}} = \sum_{\ell} \left( \frac{\partial f}{\partial q_{\ell}} \frac{\partial H}{\partial p_{\ell}} - \frac{\partial H}{\partial q_{\ell}} \frac{\partial f}{\partial p_{\ell}} \right), \quad (6)$$

in which  $p_{\ell}$  and  $q_{\ell}$  are the canonical coordinates for momentum and position, respectively, and  $\ell$  means the  $\ell^{\text{th}}$  degree of freedom. Along the Hamiltonian trajectory, where  $\frac{dq_{\ell}}{dt} = \frac{\partial H}{\partial p_{\ell}}$ ,  $\frac{dp_{\ell}}{dt} = -\frac{\partial H}{\partial q_{\ell}}$ ,  $\forall \ell$ , the time evolution of the distribution function is governed by the Poisson bracket with the Hamiltonian function. The rate of change of  $f$  is given by:

$$\frac{df}{dt} = \frac{\partial f}{\partial t} + \{f; H\} = 0, \quad (7)$$

which reflects the fundamental conservation law in classical mechanics and is known as the *Liouville theorem* (Liouville 1838). Consequently, the distribution function  $f$  remains conserved along the Hamiltonian trajectory.

Based on the integral relations for Poisson brackets, Sokolov et al. (2023) has developed a computationally efficient scheme for solving kinetic equations by the finite volume method. This newly developed Poisson bracket scheme is proved to conserve particles, possess the total-variation-diminishing (TVD, e.g., Sokolov et al. 2006a; Krivodonova & Smirnov 2021; Tóth 2023) property with second

order of accuracy in space, thus ensuring high-resolution numerical results. With the Poisson bracket scheme, Equation 4 can be reformulated into:

$$\frac{B}{\delta s} \left\{ f_{j,k}; \frac{\delta s p^3}{B} \right\}_{\tau, p^3/3} = \frac{B}{\delta s} \frac{\partial}{\partial s_L} \left( \frac{D_{xx}}{B \delta s} \frac{\partial f_{j,k}}{\partial s_L} \right), \quad (8)$$

where  $f_{j,k}$  is the distribution function along the field line that has been initially placed uniformly on the solar surface in longitude and latitude with the index  $j$  and  $k$ , respectively. Here,  $\delta s = ds/ds_L$ , where  $ds$  and  $ds_L$  are respectively the spatial size of the mesh along the field lines in Eulerian and Lagrangian coordinates. More details about the derivations of Equation 8 can be found in Section 4 of Sokolov et al. (2023).

By the Strang splitting method (Strang 1968; MacNamara & Strang 2016), at each time step, we first solve the advection equation in the phase space:

$$\left\{ f_{j,k}; \frac{\delta s p^3}{B} \right\}_{\tau, p^3/3} = 0, \quad (9)$$

where the Hamiltonian function is  $H \equiv \frac{\delta s p^3}{B}$ , with  $\tau$  and  $p^3/3$  being the two canonical coordinates as we solve the time-accurate transport equation for SEPs.

Note that the Poisson bracket scheme is general to various types of kinetic equations that can be formulated in terms of Poisson bracket scheme. Thereby, the pitch-angle-dependent distribution function, notated as  $\mathcal{F}(\mathbf{r}, \mathbf{p}, \mu, t)$ , can be solved with the focused transport equation, which incorporates the magnetic mirror force, betatron acceleration, and a non-inertial force proportional to  $\frac{d\mathbf{u}}{dt}$  (e.g., Northrop 1963; Roelof 1969; Skilling 1971; Isenberg 1997; Kóta 1997; Kóta & Jokipii 2004; van den Berg et al. 2020). It has been shown in Sokolov et al. (2019) that the focused transport equation can be formulated into multiple Poisson brackets with the potential to study the pitch angle dependence in testing cases, by the Poisson bracket scheme. In this work, we mainly target to solve the Parker transport equation (Equation 4) for the omni-directional distribution function, notated as  $f(\mathbf{r}, \mathbf{p}, t)$ , as a first trial after implementing the Poisson bracket scheme into M-FLAMPA. More realistic and sophisticated numerical models that take into account the pitch-angle dependence for the distribution function will be investigated in the future.

#### 2.3.4. Particle Diffusion

The interaction between the energetic protons and turbulent magnetic fields is modeled by the diffusion processes along the time-evolving magnetic field lines. Following Equation 9, within each time step, the transport equation will be subsequently solved for spatial diffusion along each field line in M-FLAMPA:

$$\frac{\partial f_{j,k}}{\partial \tau} = \frac{B}{\delta s} \frac{\partial}{\partial s_L} \left( \frac{D_{xx}}{B \delta s} \frac{\partial f_{j,k}}{\partial s_L} \right), \quad (10)$$

where the spatial diffusion coefficient along the magnetic field,  $D_{xx}$ , can be derived in the usual manner from the scattering integral with respect to the particle pitch angle,  $D_{\mu\mu}$  (e.g., Jokipii 1966;

Earl 1974; Lee 1982, 1983):

$$D_{xx} = \frac{v^2}{8} \int_{-1}^1 \frac{(1 - \mu^2)^2}{D_{\mu\mu}} d\mu, \quad (11)$$

$$D_{\mu\mu} = \frac{\pi\omega_{ci}^2}{2B^2/\mu_0} (1 - \mu^2) \frac{\omega_{ci}}{v|\mu|} I\left(\frac{\omega_{ci}}{v|\mu|}\right), \quad (12)$$

where  $v = |\mathbf{v}|$  denotes the energetic proton speed,  $\mu_0$  is the vacuum permeability,  $\omega_{ci} = \frac{qB}{m}$  is the cyclotron frequency of protons with  $e$  being the proton charge, and  $I(k)$  denotes the spectrum of turbulence with the wave number  $k \equiv \frac{\omega_{ci}}{v|\mu|}$ . We assume that the left and right polarized waves are balanced in the Alfvén wave turbulence, and each turbulence wave spectrum follows the Kolmogorov's spectrum with a power-law index of  $-5/3$  (Kolmogorov 1941; Zakharov et al. 2012). More details about the derivations can be found in Sokolov et al. (2009) and Borovikov et al. (2019). Finally, the parallel diffusion coefficient,  $D_{xx}$ , can be expressed in terms of the mean free path (MFP),  $\lambda_{xx}$ , and the proton speed,  $v$  (e.g., Sokolov et al. 2004):

$$D_{xx} = \frac{1}{3} \lambda_{xx} v, \quad (13)$$

with different treatments of  $\lambda_{xx}$  in the upstream and downstream of the shock in M-FLAMPA. In the upstream, the MFP has been derived and can be expressed as (Li et al. 2003; Li & Zank 2005; Zank et al. 2007):

$$\lambda_{xx} = \lambda_0 \cdot \frac{r}{1 \text{ AU}} \cdot \left(\frac{pc}{1 \text{ GeV}}\right)^{\frac{1}{3}}, \quad (14)$$

in which  $\lambda_{xx}$  is a free parameter suggested to be  $0.1 \sim 0.4$  AU. With the relativistic relations for energetic protons,  $D_{xx}$  can be expressed as:

$$D_{xx} = \frac{1}{3} \cdot \lambda_0 \cdot \frac{r}{1 \text{ AU}} \cdot \left[\frac{E_k (E_k + 2E_{p0})}{(1 \text{ GeV})^2}\right]^{\frac{1}{6}} \cdot \left[\frac{E_k (E_k + 2E_{p0})}{(E_k + E_{p0})^2}\right]^{\frac{1}{2}} \cdot c, \quad (15)$$

where  $c$  denotes the speed of light,  $E_k$  denotes the kinetic energy of energetic protons, and  $E_{p0} = m_p c^2 = 938.1$  MeV is the rest proton energy with  $m_p$  being the rest proton mass. It can be observed from Equation 15 that the upstream parallel diffusion coefficient approximately follows  $D_{xx} \propto r \cdot E_k^{2/3}$  for the keV-to-MeV energetic protons.

Note that different setups of the MFP and parallel diffusion coefficient may lead to different results (e.g., Kecskeméty et al. 2009; Zhao et al. 2016b, 2024). In order to justify the validity of the  $D_{xx}$  setup, we notice a recent study by Chen et al. (2024a), which examines the power spectrum density of the magnetic turbulence measured by the *Solar Wind Electrons, Alphas, and Protons* (SWEAP, Kasper et al. 2016) and *FIELDS* (Bale et al. 2016) instruments on board the *Parker Solar Probe* (*PSP*, Fox et al. 2016). Based on *PSP* observations in its Orbits 5–13, Chen et al. (2024a) derive an empirical formula of the parallel diffusion coefficient for 100 keV to 1 GeV energetic protons in the inner heliosphere:

$$D_{xx} = (5.16 \pm 1.22) \times 10^{14} \cdot \left(\frac{r}{1 \text{ AU}}\right)^{1.17 \pm 0.08} \cdot \left(\frac{E_k}{1 \text{ keV}}\right)^{0.71 \pm 0.02} [\text{m}^2 \text{ s}^{-1}]. \quad (16)$$

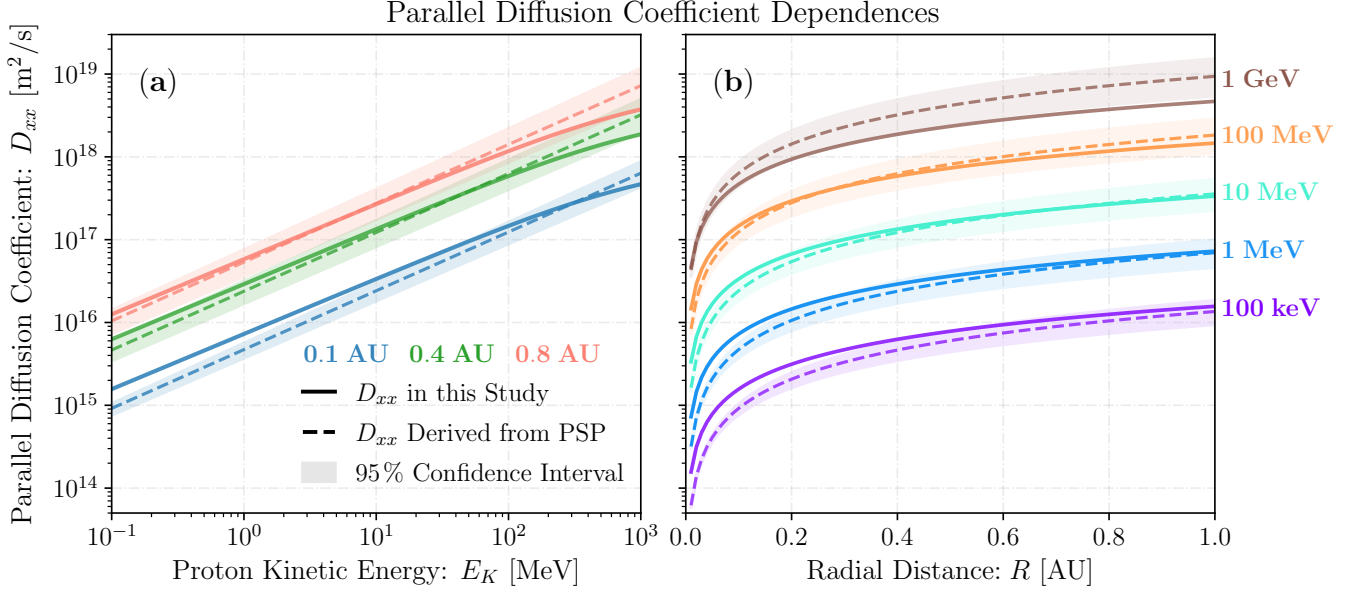


**Figure 2.** Parallel diffusion coefficient setup in our model. In each panel, the solid lines are the parallel diffusion coefficients applied to this study, and the dashed lines are the parallel diffusion coefficient derived from *PSP* observations, with the 95% confidence interval plotted as shaded areas (Chen et al. 2024a). (a): Parallel diffusion coefficient dependences on the proton kinetic energy, when the radial distance is fixed. Relations are shown when the radial distance is 0.1 AU, 0.4 AU, and 0.8 AU, plotted in blue, green, and red, respectively. (b): Parallel diffusion coefficient dependences on the radial distance, when the proton kinetic energy is fixed. Relations are shown when the proton kinetic energy is 100 keV, 1 MeV, 10 MeV, 100 MeV, and 1 GeV, plotted in purple, blue, cyan, orange, and brown, respectively.

With a similar index simplified from Equation 15 for the keV-to-MeV protons, i.e.,  $D_{xx} \propto r \cdot E_k^{2/3}$ , we compare the dependences of the diffusion coefficient adopted in M-FLAMPA on the heliocentric distance (see Figure 2(a)) and the proton energy (see Figure 2(b)) with those derived by Chen et al. (2024a) from the interplanetary turbulence level as observed by *PSP*. As depicted in Figure 2, this comparison demonstrates a perfect agreement within the 95% confidence interval, as long as the optimal value of  $\lambda_0 = 0.3$  AU is used.

In the downstream, the diffusion coefficient is calculated self-consistently through the total Alfvén wave intensity obtained from the MHD simulation. Following Equations 11–12, we introduce a minimum wave number,  $k_0$ , below which the turbulence level becomes negligible. In this way, the downstream MFP is derived by taking  $I(k)$  only for  $k \geq k_0$  in Equation 12, corresponding to sufficiently small spatial scales. With the derivations shown in Borovikov et al. (2019), we have:

$$\lambda_{xx} = \frac{81}{7\pi} \left( \frac{B}{\delta B} \right)^2 \frac{r_{L0}^{1/3}}{k_0^{2/3}} \cdot \left( \frac{pc}{1 \text{ GeV}} \right)^{1/3}, \quad (17)$$

in which  $\delta B$  is the turbulent field strength, and  $r_{L0} = \frac{1 \text{ GeV}}{ceB}$  is the Larmor radius for the particle momentum being 1 GeV/ $c$ . Herewith, we consider

$$k_0 = \frac{2\pi}{L_{\max}(r)}, \quad (18)$$

with the maximum spatial scale in the turbulence,  $L_{\max}(r) = 0.4r$  (e.g., Borovikov et al. 2019; Tenishev et al. 2022, and references therein), which gives a comparable magnitude of the MFP in

the shock downstream and upstream as shown later in Figure 14. Besides, in order to compensate for the eroded width of the shock wave front due to the finite mesh size in the MHD simulations ( $\sim 0.1 R_s$ ), the parallel diffusion coefficient for the low-energy particles is artificially enhanced to

$$D_{xx} = \max \{D_{xx}, D_{\min}\}, \quad (19)$$

where  $D_{\min} = 0.1 R_s \times 10^5 \text{ m s}^{-1}$ , as used in Sokolov et al. (2004); Borovikov et al. (2018).

By applying Equations 11–19, the diffusion equation in Equation 10 can be solved along each individual magnetic field line. It is important to note that this approach does not account for the perpendicular diffusion due to the field line random walk and particle decoupling from field lines, which remains a subject of active research and discussions within the community (e.g., Laitinen et al. 2013, 2016, 2018; Shalchi 2019, 2021; Chhiber et al. 2021) and will be visited carefully in our model in the future.

### 2.3.5. Particle Injection

Given the established particle dynamics near the shock wave front, the next essential component involves defining the initial injection conditions that work for the shock acceleration. In our study, the initial conditions for the omni-directional distribution function is assumed to be a suprathermal tail commonly observed in the solar wind (e.g., Gloeckler 2003; Fisk & Gloeckler 2006, 2008, and references therein), which extends from the thermal energy to the injection energy (or equivalent momentum) in our simulations (Sokolov et al. 2004):

$$f(p_{\text{inj}}) = \frac{c_i}{2\pi} \frac{n_p}{(2m_p k_B T_p)^{3/2}} \left( \frac{\sqrt{2m_p k_B T_p}}{p_{\text{inj}}} \right)^5, \quad (20)$$

where  $m_p$  is the rest proton mass,  $k_B$  is the Boltzmann constant,  $n_p$  and  $k_B T_p$  respectively denote the ambient plasma density and temperature in energy units calculated from stream-aligned AWSoM-R simulation. Here,  $p_{\text{inj}}$  is the injection momentum corresponding to the injection energy, which is set to be 10 keV at any location of the shock wave front (e.g., Ellison et al. 1990; Giacalone & Kóta 2007). Also, the amplitude of the injected particles is determined by the so-called injection coefficient,  $c_i$ , which indicates the fraction of suprathermal protons and can be derived from:

$$4\pi \int_{\sqrt{2mk_B T}}^{+\infty} p^2 f(p) dp = c_i n_p. \quad (21)$$

The injection coefficient is assumed to be 1 in our simulations. Nonetheless, there can still be discrepancy between the modeled proton fluxes with respect to the observations, so a scaling factor, set as 1.2 in this study, is incorporated to scale up or down the calculated proton flux to match with the observations for the event simulated (Zhao et al. 2024). Since the self-generated waves by the streaming protons are not included in the simulation, the acceleration and transport of energetic protons remain unaffected by such a scaling factor.

In order to better compare with the observations, the calculated proton flux is scaled up or down by a scaling factor to match with the observations for the event simulated. Because the self-generated waves by the streaming proton are not calculated in the simulation, the acceleration and transport of protons are not affected by such scaling. The scaling factors can be understood as the difference of the calculated proton flux with respect to the observations.

**Table 1.** Key Input Parameters of the Stream-Aligned AWSoM-R, EEGGL, and M-FLAMPA Models in SWMF for this Study

Model	Parameter	Value
Stream-Aligned AWSoM-R	Poynting flux parameter ( $S_A/B$ )	$0.3 \text{ MW m}^{-2} \text{ T}^{-1}$
	Correlation length for dissipation ( $L_{\perp}\sqrt{B}$ )	$1.5 \times 10^5 \text{ m T}^{1/2}$
	Stochastic heating exponent ( $h_S$ )	0.24
	Stochastic heating amplitude ( $A_S$ )	0.18
EEGGL	CME speed	861 km/s
	Type of the flux rope	GL
	Selected AR positive pole location*	( $66^\circ, 16^\circ$ )
	Selected AR negative pole location*	( $75^\circ, 14^\circ$ )
M-FLAMPA	Diffusion coefficient free parameter ( $\lambda_0$ )	0.3 AU
	Injection momentum spectral index	-5
	Injection scaling factor	1.2

\* These locations are given as the Carrington longitude and latitude.

In short, Table 1 summarizes the key input parameters used for this study, as we stated through Section 2.

### 3. THE 2013 APRIL 11 SEP EVENT: OVERVIEW

The SEP event on 2013 April 11 was one of the large SEP events in solar cycle 24 observed at high energies (e.g.,  $> 25$  MeV protons) across a broad range of heliospheric locations (Richardson et al. 2014; Gopalswamy et al. 2015; Paassilta et al. 2018). Lario et al. (2014) has reported the SEP measurements by multiple spacecrafts, including the *Solar TERrestrial RELations Observatory Ahead/Behind* (*STEREO-A/B*, Kaiser et al. 2008, short for STA and STB in this paper, respectively), the *SOLar and Heliospheric Observatory* (*SOHO*, Domingo et al. 1995), the *Advanced Composition Explorer* (*ACE*, Stone et al. 1998), the *WIND* spacecraft. They also analyzed the corresponding solar sources of this event by examining the extreme ultraviolet (EUV) wave observations and white-light (WL) coronagraph images from STA, STB, the *Geostationary Operational Environmental Satellite* (*GOES*, Menzel & Purdom 1994), *WIND*, and the Atmospheric Imaging Assembly (AIA, Lemen et al. 2012) on board the *Solar Dynamics Observatory* (*SDO*, Pesnell et al. 2012). Furthermore, this particular event has also showed high ratios of Fe/O abundances at both STB and Earth (see Figure 4 in Lario et al. (2014) and more details in Cohen et al. (2014)), challenging the remnant flare material theory of Tylka et al. (2005).

In this event, the filament eruption that triggered the CME responsible for this SEP event has been investigated by multiple observations (e.g., Vemareddy & Mishra 2015; Joshi et al. 2016; Kwon & Vourlidas 2017; Palmerio et al. 2018; Fulara et al. 2019; Pan et al. 2022). On 2013 April 11, an M6.5 X-ray flare was erupted from the NOAA AR 11719, located at heliographic latitude  $+9^\circ$  and longitude  $-12^\circ$  (N09E12) as viewed from Earth. The soft X-ray emission began at 06:55 UT and peaked at 07:16 UT. Both STB and *WIND* observed the type III radio bursts from the highest

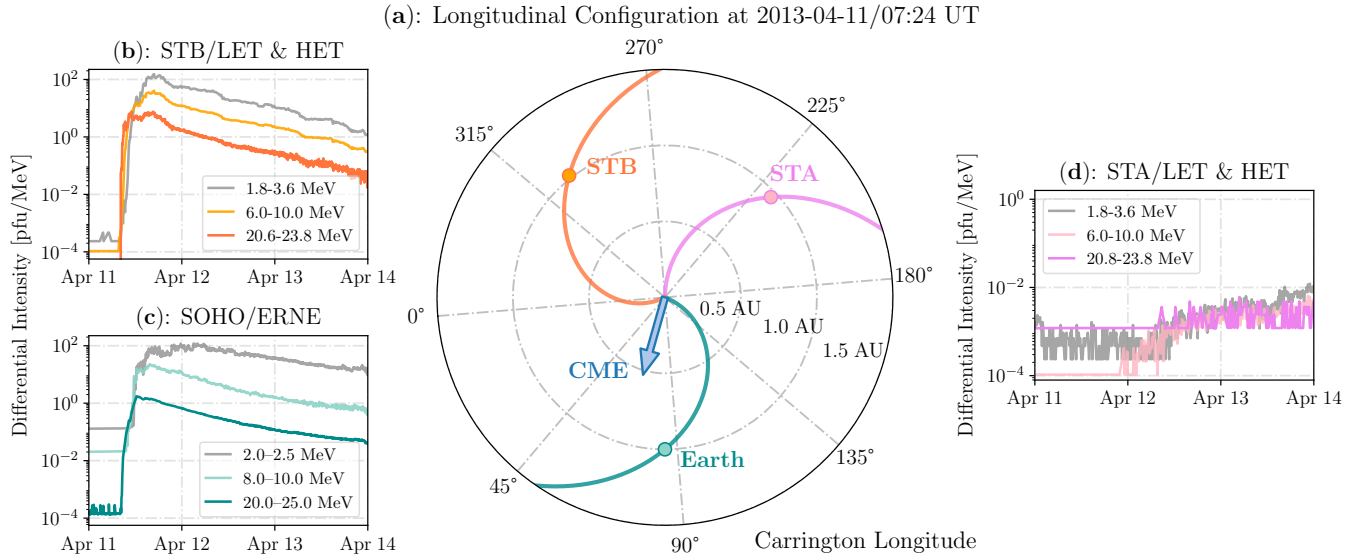


**Figure 3.** Overview of the 2013 April 11 SEP Event. (a): Longitudinal configuration of the Earth, STA, and STB at the CME eruption, plotted in green, pink, and orange, respectively, together with the nominal IMF lines taken from the Solar-Mach tool (Gieseler et al. 2023). Heliographic rotating (HGR) coordinates are applied here. Each scattered point is the location of the observer, with the field line connecting to the solar surface. The blue arrow represents the CME eruption orientation for this event. (b)(c)(d): Measurements of energetic particles in STB/LET and HET, SOHO/ERNE at Earth, and STA/LET and HET, respectively.

frequencies that the instruments can detect ( $\sim 16$  MHz) starting at about 06:58 UT, whereas STA observed the type III burst only at frequencies below 1 MHz starting around 07:00 UT.

An accompanied CME was then observed by the C2 coronagraph of the *Large Angle and Spectrometric Coronagraph* (LASCO, Brueckner et al. 1995) on *SOHO* at 07:24 UT, and the COR1 coronagraph (Thompson et al. 2003) of the *Sun Earth Connection Coronal and Heliospheric Investigation* (SECCHI, Howard et al. 2008) telescope on both STA and STB at 07:54 UT (Cohen et al. 2014). The observations indicate that this is a moderately fast halo CME, with the CME speed of 861 km/s as reported in the SOHO/LASCO CME catalog<sup>4</sup> (Yashiro et al. 2004; Gopalswamy et al. 2009). A type II radio burst was observed by both STB and *WIND* starting at 07:10 UT and ending at around 15:00 UT in the range of frequencies from 10 MHz to 200 kHz, as reported by Lario et al. (2014); Park et al. (2015).

Figure 3(a) illustrates the longitudinal distribution of the spacecraft shortly before the CME eruption on 2013 April 11, as viewed from the north ecliptic pole. The green, pink, and orange scatter points represent the locations of the Earth, *STEREO-A* (STA), and *STEREO-B* (STB), respectively. Detailed coordinates about the spacecraft locations in space is provided in Table 2. This angular separation of the spacecraft enables an analysis of whether the SEP event spanned a wide range of heliolongitudes, even offering insights into the underlying physics.

In Figure 3(a), nominal IMF lines connecting each spacecraft with the Sun (located at the center) are also plotted in the same color as the spacecraft. These spirals assume a Parker spiral field with a constant solar wind speed (Parker 1958) and an analytical solution taken from the Solar-Mach tool<sup>6</sup> (Gieseler et al. 2023). Here, we estimate the solar wind speed ( $U_{sw}$ ) by averaging the *in-situ*

<sup>6</sup> <https://solar-mach.github.io/>

**Table 2.** Table of the Spacecraft, Solar Wind, and IMF Properties.

S/C	$\phi_C$ [Deg]	$\theta_C$ [Deg]	$r$ [AU]	$U_{sw}$ [km/s]	$\phi_F$ [Deg]	$l_F$ [AU]	$\Delta\phi_{F,AR}$ [Deg]
Earth	85.3	-5.9	1.00	363	154.0	1.08	84.5
STA	218.7	7.2	0.96	514	264.7	1.04	164.8
STB	303.5	2.3	1.02	327	21.8	1.22	47.8

NOTE—This table lists the spacecraft (S/C) used in this study, along with key parameters: the Carrington longitude ( $\phi_C$ ), Carrington latitude ( $\theta_C$ ), and heliocentric distance ( $r$ ) of each spacecraft; the *in-situ* solar wind plasma speed ( $U_{sw}$ ); the Carrington longitude of the nominal magnetic footpoint ( $\phi_F$ ), the IMF line length connecting the spacecraft to the Sun ( $l_F$ ); and the Carrington longitude difference between the magnetic footpoint of the spacecraft and the source region of this SEP event ( $\Delta\phi_{F,AR}$ ).

plasma measurements from the NASA Goddard Space Flight Center (GSFC) OMNI dataset<sup>7</sup> (King & Papitashvili 2005) over a 12-hour window prior to the eruption. The resulting quiet solar wind speed is approximately 363 km/s at Earth,  $\gtrsim$  500 km/s at STA, and 327 km/s at STB, giving the magnetic footpoint separations of 110°–130° between pairs of spacecraft, as listed in Table 2. Other more methods calculating magnetic footpoint separations are discussed in Section 2 of Lario et al. (2014). Table 2 also includes the magnetic field line length connecting each spacecraft to the Sun.

In Figure 3(a), the orientation of the CME flux rope derived from EEGGL and inserted at 07:24 UT, is marked as a blue arrow. The flux rope is positioned above AR 11719, centered at (69.5°, 14.5°) in Carrington longitude and latitude, as depicted in Figure 1(b). The longitude differences between the magnetic footpoint of each spacecraft and the AR ( $\Delta\phi_{F,AR}$ ) are then calculated and presented in Table 2, suggesting that the magnetic footpoint of STB is the closest to AR 11719 among the three observers, with a separation of 47.8°, followed by the Earth with  $\Delta\phi_{F,AR}$  being 84.5°, and STA, which was the furthest, with  $\Delta\phi_{F,AR}$  being 164.8°.

Figure 3(b)–(d) shows the energetic particle intensity-time profiles measured by (b) the *Low Energy Telescope* (LET, Mewaldt et al. 2008) and *High Energy Telescope* (HET, Von Rosenvinge et al. 2008) on STB, (c) the *Energetic and Relativistic Nuclei and Electron* instrument (ERNE, Torsti et al. 1995; Valtonen et al. 1997) on SOHO, and (d) LET and HET on STA. We choose 3 energy channels for each spacecraft as shown in Figure 3(b)–(d), as representative of particle measurements at relatively lower, intermediate, and relatively higher energies, respectively. It can be found from Figure 3(b)–(c) that the onset phase of the SEP event appears sharper at STB compared to Earth, especially in the relatively higher energy channel (20.6–23.8 MeV in STB/HET, and 20.0–25.0 MeV in SOHO/ERNE). A more detailed comparison of the onset phase of Earth and STB can be found in Figure 5 of (Lario et al. 2014), where particle measurements from the *3D Plasma and Energetic Particle* instrument (3DP, Lin et al. 1995) on board the spin-stabilized WIND spacecraft, the *Electron, Proton, and Alpha Monitor* (EPAM, Gold et al. 1998) on board ACE, and the *Solar Electron and Proton Telescope* (SEPT, Müller-Mellin et al. 2008) on both STA and STB are shown and analyzed. Besides, Figure 3(b)–(c) shows that the SEP fluxes at STB decay more quickly than at Earth, especially in the relatively lower energy channel (1.8–3.6 MeV in STB/HET, and 2.0–2.5 MeV in SOHO/ERNE).

<sup>7</sup> <https://omniweb.gsfc.nasa.gov/>



While noticeable SEP fluxes are observed at both Earth and STB, there is only a slight enhancement of particle measurements at the relatively lower (1.8–3.6 MeV) and medium (6.0–10.0 MeV) energy channels at STA, as shown in Figure 3(d). As we find these differences of SEPs across a broad range of heliospheric locations in Figure 3, we are going to use our self-consistent models in SWMF to simulate this event, and explain these different behaviors with the new synthetic observables provided by the numerical modeling study.

#### 4. NUMERICAL MODELING RESULTS

In this section, we sequentially present multiple types of observables from numerical modelings. In Section 4.1, we show the results of steady-state solar wind simulations for the Carrington rotation with 2013-04-11/06:04 UT placed in the center. With the steady-state solar wind solution, the flux rope is inserted on top of the AR where the CME is erupted. We show the CME initialization and evolution, and compare the modeled results with the WL images from observations in Section 4.2. In Section 4.3, we introduce our newly developed shock capturing tool and illustrate how the shock surface is identified and evolved in the low corona. Last but not least, in Section 4.4, we highlight our SEP simulation results by M-FLAMPA and compare them with *in-situ* particle measurements.

##### 4.1. Steady-State Solar Wind

Taking the processed-GONG magnetogram shown in Figure 1(a) and the parameters listed in Table 1 as inputs, the stream-aligned AWSoM-R model can provide different types of solar wind plasma parameters, where the solar wind speed at the equatorial plane in IH is shown in Figure 4(a). In our simulation, the computational domain covers from  $-500 R_s$  to  $500 R_s$  for the 3D Cartesian coordinates, with the sun placed in the center. In Figure 4(a), we also include the locations of the Earth, STA, STB, as well as the field lines connecting them and the lower boundary of IH, respectively. We can tell the simulated global distribution of the solar wind speed from Figure 4(a): The Earth and STA locate at regions with relatively fast solar wind ( $> 500$  km/s), while the solar wind is relatively slow at STB ( $\simeq 300$  km/s). In Figure 4(a), there also exists a few regions with slow or fast solar wind, and their interfaces in our simulations.

Among the simulated steady-state solar wind parameters, the electron density and temperature are used to synthesize the EUV line-of-sight (LOS) images, which are compared with the multi-wavelength EUV observations<sup>8</sup> from *SDO/AIA* and the *Extreme Ultraviolet Imager* (EUVI, [Wuelser et al. 2004](#)) on board STA and STB. The model-data comparisons are shown in Figure 4(b)–(d), corresponding to 193 Å and 211 Å bands for *SDO/AIA*, and 171 Å and 195 Å for STA/EUVI and STB/EUVI, respectively. For each comparison, the top row shows the model-synthesized LOS EUV images while the bottom row shows the observation results. Key findings from the EUV image comparisons in Figure 4(b)–(d) are:

1. The simulation results exhibit reasonable consistency with the observations in matching the relative brightness on a global scale, capturing the positions of major coronal holes (CHs) and ARs. This consistency indicates that the stream-aligned AWSoM-R model is able to reproduce the 3D structure of the density and temperature in the low solar corona.

<sup>8</sup> <https://sdac.virtualsolar.org/cgi/search>

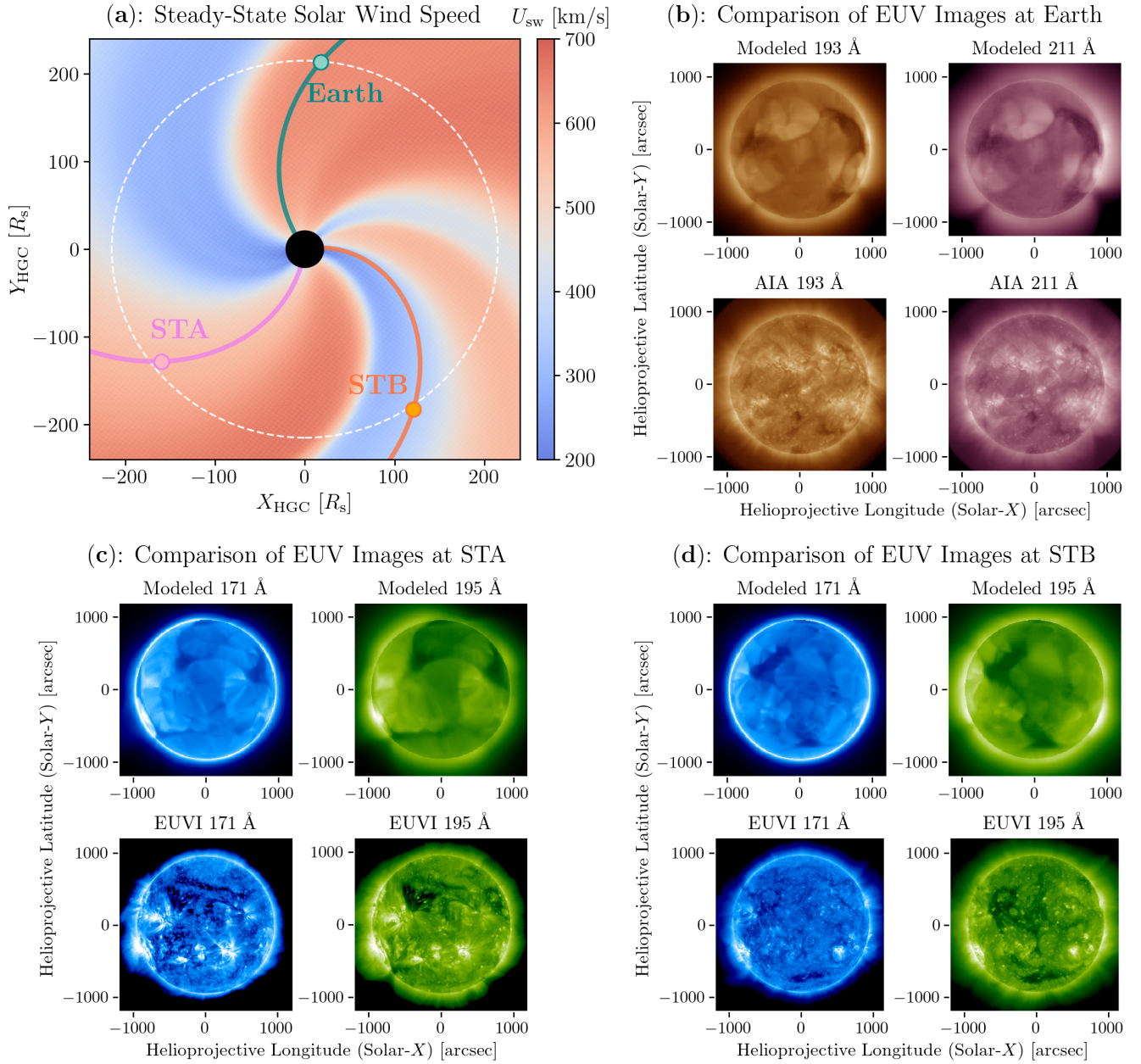


**Figure 4.** Steady-state simulation results by ASoM-R solving the stream-aligned MHD equations. (a): Background solar wind speed in the equatorial plane, with the field line connecting to the Earth (green), STA (pink), and STB (orange), respectively. Carrington Heliographic (HGC) coordinates are used. The black solid circle at the center is the lower boundary of IH in our simulations ( $24 R_s$ ). The white dashed circle represents the 1 AU sphere. (b)(c)(d): Comparison of the EUV images at Earth, STA, and STB, respectively. The modeled images at  $193 \text{ \AA}$  and  $211 \text{ \AA}$  wavelengths are compared with *SDO/AIA* at Earth, and images at  $171 \text{ \AA}$  and  $195 \text{ \AA}$  wavelengths are compared with *EUVI* at STA and STB, respectively. Helioprojective longitude and latitude are shown in the modeled and observed images for spatial references.

2. Notably, the CHs in the north hemisphere are get well captured from the STA and STB view, and the narrow CH close to the south pole is also reproduced from the STB view, as shown in Figure 4(c)(d). While the CHs in the north hemisphere is visible from the view of the Earth,

it does not fully align with *SDO/AIA* observations in Figure 4(b). As discussed in Sachdeva et al. (2023), the actual solar CHs contain small-scale, closed field line loops and magnetic flux that add to their brightness. In contrast, the numerical simulation often lack these small-scale features, leading to darker CHs in the synthetic images.

3. As illustrated in Figure 4(b)–(d), respectively, the stream-aligned AWSoM-R model can effectively reproduce the bright ARs on the west limb from the Earth view, and the ARs on both the west and east limbs from the STA and STB views. However, the small-scale ARs in the center of the EUV images observed are partially or even not present in the model results. It is worth noting that April 2013 is near the solar maximum in solar cycle 24. Our steady-state simulation is performed with a synoptic magnetic field map over a Carrington rotation (see Section 2.1) whereas the observations are updated for particular timestamps. Therefore, it is reasonable that the model cannot reproduce all the dynamic and time-dependent solar activities during the rotation (e.g., Sachdeva et al. 2019).

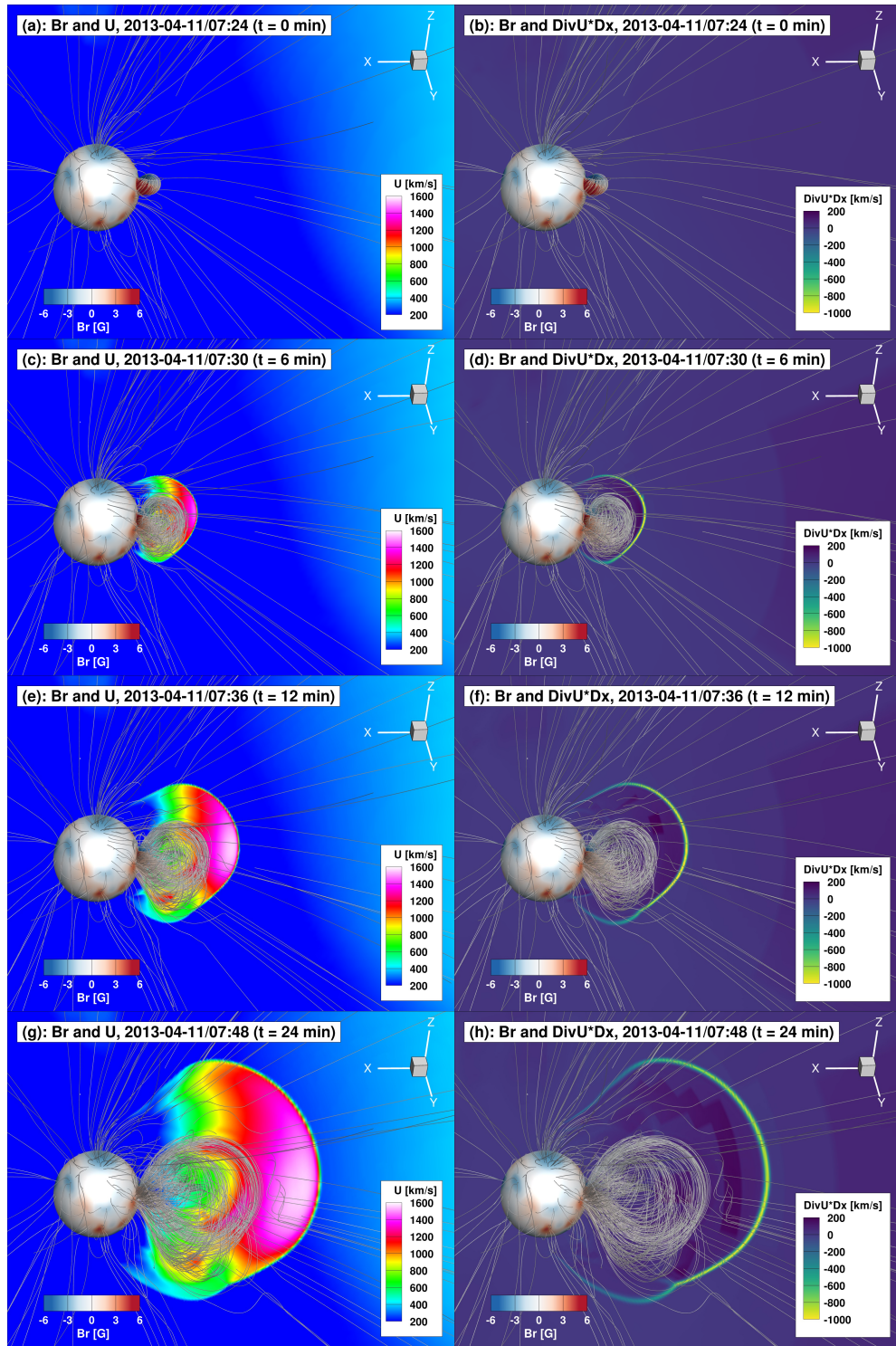
Despite the discrepancies in some fine structures, such as CHs and ARs, the model overall demonstrates good agreements in terms of the brightness and spatial location and scale of these features, indicating high simulation performance in capturing the global structure in the low corona (Downs et al. 2010; Sachdeva et al. 2019, 2021). The comparisons shown in Figure 4(b)–(d) validate the synthesized EUV observables and suggest the readiness of steady-state solar wind solutions for subsequent simulations.

#### 4.2. CME Initialization and Propagation

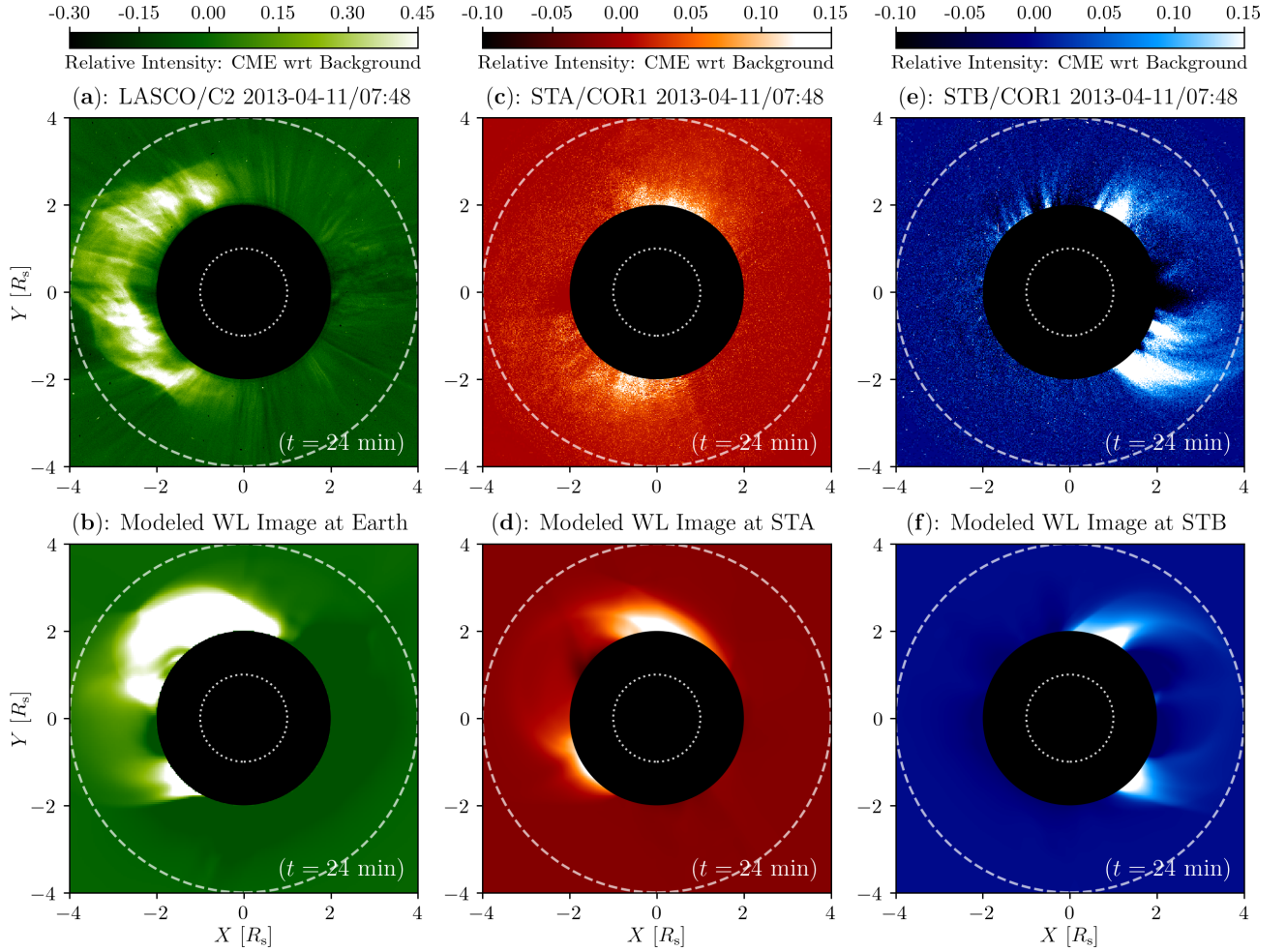
After getting the steady-state solar wind solutions, an imbalanced GL magnetic flux rope (Gibson & Low 1998) and its entrained plasma are placed on top of the parent AR (AR 11719 for this event). Figure 1(b) shows the location of the AR field, and Figure 1(c) shows the 3D topology and the radial magnetic field strength of the inserted flux rope. Figure 1(c) also depicts the field lines extended outward for the distorted flux rope, caused by the magnetic reconnection and interaction with the bi-modal solar wind. The parameters of the flux rope, including the total magnetic field, the flux rope size, and the flux rope orientation, are calculated based on the GONG magnetogram shown in Figure 1(a), and the observed CME speed, which is 861 km/s as stated in Section 3. More details can be found in, e.g., Manchester IV et al. (2004c, 2005); Jin et al. (2016).

Figure 5 presents the time evolution of the CME from a 3D view, with a time series of panels showing the system at  $t = 0, 6, 12,$  and  $24$  minutes. In each panel, the magnetic field lines are represented by the solid lines, and the blue-to-red colors demonstrate the radial magnetic field strength on the surface of  $1.15 R_s$  and the field lines. Open field lines can be easily found near the poles, and the streamer-shaped field lines are also visible in the south. A plane cut depicts the distribution of the plasma speed in the left column (Figure 5(a)(c)(e)(g)), and the divergence of velocity field times the cell size (called  $\text{DivU} \cdot \text{Dx}$  hereafter) in the right column (Figure 5(b)(d)(f)(h)), corresponding to the colorbar at the right corner of each panel. The steady-state background solar wind solutions give  $\sim 200$  km/s solar wind speed and  $\sim 0$  km/s  $\text{DivU} \cdot \text{Dx}$  in the low corona. At  $t = 0$ , as we place the flux rope on top of AR 11719, we do not change the velocity of the initial state to drive self-similar evolution (see Figure 5(a)). Instead, we let the system evolve from an initial state of force imbalance.

The evolution of the flux rope starts with rapid acceleration to a fast speed over 1200 km/s in the low corona. The fast propagation of the CME drives a fast mode MHD shock ahead of the flux rope,



**Figure 5.** Evolution of the flux rope, the velocity field, and the divergence of velocity field in SC. HGR coordinates are used with the negative  $X$  axis pointing to the Earth in these panels. (a): Initial flux rope at the solar surface plotted with  $B_r$  strength, with the velocity field in SC. (b): Initial flux rope at the solar surface plotted with  $B_r$  strength with the divergence of velocity field times the cell size in SC. (c)(d): Similar to (a)(b) but at 6 minutes after the CME eruption. (e)(f): Similar to (a)(b) but at 12 minutes after the CME eruption. (g)(h): Similar to (a)(b) but at 24 minutes after the CME eruption.



**Figure 6.** Comparison of the LASCO/C2 (left column), STA/COR1 (middle column), and STB/COR1 (right column) WL images at 24 minutes after the CME eruption. Upper panels are observations, and lower panels are the corresponding model-synthesized WL images. The color scale shows the relative intensity changes of WL total brightness with respect to the background solar wind. In each image, the radius of the inner white dotted circle, the black solid circle, and the outer dashed white circle are at  $1 R_s$ ,  $2 R_s$ , and  $4 R_s$ , respectively.

corresponding to the interface between the magenta and blue parts located ahead of the flux rope in Figure 5(c)(e)(g). For the fast mode MHD shock, since the plasma speed drops dramatically from  $> 1200$  km/s to  $\sim 200$  km/s in the outward direction from the Sun, the divergence of the velocity speed tends to be very small. We then calculate the time-evolving  $\text{DivU} \cdot \text{Dx}$  distribution, which is around  $-1000$  km/s at the shock wave front as displayed in Figure 5(d)(f)(h). As the flux rope propagates outward, it can continuously interact with the background magnetic field, undergoing magnetic reconnection and changing the field topology. The interaction is evident in the bent field lines in the downstream of the shock but ahead of the flux rope, as shown in Figure 5(e)–(h).

Moreover, as the CME travels outward from the Sun, its propagation direction can be affected by the interaction between the flux rope and the background solar wind or solar corona structures (see Manchester et al. 2017; Shen et al. 2022, and references therein). Since the CME propagation in SC is mainly observed by the WL coronagraphs, we compare the model-synthesized WL images

with the observations<sup>8</sup>, in order to validate the propagation direction of the CME. In our model, the synthetic WL images are created by integrating the Thomson-scattered light along the LOS that comprises the image. As illustrated in Figure 6, we compare the model-synthesized WL images with the LASCO/C2 (Figure 6(a)(b)), STA/COR1 (Figure 6(c)(d)), and STB/COR1 (Figure 6(e)(f)) coronagraphs observed. C2 has a field of view (FOV) from  $2 R_s$  to  $6 R_s$ , and COR1 has a FOV from  $1.7 R_s$  to  $4 R_s$ . Here we limit the FOV within  $4 R_s$ . In each panel of Figure 6, the inner white dotted circle, the black solid circle, and the outer dashed white circle show the radius at  $1 R_s$ ,  $2 R_s$ , and  $4 R_s$ , respectively, as a reference. The color scale shows the relative intensity changes of WL total brightness after the launch of the CME flux rope with respect to the background, where the total brightness is the sum of the plane-of-sky and LOS polarization along with dust-scattered light (e.g., Hayes et al. 2001; Morgan et al. 2006). Here we list our key findings by comparing the WL images in multiple views, and propose the possible explanations for some of them:

- 1 In the view of LASCO/C2, the core structure of the CME propagates eastward as shown in Figure 6(a)(b). The envelope of the observed CME appears to be symmetric with respect to the solar equator. However, the northern part of the CME is brighter than the southern part in the model-synthesized WL image, demonstrating an asymmetric shape. We examine the plasma properties in our simulations and find a high-density region lying in front of the flux rope, which can slow down the CME propagation, thus contributing to this asymmetry (Zhao et al. 2024).
- 2 In the view of STA/COR1, we primarily see the root of the CME connecting to the low solar corona in Figure 6(c). Those noisy white dots in the east part of the images may indicate the CME propagation direction; nonetheless, the brightness change is not very pronounced because of the location separation as shown in Figure 3(a). In our simulations, we basically reproduce these structures including the CME roots and some weakly intensified brightness in the west, as illustrated in Figure 6(d). Since STA is located nearly on the far side of AR 11719 with a magnetic footpoint separation of  $\sim 165^\circ$  from AR 11719 (see Table 2), it is reasonable to see only a part of the CME structure.
- 3 In the STB/COR1 view, the CME propagates westward with a nearly symmetric structure with respect to the solar equator. Comparing Figures 6(e)(f), our model-synthesized WL images align with the observations except for some slight differences for the brightness in the south, which is likely linked to the high-density region ahead of the flux rope that also affects the symmetry in the LASCO/C2 view.

Furthermore, we note that these image comparisons are influenced by significant projection effects, which can complicate the interpretation of CME structure and brightness distribution. In the future, the development of improved solar corona observation techniques is hoped to provide more accurate and detailed reconstructions of CME properties (Palmerio et al. 2023; Lugaz et al. 2024).

#### 4.3. Shock Wave Front

Note that in Figure 5, a CME-driven shock propagates ahead of the flux rope. Because of the role played by the CME-driven shocks in the SEP acceleration process, simulations of CME-driven shocks and the properties are essential to numerical modelings of SEPs (e.g., Mikić & Lee 2006; Lee et al. 2012; Manchester et al. 2017). Studies in the past have tried to reconstruct the shock surface,

derive the shock properties, and find the magnetic connectivity to investigate the energetic particles (e.g., Smith & Dryer 1990; Lario et al. 1998; Shen et al. 2011; Kwon et al. 2014; Bain et al. 2016; Rouillard et al. 2016; Plotnikov et al. 2017; Kouloumvakos et al. 2019). A feasible way to obtain more information about the CME-driven shocks is to capture the shocks from MHD simulations. Recently, satisfying agreements of shocks in simulations and observations have been found among several state-of-the-art models (e.g., Török et al. 2018; Downs et al. 2021; Ding et al. 2022; Jin et al. 2022, 2024), which indicates the capability of constructing realistic CME-driven shocks from current numerical modelings. In our model, we have developed a shock capturing tool embedded in the MHD simulations for a better understanding of the time-evolving shock surface properties.

In the stream-aligned AWSoM-R model, a second-order shock-capturing scheme with limiters has been implemented (van der Holst et al. 2014; Sokolov et al. 2013, 2022). Furthermore, different levels of the adaptive mesh refinement (AMR, see Berger & Colella 1989; Gombosi et al. 2003, 2004; van der Holst et al. 2011; Tóth et al. 2012, and references therein) have been applied to refine the mesh and improve the spatial accuracy near the shock. In our simulation, we use the pressure jump ratio ( $p_{\text{down}}/p_{\text{up}}$ ) as our criterion, calculated by the pressure in the downstream to the upstream<sup>9</sup>. When  $p_{\text{down}}/p_{\text{up}} \leq 1.3$ , the mesh gets coarsened; when  $p_{\text{down}}/p_{\text{up}} \geq 2.0$ , the mesh gets refined; otherwise, the mesh remains unchanged. For mesh refinement, the maximal resolution is set to 0.75 degrees in the SC region, and 0.75  $R_s$  in the IH region.

As we get the setup for the mesh, it is necessary to well recognize the shock structure in the MHD simulations. In the shock wave front, the divergence of the velocity field turns to be very small and negative, as we can tell from Figure 5, which corresponds to a significant adiabatic heating for particles (see Equation 4 and texts to it). With AMR near the shock wave front, DivU\*Dx is selected as the criterion because it incorporates the divergence of velocity field and the mesh size. In our shock capturing tool, from the center of the Sun, the shock surface is extracted along radial lines starting from a longitude-latitude grid. Along each radial line, the shock wave front is identified by the smallest value of DivU\*Dx. Considering the fluctuations for the modeling tool and realistic structures in the system, a threshold of DivU\*Dx needs specified by the users. In our simulation, the DivU\*Dx threshold is  $-120$  km/s, referring to the DivU\*Dx distribution shown in Figure 5. In this way, if the minimum DivU\*Dx is still greater than the threshold, there is no shock surface recognized. Conversely, when the minimum DivU\*Dx is smaller than the threshold, the radial distance of the surface and the shock associated parameters are saved.

Once we capture the shock surface, the *Rankine–Hugoniot jump conditions* (Rankine 1870; Hugoniot 1889a,b) are solved for the discontinuity in the model, providing the jump conditions for various parameters, such as the density, velocity, pressure and the shock normal. Specifically, the unit vector of the shock normal,  $\mathbf{n}$ , is calculated by using the magnetic coplanarity condition (Lepping & Argentiero 1971; Abraham-Shrauner 1972):

$$(\mathbf{B}_{\text{down}} - \mathbf{B}_{\text{up}}) \cdot \mathbf{n} = 0, \quad (22a)$$

$$\mathbf{n} = \frac{(\mathbf{B}_{\text{down}} \times \mathbf{B}_{\text{up}}) \times (\mathbf{B}_{\text{down}} - \mathbf{B}_{\text{up}})}{|(\mathbf{B}_{\text{down}} \times \mathbf{B}_{\text{up}}) \times (\mathbf{B}_{\text{down}} - \mathbf{B}_{\text{up}})|}, \quad (22b)$$

<sup>9</sup> In this paper,  $\langle \dots \rangle_{\text{down}}$  and  $\langle \dots \rangle_{\text{up}}$  refer to the parameter in the shock downstream and upstream, respectively.

and the shock obliquity angle,  $\theta_{Bn}$ , is obtained by measuring the angle between the upstream magnetic field and the shock normal. The shock speed ( $U_{\text{shock}}$ ) and Alfvén Mach number ( $M_{\text{Alfvén}}$ ) are calculated by:

$$U_{\text{shock}} = \frac{\rho_{\text{down}} U_{n,\text{down}} - \rho_{\text{up}} U_{n,\text{up}}}{\rho_{\text{down}} - \rho_{\text{up}}}, \quad (23)$$

$$M_{\text{Alfvén}} = \frac{U_{\text{shock}}}{V_A}. \quad (24)$$

with  $U_{n,\text{down}} = \mathbf{U}_{\text{down}} \cdot \mathbf{n}$  and  $U_{n,\text{up}} = \mathbf{U}_{\text{up}} \cdot \mathbf{n}$  being the downstream and upstream flow speed normal to the shock, respectively. In Equation 23, if using corotating frames, the solar wind rotation velocity will be removed in order to get the shock speed in an inertial frame. In Equation 24,  $V_A$  is the Alfvén speed calculated by  $B/\sqrt{\mu_0\rho}$  with  $\mu_0$  being the vacuum permeability.

Figure 7 presents the shock surface at  $t = 24$  minutes after the CME eruption from the front (left column) and back (right column) views. Here, the front view refers to the view directly facing AR 11719, and the back view is with a 180-degree change in longitude. We show the shock wave front superimposed by the compression ratio, shock normal angle, and Alfvén Mach number, in Figure 7(a)(b), (c)(d), and (e)(f), respectively. We can see three large-scale cone-shape pieces constructing the 3D shock surface, and at each of their interfaces, there are dramatic changes in the parameters. For example, the compression ratio gets much stronger at the interfaces of these pieces as the shock propagates (see, e.g., [Barkhudarov et al. 1991](#), for more details). While there is one single CME launched, these multiple pieces found are probably due to the interaction between the CME and the inhomogeneity of the background, as we can also tell from Figure 5.

After we capture the 3D shock surface from our numerical simulations, in order to understand the shock properties associated with the observers in the IP space, it is essential to determine its magnetic connectivity to the shock. In our study, we save all the plasma parameters together with the mesh structure in 3D space from our stream-aligned MHD simulations, and we treat field line tracing as a post-processing step. We start from the observers (e.g., Earth) and trace the field lines backward to the lower boundary of the SC region by iterations:

$$\mathbf{r}^{(j+1)} = \mathbf{r}^{(j)} + \mathbf{b}(\mathbf{r}^{(j)}) ds, \quad (25)$$

in which  $j$  is the iteration number, and  $ds$  denotes a small length step chosen to be 0.1 of the mesh size in this work. In Figure 7, we show the field lines in the low solar corona at  $t = 24$  minutes after the CME eruption, which connect to the Earth, STA, and STB, plotted in green, pink, and orange, respectively. At  $t = 24$  minutes, there is no magnetic connection between the shock surface and STA, while a connection exists for the Earth and STB. As illustrated in Figure 7, the Earth is connected to a weaker shock region where the shock compression ratio is as low as  $\sim 1.5$ , the shock is quasi-parallel with  $\theta_{Bn}$  being about  $30^\circ$ , and the Alfvén Mach number is  $\sim 1.0$ , while STB is connected to a stronger shock region where the shock compression ratio is  $\sim 2.0$ , the  $\theta_{Bn}$  is about  $45^\circ$ , and the Alfvén Mach number is  $\sim 5.0$ .

Furthermore, with a 1-minute cadence, we trace the field lines and examine the shock properties at the intersection between the magnetic field lines and the shock wave front. Figure 8 illustrates the time evolution of the shock properties associated with the field lines connecting to the Earth, STA, and STB, plotted in green, pink, and orange, respectively. These properties include the criterion



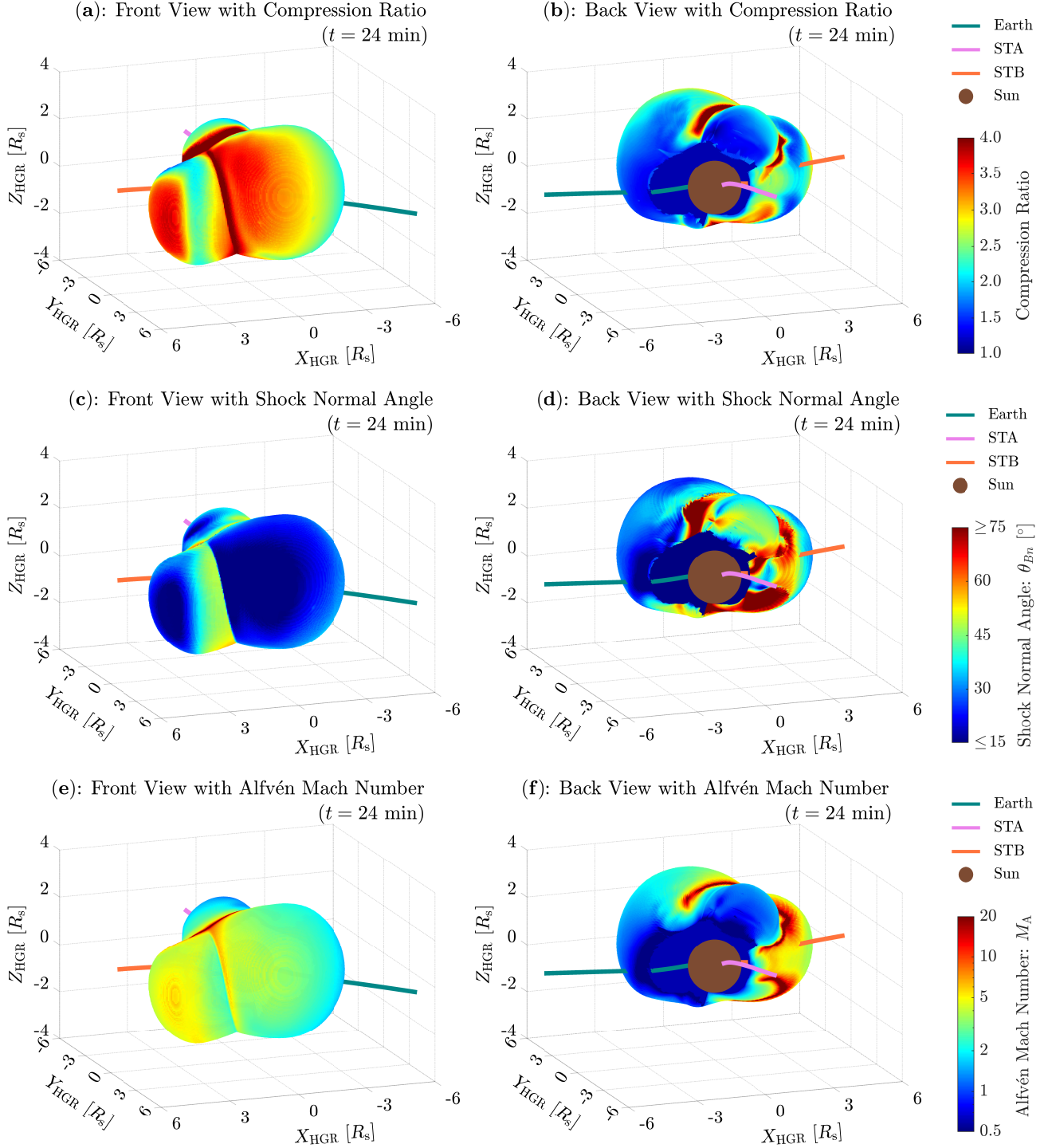


**Figure 7.** Shock surface at 24 minutes after the CME eruption. HGR coordinates are applied to all the panels. In each panel, field lines connecting to Earth, STA, and STB are plotted in green, pink, and orange in the 3D space, respectively. The brown sphere at the center represents the Sun ( $1 R_s$ ). (a): Front view of the shock surface superimposed with the compression ratio. The front view is defined as the view directly facing the AR. (b): Similar to (a) but from the back view of the shock surface, which is 180-degree rotating over the  $Z$  axis. (c)(d): Similar to (a)(b) but superimposed with the shock normal angle. (e)(f): Similar to (a)(b) but superimposed with the Alfvén Mach number.

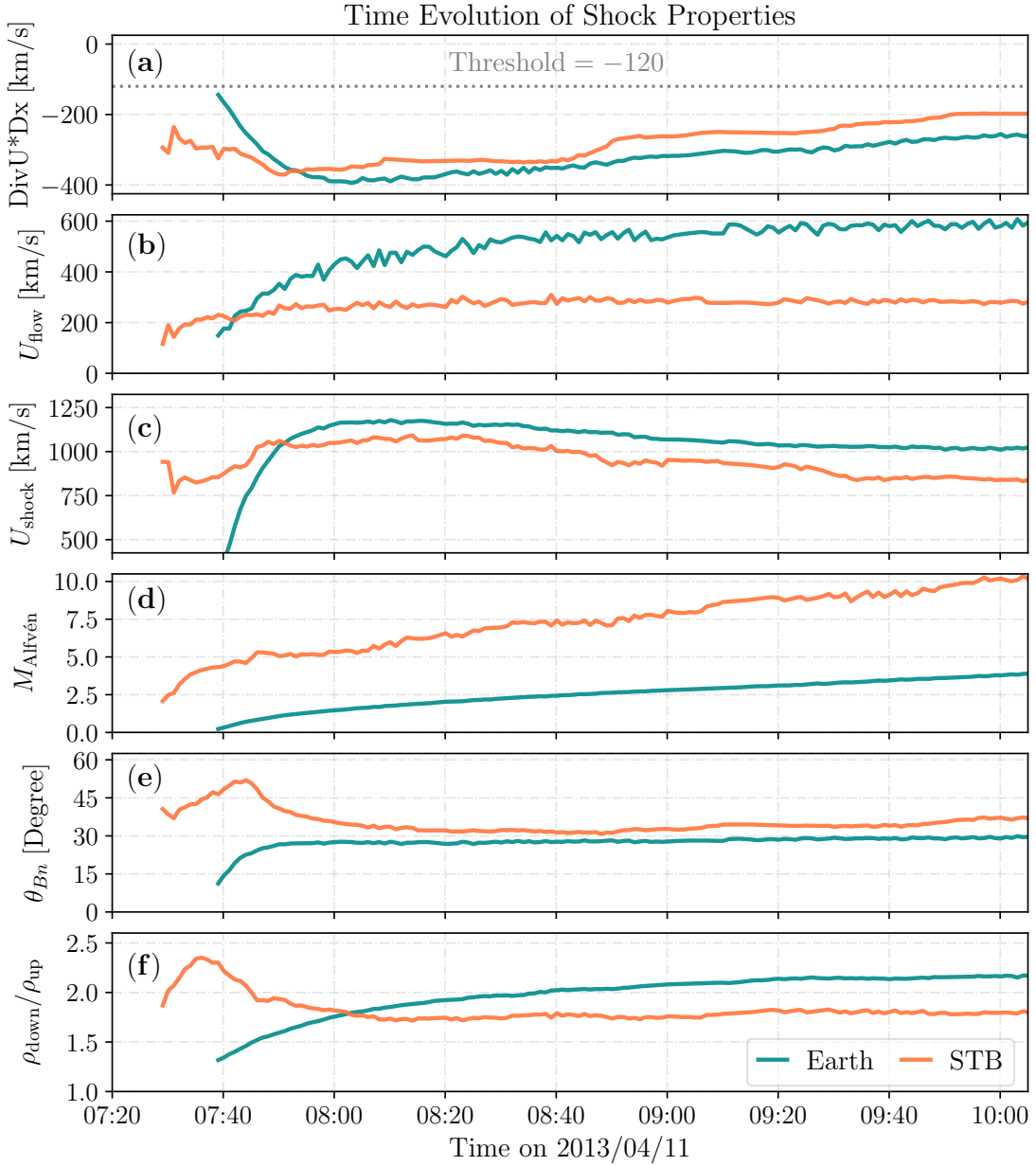


**Figure 8.** Time evolution of the shock properties at the intersection point of the shock surface and field lines connecting to Earth, and STB, plotted in green and orange, respectively. Six parameters are presented: (a) Divergence of velocity field times the cell size ( $\text{Div}U \cdot \text{D}x$ ) with the gray dotted line representing the threshold applied in this study,  $-120$  km/s; (b): Flow speed ( $U_{\text{flow}}$ ); (c) Shock speed ( $U_{\text{shock}}$ ); (d) Alfvén Mach number ( $M_{\text{Alfvén}}$ ); (e) Shock normal angle ( $\theta_{Bn}$ ); (f) Compression ratio calculated by the ratio of downstream density to upstream density ( $\rho_{\text{down}}/\rho_{\text{up}}$ ).

we use ( $\text{Div}U \cdot \text{D}x$ , in Figure 8(a)), flow speed ( $U_{\text{flow}}$ , in Figure 8(b)), shock speed ( $U_{\text{shock}}$ , in Figure 8(c)), Alfvén Mach number ( $M_{\text{Alfvén}}$ , in Figure 8(d)), shock normal angle ( $\theta_{Bn}$ , in Figure 8(e)), and compression ratio calculated by the ratio of downstream density to upstream density ( $\rho_{\text{down}}/\rho_{\text{up}}$ , in Figure 8(f)). In Figure 8, it is obvious that the time of magnetic connection to the shock surface in our simulations varies for different observers. Specifically, we launch the flux rope and let it erupt at 07:24 UT. Only 5 minutes later, at 07:29 UT, the STB is magnetically connected to the shock

surface, which is a stronger shock region, while the Earth has the magnetic connection at 07:39 UT, 15 minutes after the CME eruption, and it is a weaker shock region (also see Figure 7 for snapshots at 24 minutes). These differences indicate a more effective particle acceleration for STB than the Earth during the onset phase, explaining the fact that we see a more sharp onset at STB while the onset appears more gradual at Earth, as shown in Figure 3 and more clearly in Figure 5 of Lario et al. (2014).

As time progresses, for the field line intersection points, the shock normal angle and compression ratio tend to be a constant, while properties such as  $\text{DivU} \cdot \text{Dx}$ , flow speed, shock speed, and Alfvén Mach number continue to evolve, as demonstrated in Figure 8. At 10:00 UT, i.e., more than 2 hours after the CME eruption, our simulation results indicate that the shock compression ratio is higher at the intersection point of field line that connects the Earth ( $\sim 2.0$ ) than STB ( $\sim 1.8$ , see Figure 8(f)). Additionally, as inferred from Figure 8(e), both the regions of the intersection points appear to be quasi-parallel.

#### 4.4. SEP Fluxes and Evolutions

Once the simulation begins, AWSoM-R and M-FLAMPA run concurrently, and M-FLAMPA utilizes the plasma parameters coupled from the time-accurate AWSoM-R simulations in SC and IH. We follow 648 magnetic field lines that cover  $360^\circ$  in longitude and from  $-85^\circ$  to  $85^\circ$  in latitude on the solar surface. These field lines originate at a radial distance of  $2.5 R_s$  and are traced both inward and outward, extending to the inner and outer boundaries of the mesh domain. The starting points of the magnetic field lines are uniformly distributed on the sphere at  $2.5 R_s$ . In the following contents, we show different types of results from our simulations, and also perform model-data comparisons.

##### 4.4.1. $Z=0$ Plane Cut and Radial Distribution

Figure 9 shows a snapshot of simulation results on the  $Z_{\text{HGR}} = 0$  plane, at 4 hours after the CME eruption. The magnetic field lines connecting to the Earth, STA, and STB are shown from the north pole view and marked in green, pink, and orange with the corresponding labels, respectively. We can see from Figure 9(a) that the CME has entered into the IH region, and tell the CME-driven shock in Figure 9(b). Regions traversed by the shock exhibit simulated SEP fluxes, as demonstrated in Figure 9(c)(d) for particles with 2.4 MeV and 22 MeV, respectively. Notably, no SEP flux is simulated at STA, because it is not magnetically connected to the shock surface and we do not incorporate perpendicular diffusion in our model, as discussed before in Sections 2.3.4 and 4.3. Besides, due to spatial variations in the shock strength, the simulation results in Figure 9(c)(d) reveal different SEP flux levels across longitudes.

##### 4.4.2. 2D Spherical Distribution

Figure 10 shows the two-dimensional (2D) distribution of the energetic proton differential intensity on a logarithmic scale at three moments of time after the launch of the CME flux rope: 4 hours (top row), 12 hours (middle row), and 36 hours (bottom row). The distributions are presented for two energy channels: 2.4 MeV (left column) and 22 MeV (right column), corresponding to comparatively lower- and higher-energy protons. The  $x$ - and  $y$ -axes respectively represent the HGR longitude and latitude for a sphere at 1 AU. Locations of the Earth, STA, and STB are indicated by letters “E”, “A”, and “B” within green, pink, and orange circles, respectively. The location of the inserted flux rope on the Sun is marked as a blue square with the letter “F”, showing the relative location of

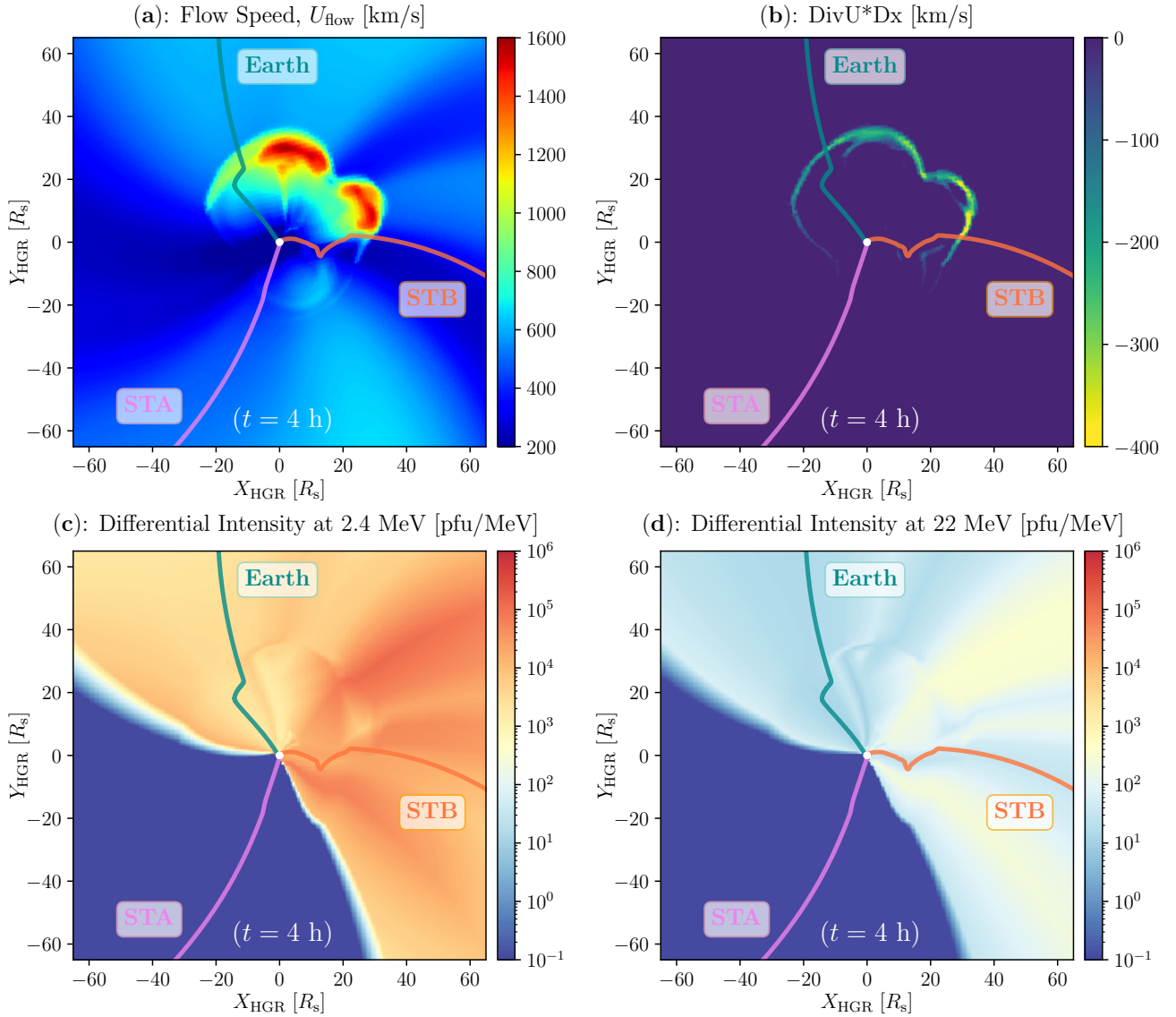


**Figure 9.** Simulation results in the equatorial plane ( $Z_{\text{HGR}} = 0$ ) at 4 hours after the launch of the CME flux rope. In each panel, HGR coordinates are used, and the FOV is set as  $-65 R_s \leq X_{\text{HGR}}, Y_{\text{HGR}} \leq 65 R_s$ . Field lines connecting to the Earth, STA, and STB are shown from the north pole view, plotted in green, pink, and orange, respectively, with corresponding labels next to the lines. The white spot at the center represents the Sun ( $1 R_s$ ). Panel (a) shows the flow speed. Panel (b) shows the DivU\*Dx parameter. Panels (c)(d) present the energetic proton differential intensity at 2.4 and 22 MeV, respectively, with colors saturated if the values exceeded the range of  $10^{-1} \sim 10^6$  pfu/MeV.

observers with respect to the CME (also see Figure 3(a)), which is the source of SEPs. A similar plot but for  $\geq 10$  MeV integral flux and with different computational schemes is presented in Figure 5 of Zhao et al. (2024).

Note that the traced 648 magnetic field lines in M-FLAMPA are not evenly distributed over the sphere at 1 AU. Here, we apply the Delaunay triangulation method (Delaunay 1934; Lee & Schachter 1980) to construct a skeleton of the sphere, which uses a set of points to effectively divide the plane into multiple triangular cells and tends to avoid the formation of narrow or sliver triangles. In Figure

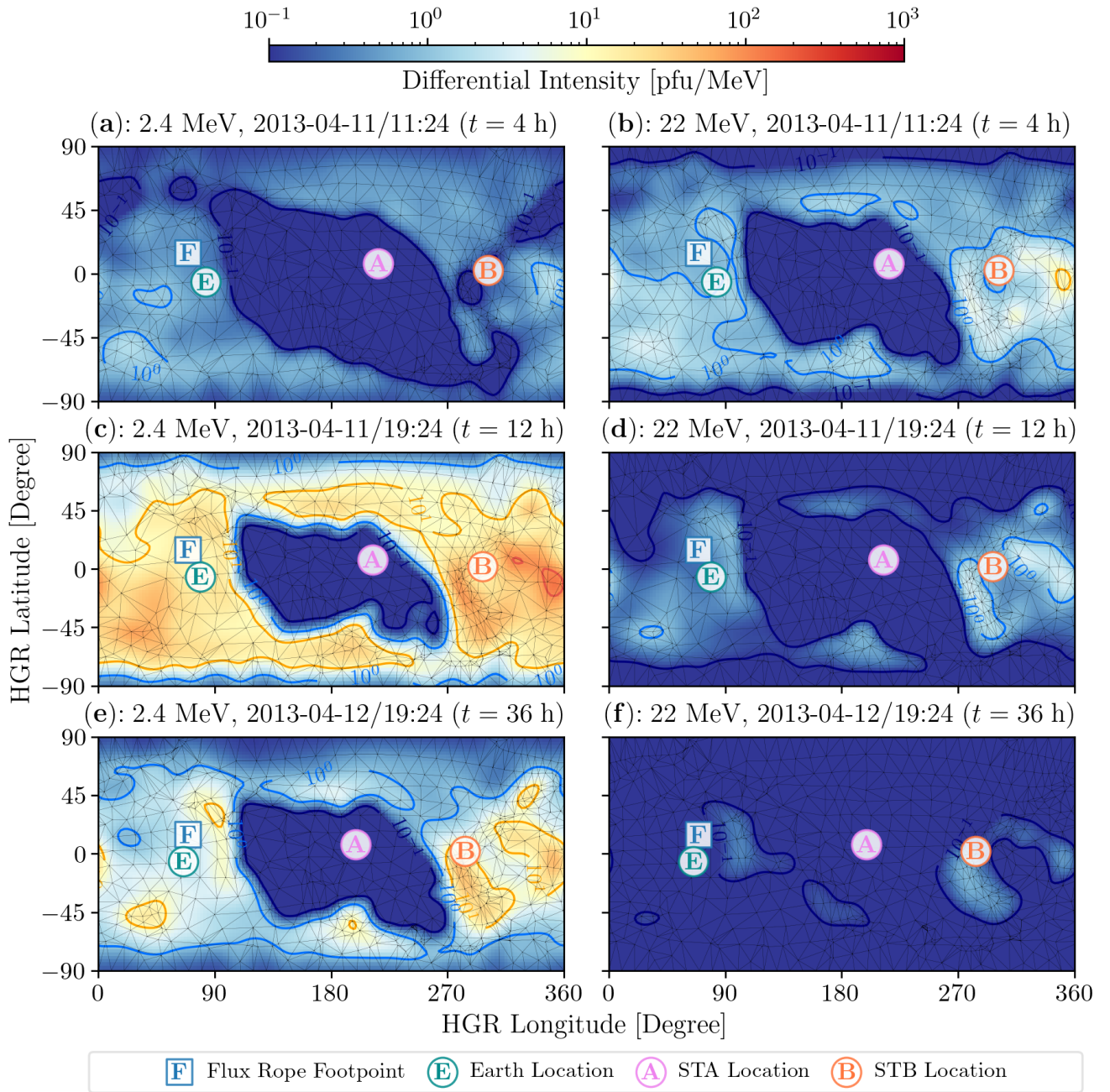


**Figure 10.** 2D distribution of the differential intensity at 2.4 MeV (left column) and 22 MeV (right column) on the 1 AU sphere, at 4 hours (upper row), 12 hours (middle row) and 36 hours (lower row) after the CME eruption. HGR longitude and latitude are used in all panels. In each panel, the flux rope footpoint on the sun is plotted as “F” in a square in blue, and the locations of Earth, STA, and STB are plotted as “E”, “A”, and “B”, in a circle in green, pink, and orange, respectively.

10, the vertices indicate where the field lines intersect the 1 AU surface, and the edges illustrate the skeletal representation of the 1 AU surface derived via Delaunay triangulation. With the skeleton and the differential intensity values at each vertexes, we are able to interpolate the intensity across any location of interest on the full 1 AU sphere. In each panel of Figure 10, the curly contour lines represent the differential intensity for each order of magnitude.

Furthermore, by comparing the distributions at 2.4 MeV and 22 MeV energies in Figure 10, we can tell that the higher-energy protons generally arrive the 1 AU surface earlier than the lower-energy protons. We can observe the phases of increase, peak, and decay for the differential intensity distribution at 2.4 MeV in Figure 10(a)(c)(e), while the 22 MeV particles travel faster than 2.4 MeV particles, so the differential intensity at 22 MeV just appears to decay in Figure 10(b)(d)(f).

Distinct variations in energetic proton intensities can also be found across longitudes and latitudes in Figure 10. For instance, in all 3 time slices (4, 12, and 36 hours after the flux rope eruption), the differential intensity around STA is noticeably orders of magnitude lower than that at Earth and STB. This aligns with the observations in Figure 3 and simulation results in Figure 9, which shows no SEP fluxes in the regions near STA due to the lack of magnetic connectivity (see Section 4.3) and the absence of perpendicular diffusion in our model. Hereafter, we place our emphasis on the SEPs at Earth and STB. The differential intensity at STB consistently appears more red-toned than at Earth, indicating that the flux at STB is overall higher than at Earth. Since the IMF follows the Parker spiral in general (e.g., Xie et al. 2019; Zhao et al. 2019), the SEP flux typically concentrates around  $40^{\circ}$ – $75^{\circ}$  eastern of the flux rope location, which also depends on the corona and interplanetary magnetic field configurations (e.g., Lario et al. 2006; Richardson et al. 2014, 2018; Paassilta et al. 2018). As shown in Figure 10(b)(c), the peak energetic proton intensity of both energies occurs between  $270^{\circ}$  and  $360^{\circ}$ , which is  $70^{\circ}$ – $120^{\circ}$  eastern of the flux rope location. Note that in our simulation, we assume a uniform injection coefficient across the shock front, i.e., independent of the shock obliquity, as described in Section 2.3.5. Therefore, the 2D distribution of the energetic particles reflects the collective effects of the shock strength, the ambient plasma density and the temperature of the flux rope.

#### 4.4.3. Time Profiles

In Section 2.3.5, we introduce the scaling factor and set as 1.2 in this study, in order to improve the alignment between the simulation results and observational data. Further interpretations are provided in Section 4.5 of Zhao et al. (2024). Based on the skeleton shown in Figure 10, we interpolate the differential intensities at the Earth and STB where SEP fluxes are observed. Each panel of Figure 11 presents the calculated differential intensities across 6 energy channels, which we compare with particle measurements from *SOHO*/ERNE, and STB/LET and HET, respectively. These 6 energy channels for each spacecraft are chosen between  $\sim 2$  MeV and  $\sim 40$  MeV and shown in different colors. In Figure 11, each energy channel, displayed with the same color but originating from different instruments, represents a close energy range, e.g., energy channel in blue is for 4.0–5.0 MeV in *SOHO*/ERNE and 4.0–6.0 MeV for STB/LET. Simulation results using the Poisson bracket scheme are plotted as dashed curves, while the observational data are presented as solid lines. Overall, our model successfully reproduces the time profiles across the energy channels for both *SOHO* and STB, with value discrepancies within roughly half an order of magnitude. For comparable energy levels, which are represented in the same color in Figure 11, the simulation results indicate a slightly higher intensity at STB and a faster decay compared to Earth. In fact, this is a combined effect of the slight differences in energies, and more significantly, the positional and resulting shock strength differences between STB and Earth, as illustrated in Figures 7 and 10, and texts to them.

Besides, for both *SOHO* and STB, the onset phases in simulations basically well match with the observations in all 6 energy channels, showing a clear velocity dispersion pattern. Specifically, for *SOHO*/ERNE, the SEP peak intensities arrive about 2 hours faster in the simulations than in the observations, in the two higher energy channels (20.0–25.0 and 32.0–40.0 MeV). In the two lower

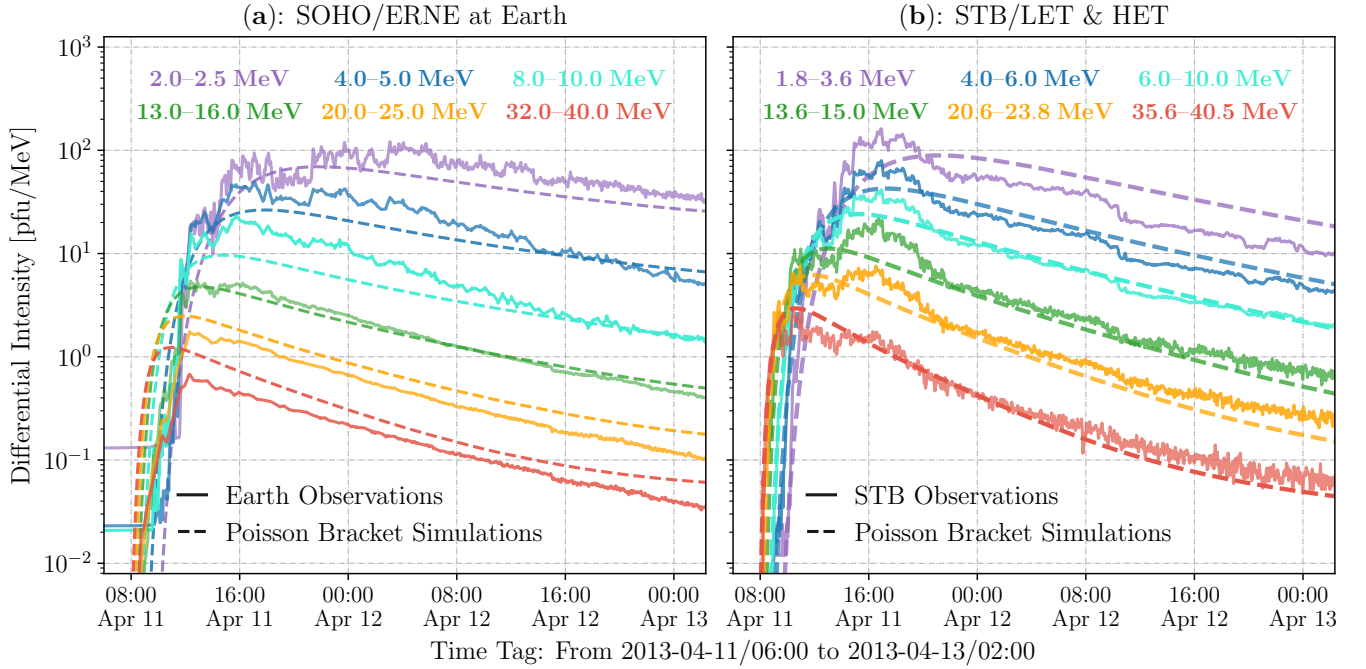


**Figure 11.** Comparison of the time intensity profiles between simulation results and observations across 6 energy channels that range from 2 MeV to 40 MeV and are slightly different for each spacecraft. In each panel, the observational data are plotted in solid curves, while the calculated intensities with the Poisson bracket scheme are plotted in dashed curves. Panel (a) shows the comparison for *SOHO/ERNE* observations and the simulation results using the Poisson bracket scheme. Panel (b) shows the comparisons for STB with different energy channels, sharing the same range of differential intensity in the  $y$ -axis.

energy channels (2.0–2.5 and 4.0–5.0 MeV), the SEP peak intensities arrive slightly slower in the simulations than in the observations. In the two intermediate energy channels (8.0–10.0 and 13.0–16.0 MeV), the onset phases appear to be comparable between simulations and observations. In terms of the time profiles in STB/LET and HET, we can tell an irregular structure in particle measurements around 17:00 UT on April 11 in Figure 11(b). Aside from this short-term irregularity, the onset phases in the simulations are comparable to those in observations across all energy channels selected, except for the lowest energy channel selected (1.8–3.6 MeV), where the simulated SEP peak intensities occur about 4 hours later than observed. Furthermore, the decay phases across all 6 energy channels for both *SOHO* and STB exhibit strong concordance between the simulations and observations, with discrepancies of values within a factor of  $\sim 2$ .

#### 4.4.4. Energy Spectrum

We further investigate the time-evolving energy spectrum. Figure 12(a)–(c) depicts the SEP spectra at 4, 12, and 36 hours after the launch of the CME flux rope, respectively. In each panel, simulation results are represented by curves, while observational data are marked as scattered points with energy-related error bars. The *SOHO/ERNE* data are marked as green circles, and the simulated spectra at Earth are plotted in green. Note that *SOHO/ERNE* data are subject to saturation effects, which may lead to inaccuracies in particle counts at high flux levels (Miteva et al. 2018, 2020; Kühl & Heber 2019). In order to enhance the model-data comparison at Earth, we also include particle measurements from the Energetic Proton, Electron and Alpha Detector (EPEAD, Onsager et al.

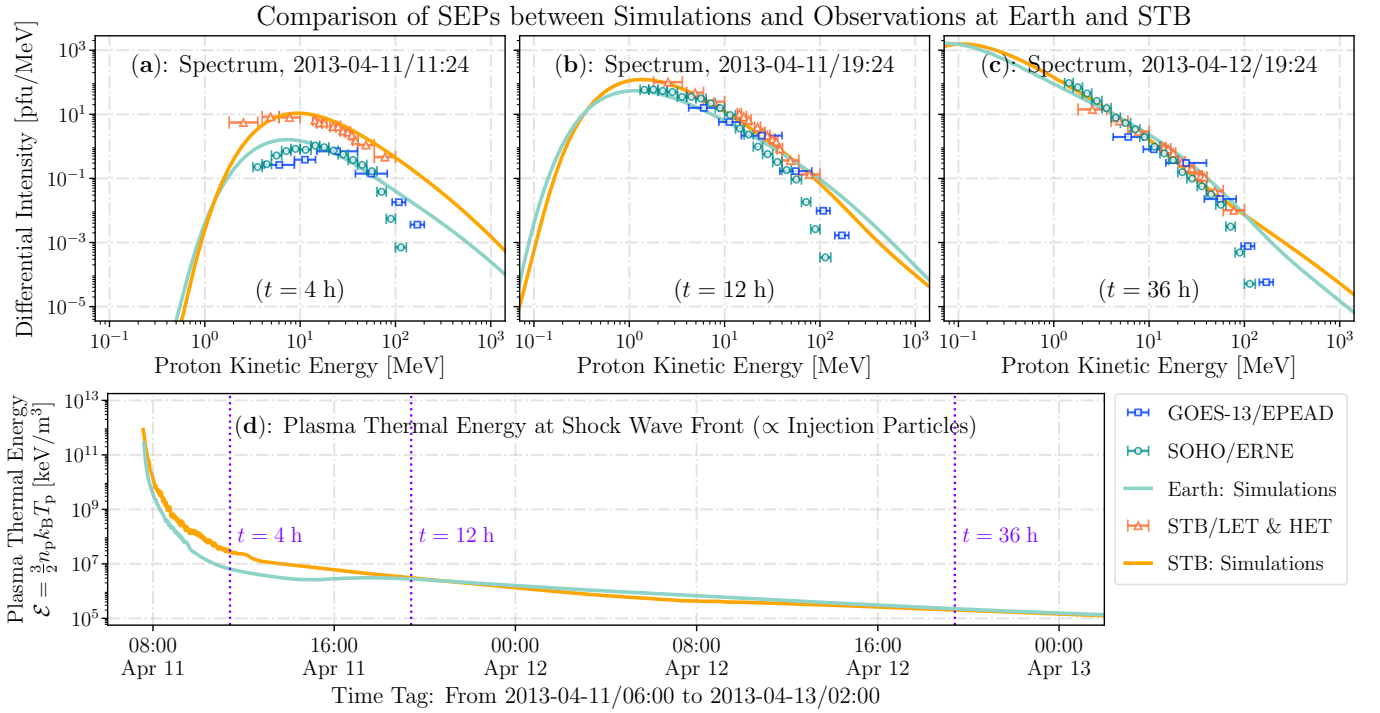


**Figure 12.** Comparison of SEPs between simulations and observations at Earth and STB. Panels (a)–(c) present the SEP spectra at Earth and STB at three time intervals after the CME flux rope eruption: (a) 4 hours, (b) 12 hours, and (c): 36 hours. In each panel, observational data are plotted as scattered points, while simulation results are shown as curves. Data from *GOES-13/EPEAD* are denoted by blue squares, with the so-called “effective energies” calibrated by Bruno (2017). Measurements from *SOHO/ERNE* are marked as green circles, and the simulated spectra at Earth are plotted in green. Similarly, orange triangles indicate data from STB/LET and HET instruments, and orange curves represent the simulated spectra at STB. Panel (d) shows the time profile of the ambient plasma thermal energy at the shock wave front, using the same legends as in Panels (a)–(c). Additionally, three purple dotted lines mark the moments of 4, 12, and 36 hours after the eruption, respectively.

1996; Sellers & Hanser 1996) on board the *GOES-13*, which are shown as blue squares with energy bins calibrated by Bruno (2017). Data from STB/LET and HET instruments are marked as orange triangles, and the simulated spectra at STB are plotted in orange.

On the whole, the simulation results align well with the particle measurements. In Figure 12(a), the SEP flux at STB is about half an order of magnitude higher than at Earth, 4 hours after the flux rope eruption. Later on, the SEP fluxes at these two locations become more similar, as illustrated in Figure 12(b)(c). To elaborate these variations of SEP flux levels, we examine the time-evolving properties at the shock surface. According to Equation 20, the number of particles injected at the shock wave front is proportional to the ambient plasma thermal energy (density, per volume), which is notated as  $\mathcal{E} \equiv \frac{3}{2}n_p k_B T_p$  hereafter. Figure 12(d) demonstrates the time evolution of the plasma thermal energy at the shock wave front, with the same legends used in Figure 12(a)–(c) and three purple dotted lines indicating 4, 12, and 36 hours after the eruption, respectively. During the first a few hours, the plasma thermal energy is slightly higher (by a factor of  $\sim 3$ ) at the intersection of the STB-connected magnetic field line and the shock surface, compared to the Earth, attributed to the propagating CME and its interaction and distortion with the background solar wind. Over time, the



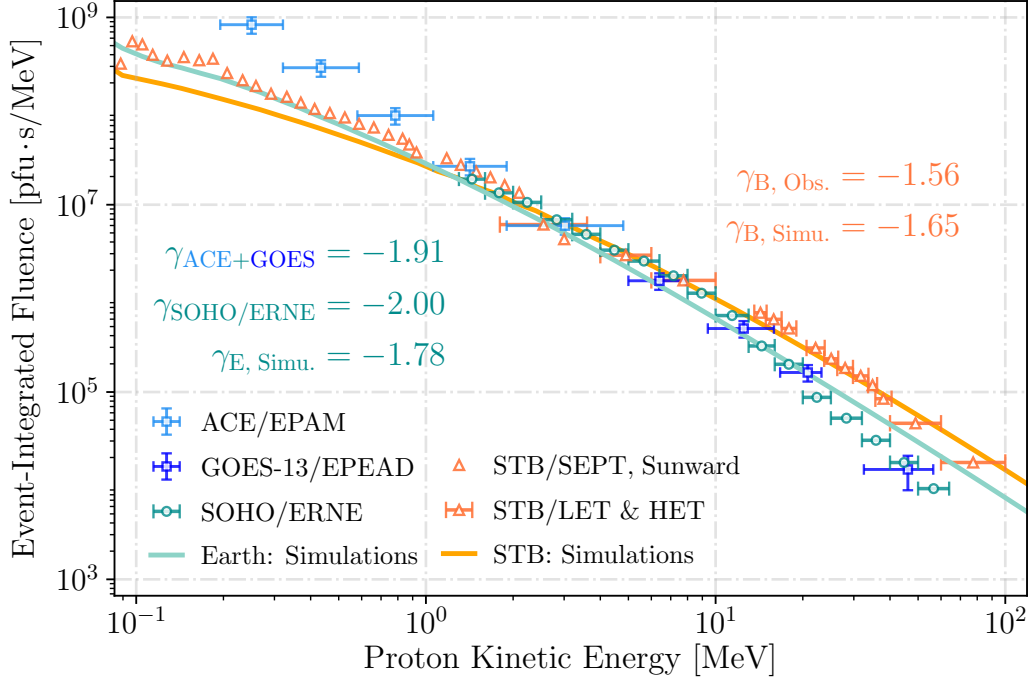


**Figure 13.** Event-integrated fluence spectrum at Earth and STB. Observational results are plotted as scattered points, while simulation results are plotted as curves. At Earth, ACE/EPAM fluence is plotted in light blue, and *GOES*-13/EPEAD fluence is plotted in deep blue, taken from Bruno & Richardson (2021). The SOHO/ERNE fluence and the simulated fluence at Earth are plotted in green. The sunward SEPT, LET and HET fluence and the simulated fluence at STB are plotted in orange. Fitted exponential indices are included for both observations and simulations at Earth and STB in corresponding colors.

plasma thermal energy tends to be similar at the two intersection points on the shock surface. This explains the differences and similarities regarding to the SEP flux magnitude observed at the Earth and STB in Figure 12(a)–(c).

To evaluate the overall event-integrated fluence, we accumulate the SEP fluxes over time among multiple energy channels, as illustrated in Figure 13. We also include data from STB/SEPT (Sunward) and ACE/EPAM at comparatively low energies (less than a few MeVs) in order to perform a more comprehensive model-data comparison. The *GOES*-13/EPEAD and ACE/EPAM data are taken from Bruno & Richardson (2021). Particle measurements of ACE/EPAM are marked as light blue squares with error bars in energies and fluences, while data from STB/SEPT are represented by scattered triangles without error bars. We calculate the exponential index of the fluence spectrum in the range of 1 ~ 50 MeV for both simulations and observations at Earth and STB. Results are attached to Figure 13, showing that the exponential indices from simulations are basically consistent with the ones derived from observations. A slightly harder fluence spectrum at STB ( $\gamma_{B, \text{Simu.}} = -1.65$ ) than the Earth ( $\gamma_{E, \text{Simu.}} = -1.78$ ) is reproduced from our simulations. Note that Figure 13 is the event-integrated fluence spectrum; it reflects the efficiency of particle acceleration and/or energy loss during its transport, throughout the entire SEP event.

In spite of the overall consistency in model-data comparisons, discrepancies can still be found in the time-evolving spectrum at energies  $\gtrsim 50$  MeV in Figure 12(a)–(c), and also the fluence spectrum at energies  $\lesssim 1$  MeV in Figure 13. These discrepancies suggest a potential overestimation of particle

acceleration and/or underestimation of particle energy loss due to adiabatic cooling during the particle transport process. The slightly mismatched patterns in spectra also highlight the need for more accurate estimations of the MFP and diffusion coefficient, particularly near the shock wave front and upstream regions (see [Desai & Giacalone 2016](#); [Guo et al. 2024](#), and references therein). These factors are discussed in greater detail in Section 5.

## 5. DISCUSSIONS

The results presented in Section 4 suggest a number of discussion points related to SEP studies, including the background solar wind, CME flux rope mechanisms, shock geometry, as well as the particle acceleration and transport processes. In the following contents, we discuss each of these aspects from the numerical modeling perspective.

### 5.1. *Background Solar Wind*

First of all, all our time-accurate simulations are run based on the steady-state solar wind solutions as outlined in Sections 2.1 and 4.1. In our simulations, the solar wind speed is reported as  $\gtrsim 500$  km/s at Earth and STA while it is  $\sim 300$  km/s at STB. Compared with the *in-situ* observations in Table 2, discernible discrepancies are evident for the solar wind speed at Earth, which may partially impact the transport of the CME flow as well as energetic particles in the IP space (e.g., [Rodriguez et al. 2016](#); [Kouloumvakos et al. 2022](#)). However, such factors are important to the SEP studies within stream/co-rotating interaction regions (e.g., [Zhao et al. 2016a](#); [Wijsen et al. 2021](#); [Tao et al. 2024](#); [Zhu & Shen 2024](#)), which is not incorporated in this event and outside the primary focus of this study. Besides, among the solar wind parameters, the magnetic field turbulence is particularly important to the acceleration and transport processes of SEPs, which will be discussed along with the MFP in more detail in Section 5.3.

As stated in Section 2.1, we process the GONG magnetogram using the PFSS model, setting the source surface height to  $2.5 R_s$ . We recognize that adjusting the boundary height in the PFSS model could potentially improve the agreement between the simulated solar wind parameters and observations, which remains an ongoing area of study (e.g., [Lee et al. 2011](#); [Huang et al. 2024a](#), and references therein). Such refinements may further enhance the accuracy of SEP modeling. Nevertheless, we derive the optimal set of input parameters with uncertainty quantification in the current runs, which are reasonably suitable for SEP studies ([Huang et al. 2024b](#); [Zhao et al. 2024](#)). Also, the solar wind parameters are obtained by solving the stream-aligned MHD equations using the AWSoM-R model ([Sokolov et al. 2022](#)). With this approach, the magnetic field lines and plasma stream lines are “nudged” to keep their alignments, avoiding unrealistic “V-shaped” magnetic reconnection along the HCS. As known, the HCS has a profound impact on the particle drift and magnetic connectivity (e.g., [Moradi & Giacalone 2022](#); [Cheng et al. 2024](#); [Liou & Wu 2024](#)). This field alignment capability in our model highlights its strength in producing realistic magnetic configurations in the SC and IH regions, making them well-suited for studies of magnetic connectivity and SEP transport.

### 5.2. *CME and Its Driven Shock*

In our simulations, the CME is initialized by inserting a force-imbalanced GL flux rope on top of the parent AR, as illustrated in Figure 1(c). This GL flux rope erupts immediately after the placement, propagating into the SC and IH regions. The CME can significantly perturb the ambient solar wind plasma, generating fast-mode shocks at its leading edge where particles are accelerated effectively, as

depicted in Figures 5 and 7. Actually, the geometry of the shock wave front is primarily dictated by the inserted flux rope and its interaction with the background solar wind (e.g., Gosling & McComas 1987; Kilpua et al. 2017; Manchester et al. 2017, and references therein). Hence, the CME magnetic structure and propagation dynamics play a critical role to the shock geometry and also SEPs (e.g., Manchester IV et al. 2005; Li et al. 2021; Palmerio et al. 2021, 2022; Wijzen et al. 2023b), highlighting the importance of accurately specifying flux rope parameters and understanding the underlying physical mechanisms. For more sophisticated considerations, alternative flux rope initiation mechanisms will be investigated in the future, such as the TD and STITCH models introduced in Section 2.2. For further details about the state-of-the-art flux rope models, we refer readers to read the papers by Titov & Démoulin (1999); Antiochos (2013); Dahlin et al. (2022); Sokolov & Gombosi (2023) and references therein.

As the CME flux rope propagates, the shock surface is driven and also captured by our modeling tool as demonstrated in Section 4.3. The shock properties, particularly the injection particles and compression ratio, are crucial for SEP studies as they determine the number and acceleration efficiency of energetic particles, representing as the flux magnitude in spectrum and the spectral index (Ellison & Ramaty 1985; Ellison et al. 1995; Prinsloo et al. 2019). By our shock capturing tool, the shock surface is not as simple as modeled in previous studies (e.g., Zhang et al. 2023; Cheng et al. 2024, and papers listed in Section 4.3). As shown in Figure 7, the shock wave front is not symmetric or uniform, but consists of multiple pieces of smooth spheres instead. Besides, shock properties vary significantly over small angular separations as illustrated clearly in Figure 7(b)(d)(f). These findings highlight the necessity of high-resolution shock capturing and field-line tracing. In this study, we employ the AMR technique and use sufficiently small spatial steps for field-line tracing to ensure the accuracy. However, we note that the shock surface is extracted along radial lines originating from a longitude-latitude grid, which may be lack of communications among different radial lines, possibly resulting in artifacts as evidenced by the rippled values and colors in Figure 7(a)(e). In future work, we aim to improve our shock capturing tool with better visualizations to address these artifacts.

In comparisons between the simulated and observed SEP fluxes, a scaling factor is incorporated into our particle tracker, M-FLAMPA, to achieve better agreements. In fact, the determination of this scaling factor is influenced by the properties of the CME-driven shock, including the spatial extension and strength of the shock surface. Besides, the magnetic connectivity between the spacecraft’s location and the shock wave front also impacts the scaling factor, as indicated by the spatial variations of the shock surface in Figure 7. Note that M-FLAMPA currently does not account for the perpendicular diffusion for SEPs due to its complexity, as stated in Section 2.3.4. This omission can also affect the scaling factor. As anticipated, we cannot reproduce the very slight and gradual enhancement in particle fluxes at low energies (1.8–3.6 MeV) shown in Figure 3(d). As a result, the value of this scaling factor employed in this study does not directly reflect the abundance of suprathermal protons at the injection energy of 10 keV, which are accelerated through the DSA process. Further interpretations and more sophisticated factors that can impact the scaling factor have been discussed in Zhao et al. (2024).

### 5.3. Influence of MFPs on SEP Acceleration and Transport

Based on the DSA mechanism, the diffusion coefficient plays a critical role in the acceleration and transport processes of energetic particles. In M-FLAMPA, only the parallel diffusion coefficient is considered, calculated by the parallel MFP ( $\lambda_{xx}$ ) and particle speed as shown in Equation 11. Here,

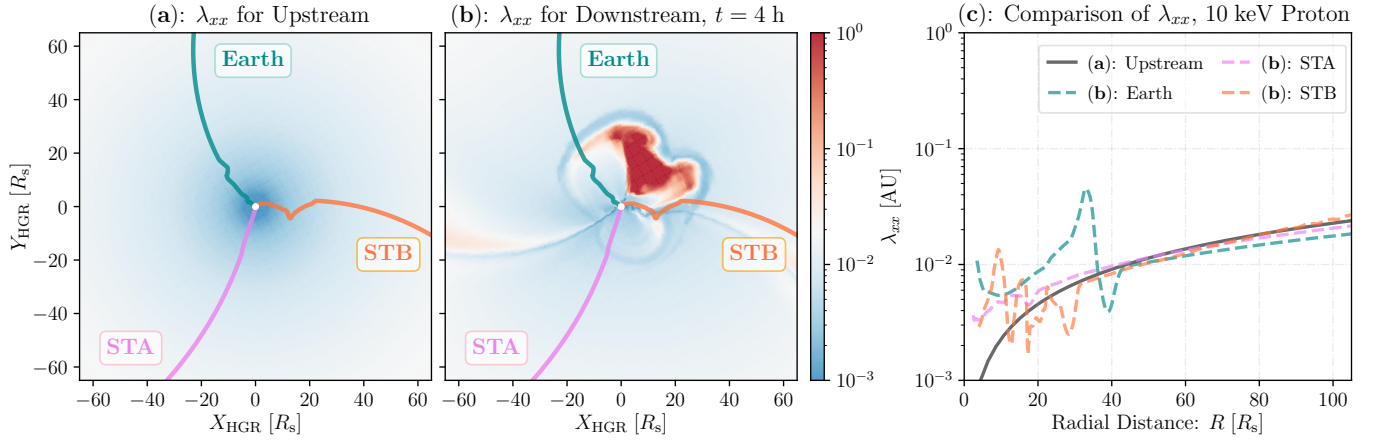


**Figure 14.** Parallel MFP ( $\lambda_{xx}$ ) comparison. (a):  $\lambda_{xx}$  for the shock upstream in the  $Z_{HGR} = 0$  plane, following Equation 14. (b):  $\lambda_{xx}$  for the shock downstream in the  $Z_{HGR} = 0$  plane at  $t = 4$  h after the CME flux rope eruption, following Equation 17. In Panels (a)(b), HGR coordinates are used, with the FOV spanning  $-65 R_s \leq X_{HGR}, Y_{HGR} \leq 65 R_s$ . The contour colors in Panels (a)(b) saturate for  $\lambda_{xx}$  values beyond  $10^{-3} \sim 10^0$  AU. Magnetic field lines connecting to the Earth, STA, and STB are shown from the north pole view. They are plotted in green, pink, and orange, respectively, with corresponding labels positioned next to each line. The white spot at the center represents the Sun ( $1 R_s$ ). (c): The comparison of  $\lambda_{xx}$  for the injected protons at 10 keV. The black solid curve indicates the MFP calculated by Equation 14 for the upstream region, while the dashed curves represent the MFP calculated by Equation 17 for the downstream region, plotted in the corresponding colors for each spacecraft as used in Panels (a)(b). The colorbar axis in Panel (b) and the  $y$ -axis of Panel (c) share the same label tag.

we further investigate and discuss the effects of the parallel MFP, which is derived from QLT (e.g., Li et al. 2003; Sokolov et al. 2004; Borovikov et al. 2019, and references therein) but manipulated differently in shock upstream and downstream regions.

In the upstream (pre-shock) regions, the free parameter  $\lambda_0$  is chosen as 0.3 AU to match with the  $D_{xx}$  based on long-term *PSP* solar wind turbulence observations (Chen et al. 2024a). Note that the self-generated Alfvén waves produced in the vicinity of a shock-wave front have been demonstrated to have important consequences for SEP elemental abundance variations (Ng et al. 1999; Tylka et al. 1999; Sandroos & Vainio 2007) and the evolution of SEP anisotropies (Reames et al. 2001; Petrosian 2012). In the downstream (post-shock) regions, the parallel MFP incorporates the effects of self-generated Alfvén wave turbulence simulated by AWSoM-R. While Equation 17 calculates  $\lambda_{xx}$  in the downstream, it is also applicable to pre-shock regions for the Alfvén wave turbulence in the background solar wind, and should yield comparable results as derived from Equation 14.

In Figure 14, we show the comparisons of  $\lambda_{xx}$  in the equatorial plane, calculated by both approaches. Figure 14(a) presents the  $\lambda_{xx}$  calculated by Equation 14, while Figure 14(b) presents the  $\lambda_{xx}$  calculated by Equation 17 at 4 hours after the CME eruption, with the field lines connecting to the Earth, STA, and STB plotted in the view of the north pole in green, orange, and pink, respectively. In Figure 14(b), the regions with dramatically increased  $\lambda_{xx}$  imply the disruptions of the flux rope, and the regions with slightly decreased  $\lambda_{xx}$  ahead of the flux rope indicate the CME-driven shock wave front. Farther away in Figure 14(b),  $\lambda_{xx}$  is for the MFP in background solar wind turbulence, shown at the same magnitude as in Figure 14(a). In Figure 14(c), we gather the  $\lambda_{xx}$  values at the injection energy of 10 keV for protons, calculated by Equations 14 and 17 for the field lines connecting to the

Earth, STA and STB. As we can tell from Figure 14(c), the far-upstream part lies in good agreements. With well magnetic connectivity of both the Earth and STB to the shock surface, around half an order of magnitude smaller  $\lambda_{xx}$ , compared with  $\lambda_{xx}$  in the nearby background solar wind, can be found in the downstream near the shock surface in Figure 14(c). As known, in the DSA process, particles in the downstream region diffuse toward the shock front due to magnetic turbulence. This slightly smaller estimation of downstream  $\lambda_{xx}$  implies stronger scattering effects and can lead to a higher acceleration efficiency of particles, producing higher intensities of high-energy particles as demonstrated in Figures 12 and 13.

Another contributing factor to the overestimation of particle accelerations is the acceleration time scale. As introduced in Section 1, the SEP energy spectrum often exhibits an exponential rollover, showing a double power-law feature with a break energy (Ellison & Ramaty 1985; Band et al. 1993; Li et al. 2009). The shock finite lifetimes and sizes for particle accelerations are believed to be one of the key reasons shaping this feature (e.g., Zhao et al. 2016b, 2017; Kong et al. 2019). A useful quantity in this context is the acceleration time (notated as  $\tau_a$ ), which is the time required to accelerate particles from a particular injected energy (or equivalent momentum,  $p_{inj}$  used below) to a higher energy (notated as  $p$  for its equivalent momentum) at a planar shock (e.g., Drury 1983; Ellison & Ramaty 1985):

$$\tau_a = \frac{3}{U_{n,up} - U_{n,down}} \int_{p_{inj}}^p \left( \frac{D_{xx,up}}{U_{n,up}} + \frac{D_{xx,down}}{U_{n,down}} \right) \frac{dp'}{p'}, \quad (26)$$

in which  $U_n$  denotes the flow speed normal to the shock in its rest frame as notated in Equation 23, and  $p'$  is a dummy variable. According to Equation 26, there is an upper limit to the possible momenta which particles can achieve within each finite time step. While this aspect is inherently significant in understanding acceleration processes, its direct influence is not explicitly accounted for in our model due to our focus on solving the particle distribution function by implementing the TVD Poisson bracket scheme. Future work could further refine this aspect, as well as more careful manipulations of the self-generated Alfvén turbulence in downstream regions, to enhance the physical fidelity of the simulations.

Moreover, the upstream MFP can significantly influence the particle transport process, as reflected by the SEP time profiles and spectra (e.g., Qin et al. 2006; Strauss & Le Roux 2019; Niemela et al. 2023; Zhong et al. 2024; Wang & Guo 2024). In the previous sections, we set the free parameter for the upstream MFP ( $\lambda_0$  in Equation 14) as 0.3 AU. Although  $\lambda_0 = 0.3$  AU with Equation 11 based on QLT has been validated against Equation 16 taken from Chen et al. (2024a) as shown in Figure 2, many assumptions about the dependency of  $D_{xx}$  on the radial distance have been made as  $D_{xx} \sim r^\ell$  in many SEP transport models with  $\ell$  varying from 0 to 2 (e.g., Qin et al. 2004; Zhang et al. 2009; Dröge et al. 2010; Giacalone et al. 2020). For the long-term solar wind magnetic field turbulence observations, although results from Chen et al. (2024a) are comparable to previous studies such as Erdős & Balogh (2005), there are still various factors that can influence the turbulence strength and the estimation of  $D_{xx}$ , such as the IP transients (e.g., Desai & Giacalone 2016; Pitňa et al. 2021) and switchbacks (e.g., de Wit et al. 2020; Shoda et al. 2021). As stated in Chen et al. (2024a), the manipulations for estimating  $D_{xx}$  from turbulence observations can also be optimized by taking into account the magnetic field turbulence anisotropy (e.g., Bieber et al. 1994; Matthaeus et al. 2003; Shalchi et al. 2009; Bandyopadhyay & McComas 2021). As a result, the optimal value  $\lambda_0$  for the upstream MFP may vary from event to event in the practical application.

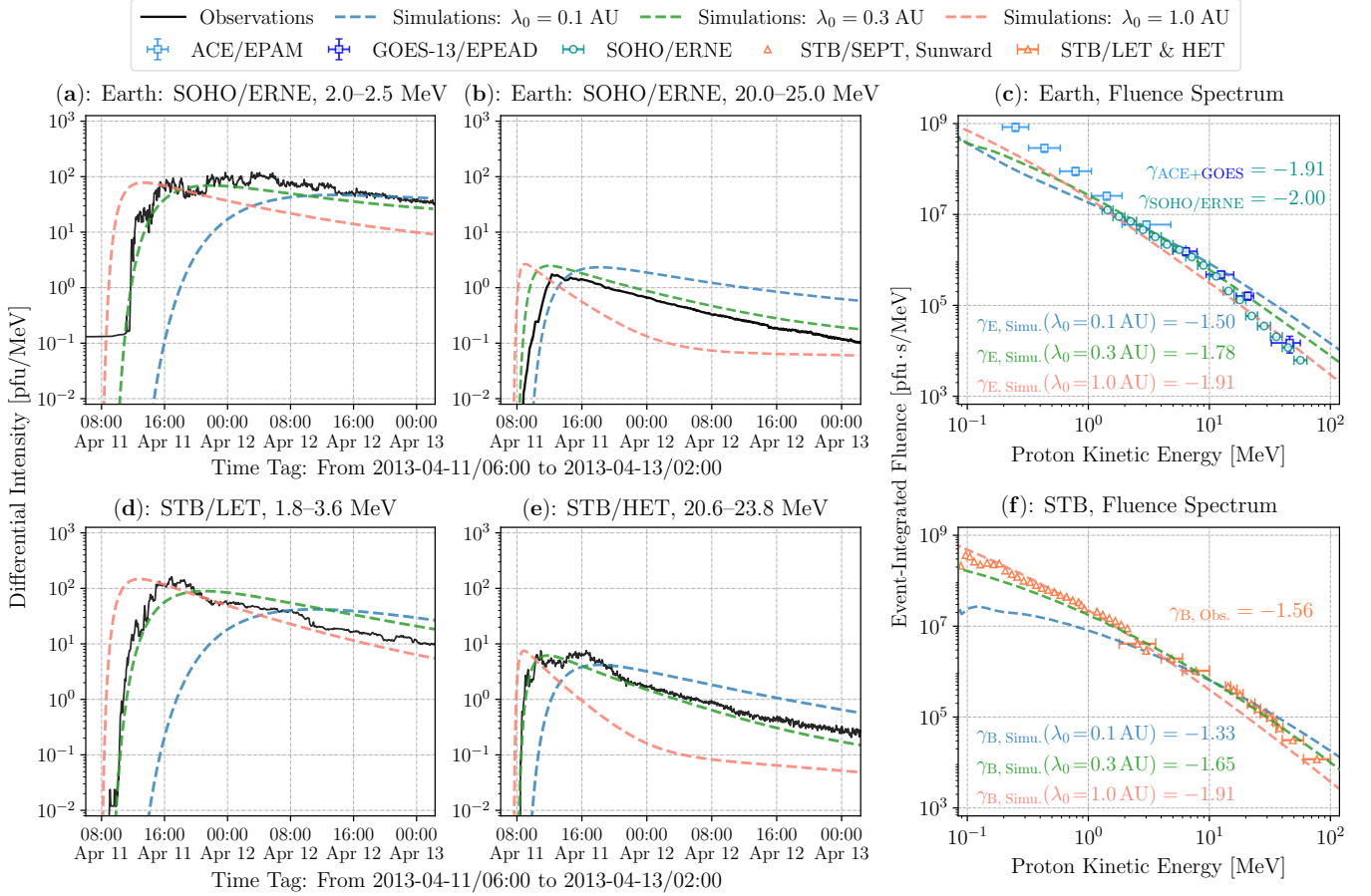


**Figure 15.** Results with different MFPs. (a)(b): The SEP intensity-time profiles at Earth in the energy ranges 2.0–2.5 MeV and 20.0–25.0 MeV, representing comparatively lower and higher energies, respectively. (c): Comparison of fluence spectra at Earth. (d)(e): The SEP intensity-time profiles at STB in the energy ranges 1.8–3.6 MeV and 20.6–23.8 MeV, corresponding to comparatively lower and higher energies, respectively. (f): Comparison of fluence spectra at STB. In each panel, simulation results are shown for three different MFP values, with  $\lambda_0$  in Equation 14 set to 0.1, 0.3, and 1.0 AU, represented as blue, green, and red dashed curves, respectively. Observational data are plotted as solid black lines for time series in Panels (a)(b)(d)(e), and marked as scattered points for the fluence spectrum in Panels (c)(f). The observational data in Panels (c)(f) follow the same legend style as used in Figure 13. Fitted exponential indices of the fluence spectrum are included for both observations and simulations using different MFPs at Earth and STB, displayed in the corresponding colors for the  $\lambda_0$  value.

For this event, we also explore the variations of SEP time profiles and fluence spectrum caused by different values of  $\lambda_0$ . In Figure 15, we present the intensity-time profiles and fluence spectra for both the Earth and STB. Panels (a) and (c) display the lower-energy profiles, with 2.0–2.5 MeV from *SOHO/ERNE* in Panel (a) and 1.8–3.6 MeV from *STB/LET* in Panel (c). Panels (b) and (d) correspond to the higher-energy profiles, featuring 20.0–25.0 MeV from *SOHO/ERNE* in Panel (b) and 20.6–23.8 MeV from *STB/HET* in Panel (d). The fluence spectra for Earth and STB are shown in Panels (e) and (f), respectively. In each panel, we show the observational data compared to the simulations for  $\lambda_0$  values of 0.1, 0.3 and 1.0 AU, in which the simulation data are respectively marked as blue, green, and red dashed curves. Particle measurements are plotted as black solid curves in

the intensity-time profiles, and represented as scattered points following the legend style in Figure 13. Fluence spectral indices are included for both observations and simulations with different MFPs, written in corresponding colors in Panels (c) and (f).

The SEP time profiles (see Figure 15(a)(b)(d)(e)) demonstrate that not only the absolute flux level, but also the onset and decay phases are sensitive to the value of MFPs. Similarly, fluence spectra (see Figure 15(c)(f)) show that different MFPs lead to a softer or harder fluence spectrum. While simulations with  $\lambda_0 = 0.3$  AU achieves excellent agreement with the intensity-time profiles, discrepancy remain in the fluence level and the spectral index compared to observations at both Earth and STB. These comparisons reveal the complexity of accurately estimations of upstream MFPs, and also highlights the significance with respect to the transport process of SEPs. In fact, the transport of SEPs in the IP medium involves a range of different physical processes, including magnetic focusing, adiabatic cooling, and the parallel and perpendicular diffusion (Northrop 1963; Roelof 1969; Skilling 1971; Kóta 1997). All of these processes depend intricately on the properties of ambient solar wind plasma. The magnetic turbulence in the solar wind, for example, can influence the timing of the first arriving particles, the timing when the particle flux crosses a pre-set threshold (e.g., Qin et al. 2005; Wang & Qin 2015), and also the event-integrated energy spectral index (e.g., Zhao et al. 2016b, 2017). Our results in Figures 2, 14 and 15 emphasize the importance and necessity of transporting energetic particles within a solar wind solution derived from self-consistent MHD simulations, where the interplay of these processes can be accurately captured and studied.

## 6. SUMMARY AND CONCLUSIONS

As SEPs can pose significant radiation hazards in space, it becomes necessary and crucial to understand their underlying physics and assess their potential impacts. Numerical modeling based on first principles can offer valuable insights into SEPs, providing synthetic observables such as the shock properties, SEP time profiles and spectra at any time and location in space. In this work, we have conducted a comprehensive investigation of the solar energetic protons during the 2013 April 11 SEP event using the numerical modeling tools within SWMF. This event, thoroughly reported by Lario et al. (2014) and summarized in Section 3, is characterized by the absence of significant SEP fluxes at STA, and a faster SEP onset at STB compared to the Earth.

Our study begins with steady-state solar wind simulations driven by the stream-aligned AWSOM-R model, with the processed GONG magnetogram, as described in Section 2.1. The simulations yield realistic solar wind backgrounds, validated against multi-point EUV observations as shown in Section 4.1. Following this, time-accurate simulations have been performed. A force-imbalanced GL flux rope, with the EEGGL-derived magnetic configurations, is then placed on top of the source AR, as stated in Section 2.2. The propagation of the CME flux rope is displayed in Section 4.2, validated through the WL image comparisons with multi-point observations from *SDO/AIA* as well as COR1 on board STA and STB.

As the CME propagates into the SC and IH domains, it further interacts with the ambient solar wind, producing fast-mode shocks where particles are accelerated effectively. A shock capturing tool has been developed to study the CME-driven shock properties starting from the low solar corona, as illustrated in Section 4.3. Utilizing the AMR technique, our shock capturing tool shows the complex shock dynamics with high spatial resolutions. Through the magnetic connectivity analysis, no magnetic connectivity has been found to the shock for STA during this event, accounting for the absence of SEPs at STA. Moreover, the time-evolving shock properties are shown in Figure 8, which

demonstrates that an earlier magnetic connectivity, along with a higher compression ratio at the onset phase, has been established for STB than the Earth during this event. Our simulation results about the shock can explain the observed differences of SEP behaviors as stated in Section 3, further underscoring the tool’s versatility and potential for simulating intricate solar events.

Within SWMF, we have implemented a newly developed high-resolution Poisson bracket scheme into M-FLAMPA to solve the kinetic equation governing energetic particle acceleration and transport processes. The scheme implementation and the setup of free parameters are thoroughly described in details in Section 2.3. New synthetic observables, including the SEP fluxes in plane cut, 2D distribution on the 1 AU sphere, intensity-time profiles, energy spectra, are presented in Section 4.4, showcasing the successful integration of the Poisson bracket scheme and also providing insights into understanding the SEP behaviors. For example, we notice the differences and similarities in comparisons of the SEP spectrum at Earth and STB. The thermal energy density of the ambient solar wind, which the quantity of injection particles is proportional to, has been inspected, offering consistent results in the observed and simulated SEP flux spectra.

Despite these advancements, challenges still remain in comparisons between simulations and observations. In Section 5.1, we have discussed the advantages of the stream-aligned MHD solutions by AWSoM-R and the mismatched results and uncertainties which may have potential impacts on SEP behaviors. In Section 5.2, we highlight the role of the flux rope initialization mechanism, the shock complexity, as well as their mutual effects on the determination of the scaling factor for SEP fluxes. Moreover, we examine the self-generated Alfvén wave turbulence and the corresponding simulated parallel MFP in Section 5.3. We find that the over estimation of particle acceleration at high energies in our model is likely attributed to the underestimation of the parallel MFP in the downstream Alfvén wave turbulence, as well as the omission of finite acceleration time. We further study the variations of the SEP intensity-time profiles and fluence spectrum with different upstream MFPs. Note that the SEP onset phase contains competing processes between the continuous acceleration of protons and the diffusion process. The discussions in Section 5.3 demonstrate the complexity of MFP studies and their implications on SEPs (e.g., Bieber et al. 1994; Lang et al. 2024). In the future, more meticulous considerations and joint efforts in both fields of study are needed for the improvements in numerical modeling for space science studies.

This study represents a meaningful advancement in SEP modeling, showcasing newly developed methods and their practical applications. The implementation of the Poisson bracket scheme within SWMF enables high-resolution simulations for SEPs, and the shock capturing tool provides insights into the evolving properties of shock surfaces. These methodological developments, combined with a variety of synthetic observables, facilitate the elucidation of the underlying physics during the 2013 April 11 SEP event, improving our understanding of SEPs and their interactions with space weather phenomena. Looking ahead, the tools and methodologies presented here hold great promise to investigate the key scientific questions (Anastasiadis et al. 2019; Pevtsov et al. 2023; Guo et al. 2024) and support operational capabilities (Vourlidis et al. 2023; Georgoulis et al. 2024; Zheng et al. 2024), ultimately enhancing our knowledge of heliophysical processes relevant to SEPs, improving radiation risk assessments, and contributing to safer space exploration in the future.

#### ACKNOWLEDGMENTS

This work is supported by the NASA Living With a Star Strategic Capability grant No. 80NSSC22K0892 (SCEPTER) and NASA Space Weather Center of Excellence program under award



No. 80NSSC23M0191 (CLEAR). The authors express their great gratitude to the *SOHO* project, an international cooperation between ESA and NASA, and to the *SDO*, *STEREO*, *ACE*, *GOES* and *PSP* teams. The authors acknowledge the development of the CDAW<sup>4</sup>, DONKI<sup>5</sup>, and OMNI<sup>7</sup> datasets. The authors also thank the Virtual Solar Observatory<sup>8</sup> (VSO) project at the National Solar Observatory (NSO), which serves as a research tool allowing scientists to search for the solar and heliospheric physics data. This work utilizes data from the NSO Integrated Synoptic Program, which is operated by the Association of Universities for Research in Astronomy, under a cooperative agreement with the National Science Foundation and with additional financial support from the National Oceanic and Atmospheric Administration, the National Aeronautics and Space Administration, and the United States Air Force. The GONG<sup>2</sup> network of instruments is hosted by the Big Bear Solar Observatory, High Altitude Observatory, Learmonth Solar Observatory (Australia), Udaipur Solar Observatory (India), Instituto de Astrofísica de Canarias (Spain), and Cerro Tololo Interamerican Observatory (Chile). Computational resources supporting this work are provided by the NASA High-End Computing (HEC) Program through the NASA Advanced Supercomputing (NAS) Division at the Ames Research Center. Any opinions, findings, and conclusions or recommendations expressed in this material are those of the author(s) and do not necessarily reflect the views of the National Aeronautics and Space Administration.

## REFERENCES

- Abraham-Shrauner, B. 1972, *Journal of Geophysical Research*, 77, 736, doi: [10.1029/JA077i004p00736](https://doi.org/10.1029/JA077i004p00736)
- Altschuler, M. D., & Newkirk, G. 1969, *SoPh*, 9, 131, doi: [10.1007/BF00145734](https://doi.org/10.1007/BF00145734)
- Anastasiadis, A., Lario, D., Papaioannou, A., Kouloumvakos, A., & Vourlidis, A. 2019, *Philosophical Transactions of the Royal Society A*, 377, 20180100, doi: [10.1098/rsta.2018.0100](https://doi.org/10.1098/rsta.2018.0100)
- Anastasiadis, A., Papaioannou, A., Sandberg, I., et al. 2017, *SoPh*, 292, 1, doi: [10.1007/s11207-017-1163-7](https://doi.org/10.1007/s11207-017-1163-7)
- Antiochos, S. K. 2013, *ApJ*, 772, 72, doi: [10.1088/0004-637X/772/1/72](https://doi.org/10.1088/0004-637X/772/1/72)
- Antiochos, S. K., DeVore, C., & Klimchuk, J. 1999, *ApJ*, 510, 485, doi: [10.1086/306563](https://doi.org/10.1086/306563)
- Aran, A., Sanahuja, B., & Lario, D. 2006, *Advances in Space Research*, 37, 1240, doi: [10.1016/j.asr.2005.09.019](https://doi.org/10.1016/j.asr.2005.09.019)
- Armstrong, T. P., Pesses, M. E., & Decker, R. B. 1985, *Collisionless Shocks in the Heliosphere: Reviews of Current Research*, 35, 271, doi: [10.1029/GM035p0271](https://doi.org/10.1029/GM035p0271)
- Aschwanden, M. J. 2012, *SSRv*, 171, 3, doi: [10.1007/s11214-011-9865-x](https://doi.org/10.1007/s11214-011-9865-x)
- Axford, W., Leer, E., & Skadron, G. 1977, in *International Cosmic Ray Conference*, Vol. 11, Springer, 132, doi: [10.1007/978-3-662-25523-0](https://doi.org/10.1007/978-3-662-25523-0)
- Bain, H. M., Copeland, K., Onsager, T. G., & Steenburgh, R. A. 2023, *Space Weather*, 21, e2022SW003346, doi: [10.1029/2022SW003346](https://doi.org/10.1029/2022SW003346)
- Bain, H. M., Mays, M. L., Luhmann, J. G., et al. 2016, *ApJ*, 825, 1, doi: [10.3847/0004-637X/825/1/1](https://doi.org/10.3847/0004-637X/825/1/1)
- Balch, C. C. 2008, *Space Weather*, 6, doi: [10.1029/2007SW000337](https://doi.org/10.1029/2007SW000337)
- Bale, S. D., Goetz, K., Harvey, P., et al. 2016, *SSRv*, 204, 49, doi: [10.1007/s11214-016-0244-5](https://doi.org/10.1007/s11214-016-0244-5)
- Band, D., Matteson, J., Ford, L., et al. 1993, *ApJ*, 413, 281, doi: [10.1086/172995](https://doi.org/10.1086/172995)
- Bandyopadhyay, R., & McComas, D. J. 2021, *ApJ*, 923, 193, doi: [10.3847/1538-4357/ac3486](https://doi.org/10.3847/1538-4357/ac3486)
- Barkhudarov, E., Mdivnishvili, M., Sokolov, I., Taktakishvili, M., & Terekhin, V. 1991, *Journal of Fluid Mechanics*, 226, 497, doi: [10.1017/S0022112091002483](https://doi.org/10.1017/S0022112091002483)
- Baydin, A. G., Poduval, B., & Schwadron, N. A. 2023, *Space Weather*, 21, e2023SW003593, doi: [10.1029/2023SW003593](https://doi.org/10.1029/2023SW003593)
- Bell, A. 1978a, *Monthly Notices of the Royal Astronomical Society*, 182, 147, doi: [10.1093/mnras/182.2.147](https://doi.org/10.1093/mnras/182.2.147)

- . 1978b, *Monthly Notices of the Royal Astronomical Society*, 182, 443, doi: [10.1093/mnras/182.3.443](https://doi.org/10.1093/mnras/182.3.443)
- Berger, M. J., & Colella, P. 1989, *Journal of Computational Physics*, 82, 64, doi: [10.1016/0021-9991\(89\)90035-1](https://doi.org/10.1016/0021-9991(89)90035-1)
- Bieber, J. W., Matthaeus, W. H., Smith, C. W., et al. 1994, *ApJ*, 420, 294, doi: [10.1086/173559](https://doi.org/10.1086/173559)
- Blandford, R., & Eichler, D. 1987, *Physics Reports*, 154, 1, doi: [10.1016/0370-1573\(87\)90134-7](https://doi.org/10.1016/0370-1573(87)90134-7)
- Blandford, R. D., & Ostriker, J. P. 1978, *ApJ*, 221, L29, doi: [10.1086/182658](https://doi.org/10.1086/182658)
- Borovikov, D., Sokolov, I., Huang, Z., Roussev, I., & Gombosi, T. 2019, arXiv preprint arXiv:1911.10165, doi: [10.48550/arXiv.1911.10165](https://doi.org/10.48550/arXiv.1911.10165)
- Borovikov, D., Sokolov, I., Roussev, I., Taktakishvili, A., & Gombosi, T. 2018, *ApJ*, 864, 88, doi: [10.3847/1538-4357/aad68d](https://doi.org/10.3847/1538-4357/aad68d)
- Borovikov, D., Sokolov, I. V., Manchester, W. B., Jin, M., & Gombosi, T. I. 2017, *Journal of Geophysical Research: Space Physics*, 122, 7979, doi: [10.1002/2017JA024304](https://doi.org/10.1002/2017JA024304)
- Borovikov, D., Sokolov, I. V., & Tóth, G. 2015, *Journal of Computational Physics*, 297, 599, doi: [10.1016/j.jcp.2015.05.038](https://doi.org/10.1016/j.jcp.2015.05.038)
- Boubrahimi, S. F., Aydin, B., Martens, P., & Angryk, R. 2017, in *2017 IEEE International Conference on Big Data (Big Data)*, IEEE, 2533–2542, doi: [10.1109/BigData.2017.8258212](https://doi.org/10.1109/BigData.2017.8258212)
- Brchnelova, M., Kuźma, B., Perri, B., Lani, A., & Poedts, S. 2022, *ApJS*, 263, 18, doi: [10.3847/1538-4365/ac8eb1](https://doi.org/10.3847/1538-4365/ac8eb1)
- Brueckner, G. E., Howard, R. A., Koomen, M. J., et al. 1995, *SoPh*, 162, 357, doi: [10.1007/BF00733434](https://doi.org/10.1007/BF00733434)
- Bruno, A. 2017, *Space Weather*, 15, 1191, doi: [10.1002/2017SW001672](https://doi.org/10.1002/2017SW001672)
- Bruno, A., & Richardson, I. G. 2021, *SoPh*, 296, 36, doi: [10.1007/s11207-021-01779-4](https://doi.org/10.1007/s11207-021-01779-4)
- Bučík, R. 2020, *SSRv*, 216, 24, doi: [10.1007/s11214-020-00650-5](https://doi.org/10.1007/s11214-020-00650-5)
- Buzulukova, N., & Tsurutani, B. 2022, *Frontiers in Astronomy and Space Sciences*, 9, 1017103, doi: [10.3389/fspas.2022.1017103](https://doi.org/10.3389/fspas.2022.1017103)
- Cane, H., Mewaldt, R., Cohen, C., & Von Roseninge, T. 2006, *Journal of Geophysical Research: Space Physics*, 111, doi: [10.1029/2005JA011071](https://doi.org/10.1029/2005JA011071)
- Chandran, B. D., Dennis, T. J., Quataert, E., & Bale, S. D. 2011, *ApJ*, 743, 197, doi: [10.1088/0004-637X/743/2/197](https://doi.org/10.1088/0004-637X/743/2/197)
- Chatterjee, S., Dayeh, M. A., Muñoz-Jaramillo, A., et al. 2024, *Space Weather*, 22, e2023SW003568, doi: [10.1029/2023SW003568](https://doi.org/10.1029/2023SW003568)
- Chen, P. 2011, *Living Reviews in Solar Physics*, 8, 1, doi: [10.12942/lrsp-2011-1](https://doi.org/10.12942/lrsp-2011-1)
- Chen, X., Giacalone, J., & Guo, F. 2022, *ApJ*, 941, 23, doi: [10.3847/1538-4357/ac9f43](https://doi.org/10.3847/1538-4357/ac9f43)
- Chen, X., Giacalone, J., Guo, F., & Klein, K. G. 2024a, *ApJ*, 965, 61, doi: [10.3847/1538-4357/ad33c3](https://doi.org/10.3847/1538-4357/ad33c3)
- Chen, Y., Manchester, W., Jin, M., & Pevtsov, A. 2024b, *Statistics and Data Science in Imaging*, 1, 2391688, doi: [10.1080/29979676.2024.2391688](https://doi.org/10.1080/29979676.2024.2391688)
- Cheng, L., Zhang, M., Kwon, R., & Lario, D. 2024, arXiv preprint arXiv:2411.04095, doi: [10.48550/arXiv.2411.04095](https://doi.org/10.48550/arXiv.2411.04095)
- Chhiber, R., Ruffolo, D., Matthaeus, W. H., et al. 2021, *ApJ*, 908, 174, doi: [10.3847/1538-4357/abd7f0](https://doi.org/10.3847/1538-4357/abd7f0)
- Cliver, E. W., Schrijver, C. J., Shibata, K., & Usoskin, I. G. 2022, *Living Reviews in Solar Physics*, 19, 2, doi: [10.1007/s41116-022-00033-8](https://doi.org/10.1007/s41116-022-00033-8)
- Cohen, C., Mason, G., Mewaldt, R., & Wiedenbeck, M. 2014, *ApJ*, 793, 35, doi: [10.1088/0004-637X/793/1/35](https://doi.org/10.1088/0004-637X/793/1/35)
- Cohen, C., Stone, E., Mewaldt, R., et al. 2005, *Journal of Geophysical Research: Space Physics*, 110, doi: [10.1029/2005JA011004](https://doi.org/10.1029/2005JA011004)
- Dahlin, J. T., DeVore, C. R., & Antiochos, S. K. 2022, *ApJ*, 941, 79, doi: [10.3847/1538-4357/ac9e5a](https://doi.org/10.3847/1538-4357/ac9e5a)
- de Wit, T. D., Krasnoselskikh, V. V., Bale, S. D., et al. 2020, *ApJS*, 246, 39, doi: [10.3847/1538-4365/ab5853](https://doi.org/10.3847/1538-4365/ab5853)
- Delaunay, B. 1934, *Bull. Acad. Science USSR VII: Class. Sci. Mat. Nat.*, 793. <https://www.mathnet.ru/links/95d7c8aa6111426eaf4114db10ced544/im4937.pdf>
- Desai, M., & Giacalone, J. 2016, *Living Reviews in Solar Physics*, 13, 3, doi: [10.1007/s41116-016-0002-5](https://doi.org/10.1007/s41116-016-0002-5)
- Dierckxsens, M., Tziotziou, K., Dalla, S., et al. 2015, *SoPh*, 290, 841, doi: [10.1007/s11207-014-0641-4](https://doi.org/10.1007/s11207-014-0641-4)

- Ding, L.-G., Li, G., Le, G.-M., Gu, B., & Cao, X.-X. 2015, *ApJ*, 812, 171, doi: [10.1088/0004-637X/812/2/171](https://doi.org/10.1088/0004-637X/812/2/171)
- Ding, Z., Wijzen, N., Li, G., & Poedts, S. 2022, *A&A*, 668, A71, doi: [10.1051/0004-6361/202244732](https://doi.org/10.1051/0004-6361/202244732)
- Domingo, V., Fleck, B., & Poland, A. I. 1995, *SoPh*, 162, 1, doi: [10.1007/BF00733425](https://doi.org/10.1007/BF00733425)
- Downs, C., Roussev, I. I., van der Holst, B., et al. 2010, *ApJ*, 712, 1219, doi: [10.1088/0004-637X/712/2/1219](https://doi.org/10.1088/0004-637X/712/2/1219)
- Downs, C., Warmuth, A., Long, D. M., et al. 2021, *ApJ*, 911, 118, doi: [10.3847/1538-4357/abea78](https://doi.org/10.3847/1538-4357/abea78)
- Dröge, W., Kartavykh, Y., Klecker, B., & Kovaltsov, G. 2010, *ApJ*, 709, 912, doi: [10.1088/0004-637X/709/2/912](https://doi.org/10.1088/0004-637X/709/2/912)
- Drury, L. O. 1983, *Reports on Progress in Physics*, 46, 973, doi: [10.1088/0034-4885/46/8/002](https://doi.org/10.1088/0034-4885/46/8/002)
- Earl, J. A. 1974, *ApJ*, 193, 231, doi: [10.1086/153152](https://doi.org/10.1086/153152)
- Ellison, D. C., Baring, M. G., & Jones, F. C. 1995, *ApJ*, 453, 873, doi: [10.1086/176447](https://doi.org/10.1086/176447)
- Ellison, D. C., Jones, F. C., & Reynolds, S. P. 1990, *ApJ*, 360, 702, doi: [10.1086/169156](https://doi.org/10.1086/169156)
- Ellison, D. C., & Ramaty, R. 1985, *ApJ*, 298, 400, doi: [10.1086/163623](https://doi.org/10.1086/163623)
- Engelbrecht, N. E. 2019, *ApJ*, 880, 60, doi: [10.3847/1538-4357/ab2871](https://doi.org/10.3847/1538-4357/ab2871)
- Erdős, G., & Balogh, A. 2005, *Advances in Space Research*, 35, 625, doi: [10.1016/j.asr.2005.02.048](https://doi.org/10.1016/j.asr.2005.02.048)
- Falconer, D., Barghouty, A. F., Khazanov, I., & Moore, R. 2011, *Space Weather*, 9, doi: [10.1029/2009SW000537](https://doi.org/10.1029/2009SW000537)
- Falconer, D. A., Moore, R. L., Barghouty, A. F., & Khazanov, I. 2014, *Space Weather*, 12, 306, doi: [10.1002/2013SW001024](https://doi.org/10.1002/2013SW001024)
- Fermi, E. 1949, *Physical Review*, 75, 1169, doi: [10.1103/PhysRev.75.1169](https://doi.org/10.1103/PhysRev.75.1169)
- Fisk, L., & Gloeckler, G. 2006, *ApJ*, 640, L79, doi: [10.1086/503293](https://doi.org/10.1086/503293)
- . 2008, *ApJ*, 686, 1466, doi: [10.1086/591543](https://doi.org/10.1086/591543)
- Fisk, L., & Schwadron, N. 2001, *ApJ*, 560, 425, doi: [10.1086/322503](https://doi.org/10.1086/322503)
- Fogtman, A., Baatout, S., Baselet, B., et al. 2023, *npj Microgravity*, 9, 8, doi: [10.1038/s41526-023-00262-7](https://doi.org/10.1038/s41526-023-00262-7)
- Fox, N., Velli, M., Bale, S., et al. 2016, *SSRv*, 204, 7, doi: [10.1007/s11214-015-0211-6](https://doi.org/10.1007/s11214-015-0211-6)
- Fulara, A., Chandra, R., Chen, P., et al. 2019, *SoPh*, 294, 1, doi: [10.1007/s11207-019-1445-3](https://doi.org/10.1007/s11207-019-1445-3)
- Georgoulis, M. K., Yardley, S. L., Guerra, J. A., et al. 2024, *Advances in Space Research*, doi: [10.1016/j.asr.2024.02.030](https://doi.org/10.1016/j.asr.2024.02.030)
- Giacalone, J. 2005a, *ApJ*, 628, L37, doi: [10.1086/432510](https://doi.org/10.1086/432510)
- . 2005b, *ApJ*, 624, 765, doi: [10.1086/429265](https://doi.org/10.1086/429265)
- Giacalone, J., Jokipii, J., & Mazur, J. 2000, *ApJ*, 532, L75, doi: [10.1086/312564](https://doi.org/10.1086/312564)
- Giacalone, J., & Kóta, J. 2007, *Solar Dynamics and Its Effects on the Heliosphere and Earth*, 277, doi: [10.1007/978-0-387-69532-7\\_19](https://doi.org/10.1007/978-0-387-69532-7_19)
- Giacalone, J., & Neugebauer, M. 2008, *ApJ*, 673, 629, doi: [10.1086/524008](https://doi.org/10.1086/524008)
- Giacalone, J., Mitchell, D., Allen, R., et al. 2020, *ApJS*, 246, 29, doi: [10.3847/1538-4365/ab5221](https://doi.org/10.3847/1538-4365/ab5221)
- Gibson, S. E., & Low, B. 1998, *ApJ*, 493, 460, doi: [10.1086/305107](https://doi.org/10.1086/305107)
- Gieseler, J., Dresing, N., Palmroos, C., et al. 2023, *Frontiers in Astronomy and Space Sciences*, 9, 1058810, doi: [10.3389/fspas.2022.1058810](https://doi.org/10.3389/fspas.2022.1058810)
- Gloeckler, G. 2003, *AIP Conference Proceedings*, 679, 583, doi: [10.1063/1.1618663](https://doi.org/10.1063/1.1618663)
- Gold, R. E., Krimigis, S. M., Hawkins, S. E., I., et al. 1998, *SSRv*, 86, 541, doi: [10.1023/A:1005088115759](https://doi.org/10.1023/A:1005088115759)
- Gombosi, T. I. 1998, *Physics of the Space Environment* (Cambridge University Press), 274–277, doi: [10.1017/CBO9780511529474](https://doi.org/10.1017/CBO9780511529474)
- Gombosi, T. I., De Zeeuw, D. L., Powell, K. G., et al. 2003, *Space Plasma Simulation*, 247, doi: [10.1007/3-540-36530-3\\_12](https://doi.org/10.1007/3-540-36530-3_12)
- Gombosi, T. I., van der Holst, B., Manchester, W. B., & Sokolov, I. V. 2018, *Living Reviews in Solar Physics*, 15, 1, doi: [10.1007/s41116-018-0014-4](https://doi.org/10.1007/s41116-018-0014-4)
- Gombosi, T. I., Powell, K. G., De Zeeuw, D. L., et al. 2004, *Computing in Science & Engineering*, 6, 14, doi: [10.1109/MCISE.2004.1267603](https://doi.org/10.1109/MCISE.2004.1267603)
- Gombosi, T. I., Chen, Y., Glocer, A., et al. 2021, *Journal of Space Weather and Space Climate*, 11, 42, doi: [10.1051/swsc/2021020](https://doi.org/10.1051/swsc/2021020)
- Gopalswamy, N., Mäkelä, P., Yashiro, S., et al. 2015, *Journal of Physics: Conference Series*, 642, 012012, doi: [10.1088/1742-6596/642/1/012012](https://doi.org/10.1088/1742-6596/642/1/012012)
- Gopalswamy, N., Yashiro, S., Michalek, G., et al. 2002, *ApJ*, 572, L103, doi: [10.1086/341601](https://doi.org/10.1086/341601)
- Gopalswamy, N., Yashiro, S., Michalek, G., et al. 2009, *Earth, Moon, and Planets*, 104, 295, doi: [10.1007/s11038-008-9282-7](https://doi.org/10.1007/s11038-008-9282-7)

- Gosling, J., & McComas, D. 1987, *Geophys. Res. Lett.*, 14, 355, doi: [10.1029/GL014i004p00355](https://doi.org/10.1029/GL014i004p00355)
- Guo, J., Zeitlin, C., Wimmer-Schweingruber, R. F., et al. 2021, *A&A Rv*, 29, 1, doi: [10.1007/s00159-021-00136-5](https://doi.org/10.1007/s00159-021-00136-5)
- Guo, J., Wang, B., Whitman, K., et al. 2024, *Advances in Space Research*, doi: [10.1016/j.asr.2024.03.070](https://doi.org/10.1016/j.asr.2024.03.070)
- Harvey, J., Hill, F., Hubbard, R., et al. 1996, *Science*, 272, 1284, doi: [10.1126/science.272.5266.1284](https://doi.org/10.1126/science.272.5266.1284)
- Hayes, A., Vourlidas, A., & Howard, R. 2001, *ApJ*, 548, 1081, doi: [10.1086/319029](https://doi.org/10.1086/319029)
- Hill, F. 2018, *Space Weather*, 16, 1488, doi: [10.1029/2018SW002001](https://doi.org/10.1029/2018SW002001)
- Hinterreiter, J., Magdalenic, J., Temmer, M., et al. 2019, *SoPh*, 294, 1, doi: [10.1007/s11207-019-1558-8](https://doi.org/10.1007/s11207-019-1558-8)
- Hoppock, I. W., Chandran, B. D., Klein, K. G., Mallet, A., & Verscharen, D. 2018, *Journal of Plasma Physics*, 84, 905840615, doi: [10.1017/S0022377818001277](https://doi.org/10.1017/S0022377818001277)
- Hosseinzadeh, P., Boubrahimi, S. F., & Hamdi, S. M. 2024, *ApJS*, 270, 31, doi: [10.3847/1538-4365/ad1de0](https://doi.org/10.3847/1538-4365/ad1de0)
- Howard, R. A., Moses, J., Vourlidas, A., et al. 2008, *SSRv*, 136, 67, doi: [10.1007/s11214-008-9341-4](https://doi.org/10.1007/s11214-008-9341-4)
- Hu, J., Li, G., Ao, X., Zank, G. P., & Verkhoglyadova, O. 2017, *Journal of Geophysical Research: Space Physics*, 122, 10, doi: [10.1002/2017JA024077](https://doi.org/10.1002/2017JA024077)
- Huang, Z., Tóth, G., Huang, J., et al. 2024a, *ApJL*, 965, L1, doi: [10.3847/2041-8213/ad3547](https://doi.org/10.3847/2041-8213/ad3547)
- Huang, Z., Tóth, G., Sachdeva, N., & van der Holst, B. 2024b, *ApJ*, 965, 1, doi: [10.3847/1538-4357/ad32ca](https://doi.org/10.3847/1538-4357/ad32ca)
- Huang, Z., Tóth, G., Sachdeva, N., et al. 2023, *ApJL*, 946, L47, doi: [10.3847/2041-8213/acc5ef](https://doi.org/10.3847/2041-8213/acc5ef)
- Hugoniot, H. 1889a, *Journal de l'École Polytechnique (French)*, 57, 1. <https://books.google.com/books?id=wccAAAAAYAAJ>
- . 1889b, *Journal de l'École Polytechnique (French)*, 58, 1. <https://gallica.bnf.fr/ark:/12148/bpt6k4337130/f11.item>
- Isenberg, P. A. 1997, *Journal of Geophysical Research: Space Physics*, 102, 4719, doi: [10.1029/96JA03671](https://doi.org/10.1029/96JA03671)
- Jian, L., MacNeice, P., Taktakishvili, A., et al. 2015, *Space Weather*, 13, 316, doi: [10.1002/2015SW001174](https://doi.org/10.1002/2015SW001174)
- Jin, M., Manchester, W., van der Holst, B., et al. 2017a, *ApJ*, 834, 172, doi: [10.3847/1538-4357/834/2/172](https://doi.org/10.3847/1538-4357/834/2/172)
- Jin, M., Nitta, N. V., & Cohen, C. M. 2022, *Space Weather*, 20, e2021SW002894, doi: [10.1029/2021SW002894](https://doi.org/10.1029/2021SW002894)
- Jin, M., Schrijver, C., Cheung, M., et al. 2016, *ApJ*, 820, 16, doi: [10.3847/0004-637X/820/1/16](https://doi.org/10.3847/0004-637X/820/1/16)
- Jin, M., Manchester, W., Van Der Holst, B., et al. 2013, *ApJ*, 773, 50, doi: [10.1088/0004-637X/773/1/50](https://doi.org/10.1088/0004-637X/773/1/50)
- Jin, M., Manchester, W., van der Holst, B., et al. 2017b, *ApJ*, 834, 173, doi: [10.3847/1538-4357/834/2/173](https://doi.org/10.3847/1538-4357/834/2/173)
- Jin, M., Li, G., Nitta, N., et al. 2024, *arXiv preprint arXiv:2409.18020*, doi: [10.48550/arXiv.2409.18020](https://doi.org/10.48550/arXiv.2409.18020)
- Jivani, A., Sachdeva, N., Huang, Z., et al. 2023, *Space Weather*, 21, e2022SW003262, doi: [10.1029/2022SW003262](https://doi.org/10.1029/2022SW003262)
- Jokipii, J. 1982, *ApJ*, 255, 716, doi: [10.1086/159870](https://doi.org/10.1086/159870)
- . 1987, *ApJ*, 313, 842, doi: [10.1086/165022](https://doi.org/10.1086/165022)
- Jokipii, J. R. 1966, *ApJ*, 146, 480, doi: [10.1086/148912](https://doi.org/10.1086/148912)
- Jones, F. C., & Ellison, D. C. 1991, *SSRv*, 58, 259, doi: [10.1007/BF01206003](https://doi.org/10.1007/BF01206003)
- Jones, J. B. L., Bentley, R., Hunter, R., et al. 2005, *Advances in Space Research*, 36, 2258, doi: [10.1016/j.asr.2004.04.017](https://doi.org/10.1016/j.asr.2004.04.017)
- Joshi, B., Kushwaha, U., Veronig, A. M., et al. 2016, *ApJ*, 834, 42, doi: [10.3847/1538-4357/834/1/42](https://doi.org/10.3847/1538-4357/834/1/42)
- Jun, I., Garrett, H., Kim, W., et al. 2024, *Advances in Space Research*, doi: [10.1016/j.asr.2024.03.079](https://doi.org/10.1016/j.asr.2024.03.079)
- Kahler, S., Hildner, E., & Van Hollebeke, M. 1978, *SoPh*, 57, 429, doi: [10.1007/BF00160116](https://doi.org/10.1007/BF00160116)
- Kahler, S., & Ling, A. 2019, *ApJ*, 872, 89, doi: [10.3847/1538-4357/aafb03](https://doi.org/10.3847/1538-4357/aafb03)
- Kahler, S., Sheeley Jr, N., Howard, R., et al. 1984, *Journal of Geophysical Research: Space Physics*, 89, 9683, doi: [10.1029/JA089iA11p09683](https://doi.org/10.1029/JA089iA11p09683)
- Kaiser, M. L., Kucera, T., Davila, J., et al. 2008, *SSRv*, 136, 5, doi: [10.1007/s11214-007-9277-0](https://doi.org/10.1007/s11214-007-9277-0)

- Kasapis, S., Kitiashvili, I. N., Kosovitch, P., et al. 2024, *ApJ*, 974, 131, doi: [10.3847/1538-4357/ad6f0e](https://doi.org/10.3847/1538-4357/ad6f0e)
- Kasapis, S., Zhao, L., Chen, Y., et al. 2022, *Space Weather*, 20, e2021SW002842, doi: [10.1029/2021SW002842](https://doi.org/10.1029/2021SW002842)
- Kasper, J. C., Abiad, R., Austin, G., et al. 2016, *SSRv*, 204, 131, doi: [10.1007/s11214-015-0206-3](https://doi.org/10.1007/s11214-015-0206-3)
- Kataoka, R., Ebisuzaki, T., Kusano, K., et al. 2009, *Journal of Geophysical Research: Space Physics*, 114, doi: [10.1029/2009JA014167](https://doi.org/10.1029/2009JA014167)
- Kecskeméty, K., Daibog, E., Logachev, Y. I., & Kóta, J. 2009, *Journal of Geophysical Research: Space Physics*, 114, doi: [10.1029/2008JA013730](https://doi.org/10.1029/2008JA013730)
- Kilpua, E., Koskinen, H. E., & Pulkkinen, T. I. 2017, *Living Reviews in Solar Physics*, 14, 1, doi: [10.1007/s41116-017-0009-6](https://doi.org/10.1007/s41116-017-0009-6)
- Kilpua, E. K., Lugaz, N., Mays, M. L., & Temmer, M. 2019, *Space Weather*, 17, 498, doi: [10.1029/2018SW001944](https://doi.org/10.1029/2018SW001944)
- King, J., & Papitashvili, N. 2005, *Journal of Geophysical Research: Space Physics*, 110, doi: [10.1029/2004JA010649](https://doi.org/10.1029/2004JA010649)
- Klein, K.-L., & Dalla, S. 2017, *SSRv*, 212, 1107, doi: [10.1007/s11214-017-0382-4](https://doi.org/10.1007/s11214-017-0382-4)
- Kolmogorov, A. 1941, *Akademiia Nauk SSSR Doklady*, 30, 301, doi: [10.1098/rspa.1991.0075](https://doi.org/10.1098/rspa.1991.0075)
- Kong, X., Guo, F., Chen, Y., & Giacalone, J. 2019, *ApJ*, 883, 49, doi: [10.3847/1538-4357/ab3848](https://doi.org/10.3847/1538-4357/ab3848)
- Kóta, J. 1997, in *Proceedings of the 25th International Cosmic Ray Conference*, Vol. 1, 213–216. <https://articles.adsabs.harvard.edu/pdf/1997ICRC...25a.213K>
- Kóta, J., & Jokipii, J. 2004, *AIP Conference Proceedings*, 719, 272, doi: [10.1063/1.1809528](https://doi.org/10.1063/1.1809528)
- Kóta, J., Manchester, W., Jokipii, J., De Zeeuw, D., & Gombosi, T. 2005, *AIP Conference Proceedings*, 781, 201, doi: [10.1063/1.2032697](https://doi.org/10.1063/1.2032697)
- Kouloumvakos, A., Rouillard, A. P., Wu, Y., et al. 2019, *ApJ*, 876, 80, doi: [10.3847/1538-4357/ab15d7](https://doi.org/10.3847/1538-4357/ab15d7)
- Kouloumvakos, A., Kwon, R., Rodríguez-García, L., et al. 2022, *A&A*, 660, A84, doi: [10.1051/0004-6361/202142515](https://doi.org/10.1051/0004-6361/202142515)
- Krivodonova, L., & Smirnov, A. 2021, *arXiv preprint arXiv:2110.00067*, doi: [10.48550/arXiv.2110.00067](https://doi.org/10.48550/arXiv.2110.00067)
- Krymskii, G. 1977, in *Akademiia Nauk SSSR Doklady*, Vol. 234, 1306–1308
- Kühl, P., & Heber, B. 2019, *Space Weather*, 17, 84, doi: [10.1029/2018SW002114](https://doi.org/10.1029/2018SW002114)
- Kwon, R.-Y., & Vourlidas, A. 2017, *ApJ*, 836, 246, doi: [10.3847/1538-4357/aa5b92](https://doi.org/10.3847/1538-4357/aa5b92)
- Kwon, R.-Y., Zhang, J., & Olmedo, O. 2014, *ApJ*, 794, 148, doi: [10.1088/0004-637X/794/2/148](https://doi.org/10.1088/0004-637X/794/2/148)
- Laitinen, T., Dalla, S., & Marsh, M. 2013, *ApJL*, 773, L29, doi: [10.1088/2041-8205/773/2/L29](https://doi.org/10.1088/2041-8205/773/2/L29)
- Laitinen, T., Effenberger, F., Kopp, A., & Dalla, S. 2018, *Journal of Space Weather and Space Climate*, 8, A13, doi: [10.1051/swsc/2018001](https://doi.org/10.1051/swsc/2018001)
- Laitinen, T., Kopp, A., Effenberger, F., Dalla, S., & Marsh, M. 2016, *A&A*, 591, A18, doi: [10.1051/0004-6361/201527801](https://doi.org/10.1051/0004-6361/201527801)
- Landau, L. D., & Lifshitz, E. M. 1987, *Fluid Mechanics*, Vol. 6 (Elsevier)
- Lang, J., Strauss, R., Engelbrecht, N., et al. 2024, *arXiv preprint arXiv:2406.05765*, doi: [10.48550/arXiv.2406.05765](https://doi.org/10.48550/arXiv.2406.05765)
- Lario, D., Aran, A., Gómez-Herrero, R., et al. 2013, *ApJ*, 767, 41, doi: [10.1088/0004-637X/767/1/41](https://doi.org/10.1088/0004-637X/767/1/41)
- Lario, D., Berger, L., Decker, R., et al. 2019, *AJ*, 158, 12, doi: [10.3847/1538-3881/ab1e49](https://doi.org/10.3847/1538-3881/ab1e49)
- Lario, D., Kallenrode, M.-B., Decker, R., et al. 2006, *ApJ*, 653, 1531, doi: [10.1086/508982](https://doi.org/10.1086/508982)
- Lario, D., Kwon, R.-Y., Riley, P., & Raouafi, N. 2017a, *ApJ*, 847, 103, doi: [10.3847/1538-4357/aa89e3](https://doi.org/10.3847/1538-4357/aa89e3)
- Lario, D., Raouafi, N., Kwon, R.-Y., et al. 2014, *ApJ*, 797, 8, doi: [10.1088/0004-637X/797/1/8](https://doi.org/10.1088/0004-637X/797/1/8)
- Lario, D., Sanahuja, B., & Heras, A. 1998, *ApJ*, 509, 415, doi: [10.1086/306461](https://doi.org/10.1086/306461)
- Lario, D., Kwon, R.-Y., Vourlidas, A., et al. 2016, *ApJ*, 819, 72, doi: [10.3847/0004-637X/819/1/72](https://doi.org/10.3847/0004-637X/819/1/72)
- Lario, D., Kwon, R.-Y., Richardson, I. G., et al. 2017b, *ApJ*, 838, 51, doi: [10.3847/1538-4357/aa63e4](https://doi.org/10.3847/1538-4357/aa63e4)
- Lario, D., Kwon, R., Balmaceda, L., et al. 2020, *ApJ*, 889, 92, doi: [10.3847/1538-4357/ab64e1](https://doi.org/10.3847/1538-4357/ab64e1)
- Laurenza, M., Cliver, E., Hewitt, J., et al. 2009, *Space Weather*, 7, doi: [10.1029/2007SW000379](https://doi.org/10.1029/2007SW000379)
- Lavasa, E., Giannopoulos, G., Papaioannou, A., et al. 2021, *SoPh*, 296, 107, doi: [10.1007/s11207-021-01837-x](https://doi.org/10.1007/s11207-021-01837-x)
- Lee, C., Luhmann, J., Hoeksema, J., et al. 2011, *SoPh*, 269, 367, doi: [10.1007/s11207-010-9699-9](https://doi.org/10.1007/s11207-010-9699-9)
- Lee, D.-T., & Schachter, B. J. 1980, *International Journal of Computer & Information Sciences*, 9, 219, doi: [10.1007/BF00977785](https://doi.org/10.1007/BF00977785)

- Lee, M. A. 1982, *Journal of Geophysical Research: Space Physics*, 87, 5063, doi: [10.1029/JA087iA07p05063](https://doi.org/10.1029/JA087iA07p05063)
- . 1983, *Journal of Geophysical Research: Space Physics*, 88, 6109, doi: [10.1029/JA088iA08p06109](https://doi.org/10.1029/JA088iA08p06109)
- Lee, M. A., Mewaldt, R., & Giacalone, J. 2012, *SSRv*, 173, 247, doi: [10.1007/s11214-012-9932-y](https://doi.org/10.1007/s11214-012-9932-y)
- Lemen, J. R., Title, A. M., Akin, D. J., et al. 2012, *SoPh*, 275, 17, doi: [10.1007/s11207-011-9776-8](https://doi.org/10.1007/s11207-011-9776-8)
- Lepping, R., & Argentiero, P. 1971, *Journal of Geophysical Research*, 76, 4349, doi: [10.1029/JA076i019p04349](https://doi.org/10.1029/JA076i019p04349)
- Li, G., Moore, R., Mewaldt, R., Zhao, L., & Labrador, A. 2012, *SSRv*, 171, 141, doi: [10.1007/s11214-011-9823-7](https://doi.org/10.1007/s11214-011-9823-7)
- Li, G., & Zank, G. 2005, *Geophys. Res. Lett.*, 32, doi: [10.1029/2004GL021250](https://doi.org/10.1029/2004GL021250)
- Li, G., Zank, G., & Rice, W. 2003, *Journal of Geophysical Research: Space Physics*, 108, doi: [10.1029/2002JA009666](https://doi.org/10.1029/2002JA009666)
- Li, G., Zank, G., Verkhoglyadova, O., et al. 2009, *ApJ*, 702, 998, doi: [10.1088/0004-637X/702/2/998](https://doi.org/10.1088/0004-637X/702/2/998)
- Li, G., Jin, M., Ding, Z., et al. 2021, *ApJ*, 919, 146, doi: [10.3847/1538-4357/ac0db9](https://doi.org/10.3847/1538-4357/ac0db9)
- Lin, R., Anderson, K., Ashford, S., et al. 1995, *SSRv*, 71, 125, doi: [10.1007/BF00751328](https://doi.org/10.1007/BF00751328)
- Linker, J. A., Caplan, R. M., Schwadron, N., et al. 2019, *Journal of Physics: Conference Series*, 1225, 012007, doi: [10.1088/1742-6596/1225/1/012007](https://doi.org/10.1088/1742-6596/1225/1/012007)
- Liou, K., & Wu, C.-C. 2024, *ApJ*, 966, 16, doi: [10.3847/1538-4357/ad33c2](https://doi.org/10.3847/1538-4357/ad33c2)
- Liouville, J. 1838, *Journal de mathématiques pures et appliquées*, 3, 342. [http://www.numdam.org/item/JMPA\\_1838\\_1\\_3\\_342\\_0.pdf](http://www.numdam.org/item/JMPA_1838_1_3_342_0.pdf)
- Lugaz, N., Farrugia, C. J., Manchester IV, W. B., & Schwadron, N. 2013, *ApJ*, 778, 20, doi: [10.1088/0004-637X/778/1/20](https://doi.org/10.1088/0004-637X/778/1/20)
- Lugaz, N., Manchester IV, W. B., & Gombosi, T. I. 2005a, *ApJ*, 627, 1019, doi: [10.1086/430465](https://doi.org/10.1086/430465)
- . 2005b, *ApJ*, 634, 651, doi: [10.1086/491782](https://doi.org/10.1086/491782)
- Lugaz, N., Manchester IV, W. B., Roussev, I. I., Tóth, G., & Gombosi, T. I. 2007, *ApJ*, 659, 788, doi: [10.1086/512005](https://doi.org/10.1086/512005)
- Lugaz, N., Lee, C. O., Al-Haddad, N., et al. 2024, *SSRv*, 220, 73, doi: [10.1007/s11214-024-01108-8](https://doi.org/10.1007/s11214-024-01108-8)
- Luhmann, J., Ledvina, S., Krauss-Varban, D., Odstrcil, D., & Riley, P. 2007, *Advances in Space Research*, 40, 295, doi: [10.1016/j.asr.2007.03.089](https://doi.org/10.1016/j.asr.2007.03.089)
- Luhmann, J. G., Gopalswamy, N., Jian, L., & Lugaz, N. 2020, *SoPh*, 295, 61, doi: [10.1007/s11207-020-01624-0](https://doi.org/10.1007/s11207-020-01624-0)
- MacNamara, S., & Strang, G. 2016, *Splitting Methods in Communication, Imaging, Science, and Engineering*, 95, doi: [10.1007/978-3-319-41589-5\\_3](https://doi.org/10.1007/978-3-319-41589-5_3)
- Manchester, W., Kilpua, E. K., Liu, Y. D., et al. 2017, *SSRv*, 212, 1159, doi: [10.1007/s11214-017-0394-0](https://doi.org/10.1007/s11214-017-0394-0)
- Manchester IV, W., Gombosi, T., DeZeeuw, D., & Fan, Y. 2004a, *ApJ*, 610, 588, doi: [10.1086/421516](https://doi.org/10.1086/421516)
- Manchester IV, W., Kozyra, J., Lepri, S., & Lavraud, B. 2014a, *Journal of Geophysical Research: Space Physics*, 119, 5449, doi: [10.1002/2014JA019882](https://doi.org/10.1002/2014JA019882)
- Manchester IV, W., Ridley, A., Gombosi, T., & DeZeeuw, D. 2006, *Advances in Space Research*, 38, 253, doi: [10.1016/j.asr.2005.09.044](https://doi.org/10.1016/j.asr.2005.09.044)
- Manchester IV, W., van der Holst, B., & Lavraud, B. 2014b, *Plasma Physics and Controlled Fusion*, 56, 064006, doi: [10.1088/0741-3335/56/6/064006](https://doi.org/10.1088/0741-3335/56/6/064006)
- Manchester IV, W., Gombosi, T., De Zeeuw, D., et al. 2005, *ApJ*, 622, 1225, doi: [10.1086/427768](https://doi.org/10.1086/427768)
- Manchester IV, W. B., Gombosi, T. I., Roussev, I., et al. 2004b, *Journal of Geophysical Research: Space Physics*, 109, doi: [10.1029/2002JA009672](https://doi.org/10.1029/2002JA009672)
- . 2004c, *Journal of Geophysical Research: Space Physics*, 109, doi: [10.1029/2003JA010150](https://doi.org/10.1029/2003JA010150)
- Manchester IV, W. B., Vourlidas, A., Tóth, G., et al. 2008, *ApJ*, 684, 1448, doi: [10.1086/590231](https://doi.org/10.1086/590231)
- Mason, G. 2007, *SSRv*, 130, 231, doi: [10.1007/s11214-007-9156-8](https://doi.org/10.1007/s11214-007-9156-8)
- Matthaeus, W. H., Qin, G., Bieber, J. W., & Zank, G. P. 2003, *ApJ*, 590, doi: [10.1086/376613](https://doi.org/10.1086/376613)
- Melrose, D., & Pope, M. 1993, *PASA*, 10, 222, doi: [10.1017/S1323358000025716](https://doi.org/10.1017/S1323358000025716)
- Meng, X., Van der Holst, B., Tóth, G., & Gombosi, T. 2015, *Monthly Notices of the Royal Astronomical Society*, 454, 3697, doi: [10.1093/mnras/stv2249](https://doi.org/10.1093/mnras/stv2249)

- Menzel, W. P., & Purdom, J. F. 1994, *Bulletin of the American Meteorological Society*, 75, 757, doi: [10.1175/1520-0477\(1994\)075<0757:IGITFO>2.0.CO;2](https://doi.org/10.1175/1520-0477(1994)075<0757:IGITFO>2.0.CO;2)
- Mewaldt, R. 2006, *SSRv*, 124, 303, doi: [10.1007/s11214-006-9091-0](https://doi.org/10.1007/s11214-006-9091-0)
- Mewaldt, R., Cohen, C., Labrador, A., et al. 2005, *Journal of Geophysical Research: Space Physics*, 110, doi: [10.1029/2005JA011038](https://doi.org/10.1029/2005JA011038)
- Mewaldt, R. A., Cohen, C., Cook, W., et al. 2008, *SSRv*, 136, 285, doi: [10.1007/s11214-007-9288-x](https://doi.org/10.1007/s11214-007-9288-x)
- Mikić, Z., & Lee, M. 2006, *SSRv*, 123, 57, doi: [10.1007/s11214-006-9012-2](https://doi.org/10.1007/s11214-006-9012-2)
- Miroshnichenko, L. I. 2018, *Journal of Space Weather and Space Climate*, 8, A52, doi: [10.1051/swsc/2018042](https://doi.org/10.1051/swsc/2018042)
- Miteva, R., Samwel, S., & Costa-Duarte, M. 2018, *Journal of Atmospheric and Solar-Terrestrial Physics*, 180, 26, doi: [10.1016/j.jastp.2017.05.003](https://doi.org/10.1016/j.jastp.2017.05.003)
- Miteva, R., Samwel, S. W., Zabunov, S., & Dechev, M. 2020, *Bulgarian Astronomical Journal*, 33, 99
- Moradi, A., & Giacalone, J. 2022, *ApJ*, 932, 73, doi: [10.3847/1538-4357/ac66e0](https://doi.org/10.3847/1538-4357/ac66e0)
- Morgan, H., Habbal, S. R., & Woo, R. 2006, *SoPh*, 236, 263, doi: [10.1007/s11207-006-0113-6](https://doi.org/10.1007/s11207-006-0113-6)
- Müller-Mellin, R., Böttcher, S., Falenski, J., et al. 2008, *SSRv*, 136, 363, doi: [10.1007/s11214-007-9204-4](https://doi.org/10.1007/s11214-007-9204-4)
- Ng, C., & Reames, D. 1994, *ApJ*, 424, 1032, doi: [10.1086/173954](https://doi.org/10.1086/173954)
- Ng, C., Reames, D., & Tylka, A. 2003, *ApJ*, 591, 461, doi: [10.1086/375293](https://doi.org/10.1086/375293)
- Ng, C. K., Reames, D. V., & Tylka, A. J. 1999, *Geophys. Res. Lett.*, 26, 2145, doi: [10.1029/1999GL900459](https://doi.org/10.1029/1999GL900459)
- Niemela, A., Wijesen, N., Aran, A., et al. 2023, *A&A*, 679, A93, doi: [10.1051/0004-6361/202347116](https://doi.org/10.1051/0004-6361/202347116)
- Nikolić, L. 2019, *Space Weather*, 17, 1293, doi: [10.1029/2019SW002205](https://doi.org/10.1029/2019SW002205)
- Nitta, N. V., Reames, D. V., DeRosa, M. L., et al. 2006, *ApJ*, 650, 438, doi: [10.1086/507442](https://doi.org/10.1086/507442)
- Northrop, T. G. 1963, *Reviews of Geophysics and Space Physics*, 1, 283, doi: [10.1029/RG001i003p00283](https://doi.org/10.1029/RG001i003p00283)
- Núñez, M. 2011, *Space Weather*, 9, doi: [10.1029/2010SW000640](https://doi.org/10.1029/2010SW000640)
- Onsager, T., Grubb, R., Kunches, J., et al. 1996, in *GOES-8 and Beyond*, Vol. 2812, SPIE, 281–290, doi: [10.1117/12.254075](https://doi.org/10.1117/12.254075)
- Oran, R., van der Holst, B., Landi, E., et al. 2013, *ApJ*, 778, 176, doi: [10.1088/0004-637X/778/2/176](https://doi.org/10.1088/0004-637X/778/2/176)
- Paassilta, M., Papaioannou, A., Dresing, N., et al. 2018, *SoPh*, 293, 1, doi: [10.1007/s11207-018-1284-7](https://doi.org/10.1007/s11207-018-1284-7)
- Palmerio, E., Kilpua, E. K., Möstl, C., et al. 2018, *Space Weather*, 16, 442, doi: [10.1002/2017SW001767](https://doi.org/10.1002/2017SW001767)
- Palmerio, E., Kilpua, E. K., Witasse, O., et al. 2021, *Space Weather*, 19, e2020SW002654, doi: [10.1029/2020SW002654](https://doi.org/10.1029/2020SW002654)
- Palmerio, E., Lee, C. O., Mays, M. L., et al. 2022, *Space Weather*, 20, e2021SW002993, doi: [10.1029/2021SW002993](https://doi.org/10.1029/2021SW002993)
- Palmerio, E., Lynch, B. J., Lee, C. O., et al. 2023, arXiv preprint arXiv:2309.05480, doi: [10.48550/arXiv.2309.05480](https://doi.org/10.48550/arXiv.2309.05480)
- Palmerio, E., Luhmann, J. G., Mays, M. L., et al. 2024, *Journal of Space Weather and Space Climate*, 14, 3, doi: <https://doi.org/10.1051/swsc/2024001>
- Pan, H., Gou, T., & Liu, R. 2022, *ApJ*, 937, 77, doi: [10.3847/1538-4357/ac8d64](https://doi.org/10.3847/1538-4357/ac8d64)
- Papaioannou, A., Vainio, R., Raukunen, O., et al. 2022, *Journal of Space Weather and Space Climate*, 12, 24, doi: [10.1051/swsc/2022019](https://doi.org/10.1051/swsc/2022019)
- Park, J., Innes, D., Bucik, R., Moon, Y.-J., & Kahler, S. 2015, *ApJ*, 808, 3, doi: [10.1088/0004-637X/808/1/3](https://doi.org/10.1088/0004-637X/808/1/3)
- Parker, E. N. 1958, *ApJ*, 128, 664, doi: [10.1086/146579](https://doi.org/10.1086/146579)
- . 1965, *Planetary and Space Science*, 13, 9, doi: [10.1016/0032-0633\(65\)90131-5](https://doi.org/10.1016/0032-0633(65)90131-5)
- Pesnell, W. D., Thompson, B. J., & Chamberlin, P. C. 2012, *SoPh*, 275, 3, doi: [10.1007/s11207-011-9841-3](https://doi.org/10.1007/s11207-011-9841-3)
- Petrie, G. J. 2015, *Living Reviews in Solar Physics*, 12, 1, doi: [10.1007/lrsp-2015-5](https://doi.org/10.1007/lrsp-2015-5)
- Petrosian, V. 2012, *SSRv*, 173, 535, doi: [10.1007/s11214-012-9900-6](https://doi.org/10.1007/s11214-012-9900-6)
- Pevtsov, A. A., Nandy, D., Usoskin, I., et al. 2023, *Advances in Space Research*, doi: [10.1016/j.asr.2023.08.034](https://doi.org/10.1016/j.asr.2023.08.034)
- Pierrard, V., & Lazar, M. 2010, *SoPh*, 267, 153, doi: [10.1007/s11207-010-9640-2](https://doi.org/10.1007/s11207-010-9640-2)

- Pitňa, A., Šafránková, J., Němeček, Z., Ďurovcová, T., & Kis, A. 2021, *Frontiers in Physics*, 8, 626768, doi: [10.3389/fphy.2020.626768](https://doi.org/10.3389/fphy.2020.626768)
- Plotnikov, I., Rouillard, A. P., & Share, G. H. 2017, *A&A*, 608, A43, doi: [10.1051/0004-6361/201730804](https://doi.org/10.1051/0004-6361/201730804)
- Posner, A. 2007, *Space Weather*, 5, doi: [10.1029/2006SW000268](https://doi.org/10.1029/2006SW000268)
- Powell, K. G., Roe, P. L., Linde, T. J., Gombosi, T. I., & De Zeeuw, D. L. 1999, *Journal of Computational Physics*, 154, 284, doi: [10.1006/jcph.1999.6299](https://doi.org/10.1006/jcph.1999.6299)
- Prinsloo, P., Strauss, R., & Le Roux, J. 2019, *ApJ*, 878, 144, doi: [10.3847/1538-4357/ab211b](https://doi.org/10.3847/1538-4357/ab211b)
- Qin, G., Zhang, M., & Dwyer, J. 2006, *Journal of Geophysical Research: Space Physics*, 111, doi: [10.1029/2005JA011512](https://doi.org/10.1029/2005JA011512)
- Qin, G., Zhang, M., Dwyer, J. R., & Rassoul, H. K. 2004, *ApJ*, 609, 1076, doi: [10.1086/421101](https://doi.org/10.1086/421101)
- Qin, G., Zhang, M., Dwyer, J. R., Rassoul, H. K., & Mason, G. M. 2005, *ApJ*, 627, 562, doi: [10.1086/430136](https://doi.org/10.1086/430136)
- Rankine, W. J. M. 1870, *Philosophical Transactions of the Royal Society of London*, 277, doi: [10.1098/rstl.1870.0015](https://doi.org/10.1098/rstl.1870.0015)
- Reames, D., Ng, C., & Berdichevsky, D. 2001, *ApJ*, 550, 1064, doi: [10.1086/319810](https://doi.org/10.1086/319810)
- Reames, D. V. 1999, *SSRv*, 90, 413, doi: [10.1023/A:1005105831781](https://doi.org/10.1023/A:1005105831781)
- . 2013, *SSRv*, 175, 53, doi: [10.1007/s11214-013-9958-9](https://doi.org/10.1007/s11214-013-9958-9)
- . 2021, *Solar Energetic Particles: A Modern Primer on Understanding Sources, Acceleration and Propagation* (Springer Nature), doi: [10.1007/978-3-030-66402-2](https://doi.org/10.1007/978-3-030-66402-2)
- Reiss, M. A., Arge, C. N., Henney, C. J., et al. 2023, *Advances in Space Research*, doi: [10.1016/j.asr.2023.08.039](https://doi.org/10.1016/j.asr.2023.08.039)
- Richardson, I., Mays, M., & Thompson, B. 2018, *Space Weather*, 16, 1862, doi: [10.1029/2018SW002032](https://doi.org/10.1029/2018SW002032)
- Richardson, I., Von Rosenvinge, T., Cane, H., et al. 2014, *Coronal Magnetometry*, 437, doi: [10.1007/978-1-4939-2038-9\\_27](https://doi.org/10.1007/978-1-4939-2038-9_27)
- Rodriguez, L., Masías-Meza, J. J., Dasso, S., et al. 2016, *SoPh*, 291, 2145, doi: [10.1007/s11207-016-0955-5](https://doi.org/10.1007/s11207-016-0955-5)
- Roelof, E. 1969, *Lectures in High-Energy Astrophysics*, 111, <https://ntrs.nasa.gov/citations/19690020274>
- Rouillard, A., Odstre, D., Sheeley, N., et al. 2011, *ApJ*, 735, 7, doi: [10.1088/0004-637X/735/1/7](https://doi.org/10.1088/0004-637X/735/1/7)
- Rouillard, A. P., Plotnikov, I., Pinto, R. F., et al. 2016, *ApJ*, 833, 45, doi: [10.3847/1538-4357/833/1/45](https://doi.org/10.3847/1538-4357/833/1/45)
- Roussev, I. I., Forbes, T. G., Gombosi, T. I., et al. 2003, *ApJ*, 588, L45, doi: [10.1086/375442](https://doi.org/10.1086/375442)
- Sachdeva, N., van Der Holst, B., Manchester, W. B., et al. 2019, *ApJ*, 887, 83, doi: [10.3847/1538-4357/ab4f5e](https://doi.org/10.3847/1538-4357/ab4f5e)
- Sachdeva, N., Tóth, G., Manchester, W. B., et al. 2021, *ApJ*, 923, 176, doi: [10.3847/1538-4357/ac307c](https://doi.org/10.3847/1538-4357/ac307c)
- Sachdeva, N., Manchester IV, W. B., Sokolov, I., et al. 2023, *ApJ*, 952, 117, doi: [10.3847/1538-4357/acda87](https://doi.org/10.3847/1538-4357/acda87)
- Sandroos, A., & Vainio, R. 2007, *ApJ*, 662, L127, doi: [10.1086/519378](https://doi.org/10.1086/519378)
- Schatten, K. H., Wilcox, J. M., & Ness, N. F. 1969, *SoPh*, 6, 442, doi: [10.1007/BF00146478](https://doi.org/10.1007/BF00146478)
- Schmelz, J., Reames, D., Von Steiger, R., & Basu, S. 2012, *ApJ*, 755, 33, doi: [10.1088/0004-637X/755/1/33](https://doi.org/10.1088/0004-637X/755/1/33)
- Sellers, F. B., & Hanser, F. A. 1996, in *GOES-8 and Beyond*, Vol. 2812, SPIE, 353–364, doi: [10.1117/12.254083](https://doi.org/10.1117/12.254083)
- Shalchi, A. 2019, *Advances in Space Research*, 64, 2426, doi: [10.1016/j.asr.2019.03.005](https://doi.org/10.1016/j.asr.2019.03.005)
- . 2020, *SSRv*, 216, 23, doi: [10.1007/s11214-020-0644-4](https://doi.org/10.1007/s11214-020-0644-4)
- . 2021, *Physics of Plasmas*, 28, doi: [10.1063/5.0061485](https://doi.org/10.1063/5.0061485)
- Shalchi, A., Škoda, T., Tautz, R., & Schlickeiser, R. 2009, *A&A*, 507, 589, doi: [10.1051/0004-6361/200912755](https://doi.org/10.1051/0004-6361/200912755)
- Shen, F., Feng, X., Wu, S., Xiang, C., & Song, W. 2011, *Journal of Geophysical Research: Space Physics*, 116, doi: [10.1029/2010JA015809](https://doi.org/10.1029/2010JA015809)
- Shen, F., Shen, C., Xu, M., et al. 2022, *Reviews of Modern Plasma Physics*, 6, 8, doi: [10.1007/s41614-022-00069-1](https://doi.org/10.1007/s41614-022-00069-1)
- Shi, T., Manchester IV, W., Landi, E., et al. 2022, *ApJ*, 928, 34, doi: [10.3847/1538-4357/ac52ab](https://doi.org/10.3847/1538-4357/ac52ab)
- Shiota, D., & Kataoka, R. 2016, *Space Weather*, 14, 56, doi: [10.1002/2015SW001308](https://doi.org/10.1002/2015SW001308)



- Shoda, M., Chandran, B. D., & Cranmer, S. R. 2021, *ApJ*, 915, 52, doi: [10.3847/1538-4357/abfdbbc](https://doi.org/10.3847/1538-4357/abfdbbc)
- Sime, D., & Hundhausen, A. 1987, *Journal of Geophysical Research: Space Physics*, 92, 1049, doi: [10.1029/JA092iA02p01049](https://doi.org/10.1029/JA092iA02p01049)
- Skilling, J. 1971, *ApJ*, 170, 265, doi: [10.1086/151210](https://doi.org/10.1086/151210)
- Smith, Z., & Dryer, M. 1990, *SoPh*, 129, 387, doi: [10.1007/BF00159049](https://doi.org/10.1007/BF00159049)
- Sokolov, I. V., & Gombosi, T. I. 2023, *ApJ*, 955, 126, doi: [10.3847/1538-4357/aceef5](https://doi.org/10.3847/1538-4357/aceef5)
- Sokolov, I. V., Powell, K. G., Gombosi, T. I., & Roussev, I. I. 2006a, *Journal of Computational Physics*, 220, 1, doi: [10.1016/j.jcp.2006.07.021](https://doi.org/10.1016/j.jcp.2006.07.021)
- Sokolov, I. V., Roussev, I., Fisk, L., et al. 2006b, *ApJ*, 642, L81, doi: [10.1086/504406](https://doi.org/10.1086/504406)
- Sokolov, I. V., Roussev, I., Gombosi, T., et al. 2004, *ApJ*, 616, L171, doi: [10.1086/426812](https://doi.org/10.1086/426812)
- Sokolov, I. V., Roussev, I. I., Skender, M., Gombosi, T. I., & Usmanov, A. V. 2009, *ApJ*, 696, 261, doi: [10.1088/0004-637X/696/1/261](https://doi.org/10.1088/0004-637X/696/1/261)
- Sokolov, I. V., Sun, H., Tóth, G., et al. 2019, arXiv preprint arXiv:1910.12636v1, doi: [10.48550/arXiv.1910.12636v1](https://doi.org/10.48550/arXiv.1910.12636v1)
- Sokolov, I. V., Zhao, L., & Gombosi, T. I. 2022, *ApJ*, 926, 102, doi: [10.3847/1538-4357/ac400f](https://doi.org/10.3847/1538-4357/ac400f)
- Sokolov, I. V., van der Holst, B., Oran, R., et al. 2013, *ApJ*, 764, 23, doi: [10.1088/0004-637X/764/1/23](https://doi.org/10.1088/0004-637X/764/1/23)
- Sokolov, I. V., van der Holst, B., Manchester, W. B., et al. 2021, *ApJ*, 908, 172, doi: [10.3847/1538-4357/abc000](https://doi.org/10.3847/1538-4357/abc000)
- Sokolov, I. V., Sun, H., Tóth, G., et al. 2023, *Journal of Computational Physics*, 476, 111923, doi: [10.1016/j.jcp.2023.111923](https://doi.org/10.1016/j.jcp.2023.111923)
- Stone, E. C., Frandsen, A., Mewaldt, R., et al. 1998, *SSRv*, 86, 1, doi: [10.1023/A:1005082526237](https://doi.org/10.1023/A:1005082526237)
- Strang, G. 1968, *SIAM journal on numerical analysis*, 5, 506, doi: [10.1137/0705041](https://doi.org/10.1137/0705041)
- Strauss, R., & Fichtner, H. 2015, *ApJ*, 801, 29, doi: [10.1088/0004-637X/801/1/29](https://doi.org/10.1088/0004-637X/801/1/29)
- Strauss, R., & Le Roux, J. 2019, *ApJ*, 872, 125, doi: [10.3847/1538-4357/aafe02](https://doi.org/10.3847/1538-4357/aafe02)
- Tao, X., Shen, F., Wei, W., et al. 2024, *A&A*, 682, A82, doi: [10.1051/0004-6361/202347248](https://doi.org/10.1051/0004-6361/202347248)
- Tenishev, V., Shou, Y., Borovikov, D., et al. 2021, *Journal of Geophysical Research: Space Physics*, 126, e2020JA028242, doi: [10.1029/2020JA028242](https://doi.org/10.1029/2020JA028242)
- Tenishev, V., Zhao, L., & Sokolov, I. 2022, arXiv preprint arXiv:2209.09346, doi: [10.48550/arXiv.2209.09346](https://doi.org/10.48550/arXiv.2209.09346)
- Thompson, W. T., Davila, J. M., Fisher, R. R., et al. 2003, in *Innovative Telescopes and Instrumentation for Solar Astrophysics*, Vol. 4853, SPIE, 1–11, doi: [10.1117/12.460267](https://doi.org/10.1117/12.460267)
- Titov, V., Török, T., Mikic, Z., & Linker, J. A. 2014, *ApJ*, 790, 163, doi: [10.1088/0004-637X/790/2/163](https://doi.org/10.1088/0004-637X/790/2/163)
- Titov, V. S., & Démoulin, P. 1999, *A&A*, 351, 707
- Titov, V. S., Downs, C., Török, T., & Linker, J. A. 2022, *ApJ*, 936, 121, doi: [10.3847/1538-4357/ac874e](https://doi.org/10.3847/1538-4357/ac874e)
- Török, T., Downs, C., Linker, J. A., et al. 2018, *ApJ*, 856, 75, doi: [10.3847/1538-4357/aab36d](https://doi.org/10.3847/1538-4357/aab36d)
- Torsti, J., Valtonen, E., Lumme, M., et al. 1995, *SoPh*, 162, 505, doi: [10.1007/BF00733438](https://doi.org/10.1007/BF00733438)
- Tóth, G. 2023, *Journal of Computational Physics*, 494, 112534, doi: [10.1016/j.jcp.2023.112534](https://doi.org/10.1016/j.jcp.2023.112534)
- Tóth, G., van der Holst, B., & Huang, Z. 2011, *ApJ*, 732, 102, doi: [10.1088/0004-637X/732/2/102](https://doi.org/10.1088/0004-637X/732/2/102)
- Tóth, G., Sokolov, I. V., Gombosi, T. I., et al. 2005, *Journal of Geophysical Research: Space Physics*, 110, doi: [10.1029/2005JA011126](https://doi.org/10.1029/2005JA011126)
- Tóth, G., van der Holst, B., Sokolov, I. V., et al. 2012, *Journal of Computational Physics*, 231, 870, doi: [10.1016/j.jcp.2011.02.006](https://doi.org/10.1016/j.jcp.2011.02.006)
- Tylka, A., Cohen, C., Dietrich, W., et al. 2005, *ApJ*, 625, 474, doi: [10.1086/429384](https://doi.org/10.1086/429384)
- Tylka, A. J., Reames, D. V., & Ng, C. K. 1999, *Geophys. Res. Lett.*, 26, 2141, doi: [10.1029/1999GL900458](https://doi.org/10.1029/1999GL900458)
- Valtonen, E., Peltonen, J., Peltonen, P., et al. 1997, *Nuclear Instruments and Methods in Physics Research Section A: Accelerators, Spectrometers, Detectors and Associated Equipment*, 391, 249, doi: [10.1016/S0168-9002\(97\)00469-5](https://doi.org/10.1016/S0168-9002(97)00469-5)
- van den Berg, J., Strauss, D. T., & Effenberger, F. 2020, *SSRv*, 216, 146, doi: [10.1007/s11214-020-00771-x](https://doi.org/10.1007/s11214-020-00771-x)
- van der Holst, B., Manchester, W., Frazin, R., et al. 2010, *ApJ*, 725, 1373, doi: [10.1088/0004-637X/725/1/1373](https://doi.org/10.1088/0004-637X/725/1/1373)

- van der Holst, B., Manchester, W., Sokolov, I., et al. 2009, *ApJ*, 693, 1178, doi: [10.1088/0004-637X/693/2/1178](https://doi.org/10.1088/0004-637X/693/2/1178)
- van der Holst, B., Manchester IV, W., Klein, K., & Kasper, J. 2019, *ApJL*, 872, L18, doi: [10.3847/2041-8213/ab04a5](https://doi.org/10.3847/2041-8213/ab04a5)
- van der Holst, B., Sokolov, I. V., Meng, X., et al. 2014, *ApJ*, 782, 81, doi: [10.1088/0004-637X/782/2/81](https://doi.org/10.1088/0004-637X/782/2/81)
- van der Holst, B., Tóth, G., Sokolov, I. V., et al. 2011, *ApJS*, 194, 23, doi: [10.1088/0067-0049/194/2/23](https://doi.org/10.1088/0067-0049/194/2/23)
- van der Holst, B., Huang, J., Sachdeva, N., et al. 2022, *ApJ*, 925, 146, doi: [10.3847/1538-4357/ac3d34](https://doi.org/10.3847/1538-4357/ac3d34)
- Vemareddy, P., & Mishra, W. 2015, *ApJ*, 814, 59, doi: [10.1088/0004-637X/814/1/59](https://doi.org/10.1088/0004-637X/814/1/59)
- Verkhoglyadova, O. P., Zank, G. P., & Li, G. 2015, *Physics Reports*, 557, 1, doi: [10.1016/j.physrep.2014.10.004](https://doi.org/10.1016/j.physrep.2014.10.004)
- Von Roseninge, T., Reames, D., Baker, R., et al. 2008, *The STEREO Mission*, 391, doi: [10.1007/978-0-387-09649-0\\_14](https://doi.org/10.1007/978-0-387-09649-0_14)
- Vourlidas, A., Wu, S., Wang, A., Subramanian, P., & Howard, R. 2003, *ApJ*, 598, 1392, doi: [10.1086/379098](https://doi.org/10.1086/379098)
- Vourlidas, A., Turner, D., Biesecker, D., et al. 2023, *Advances in Space Research*, doi: [10.1016/j.asr.2023.06.046](https://doi.org/10.1016/j.asr.2023.06.046)
- Wang, Y., & Guo, J. 2024, *A&A*, 691, A54, doi: [10.1051/0004-6361/202450046](https://doi.org/10.1051/0004-6361/202450046)
- Wang, Y., & Qin, G. 2015, *ApJ*, 806, 252, doi: [10.1088/0004-637X/806/2/252](https://doi.org/10.1088/0004-637X/806/2/252)
- Webb, D. F., & Howard, T. A. 2012, *Living Reviews in Solar Physics*, 9, 1, doi: [10.12942/lrsp-2012-3](https://doi.org/10.12942/lrsp-2012-3)
- Wei, W., Shen, F., Yang, Z., et al. 2019, *Journal of Atmospheric and Solar-Terrestrial Physics*, 182, 155, doi: [10.1016/j.jastp.2018.11.012](https://doi.org/10.1016/j.jastp.2018.11.012)
- Whitman, K., Egeland, R., Richardson, I. G., et al. 2023, *Advances in Space Research*, 72, 5161, doi: [10.1016/j.asr.2022.08.006](https://doi.org/10.1016/j.asr.2022.08.006)
- Wijsen, N., Aran, A., Pomoell, J., & Poedts, S. 2019, *A&A*, 622, A28, doi: [10.1051/0004-6361/201833958](https://doi.org/10.1051/0004-6361/201833958)
- Wijsen, N., Li, G., Ding, Z., et al. 2023a, *Journal of Geophysical Research: Space Physics*, 128, e2022JA031203, doi: [10.1029/2022JA031203](https://doi.org/10.1029/2022JA031203)
- Wijsen, N., Samara, E., Aran, À., et al. 2021, *ApJL*, 908, L26, doi: [10.3847/2041-8213/abe1cb](https://doi.org/10.3847/2041-8213/abe1cb)
- Wijsen, N., Lario, D., Sánchez-Cano, B., et al. 2023b, *ApJ*, 950, 172, doi: [10.3847/1538-4357/acd1ed](https://doi.org/10.3847/1538-4357/acd1ed)
- Wraback, E., Hoffmann, A., Manchester, W., et al. 2024, *ApJ*, 962, 182, doi: [10.3847/1538-4357/ad21fd](https://doi.org/10.3847/1538-4357/ad21fd)
- Wuelser, J.-P., Lemen, J. R., Tarbell, T. D., et al. 2004, in *Telescopes and instrumentation for solar astrophysics*, Vol. 5171, SPIE, 111–122, doi: [10.1117/12.506877](https://doi.org/10.1117/12.506877)
- Xapsos, M., Stauffer, C., Jordan, T., Barth, J., & Mewaldt, R. 2007, *IEEE Transactions on Nuclear Science*, 54, 1985, doi: [10.1109/TNS.2007.910850](https://doi.org/10.1109/TNS.2007.910850)
- Xie, H., St. Cyr, O., Mäkelä, P., & Gopalswamy, N. 2019, *Journal of Geophysical Research: Space Physics*, 124, 6384, doi: [10.1029/2019JA026832](https://doi.org/10.1029/2019JA026832)
- Yashiro, S., Gopalswamy, N., Michalek, G., et al. 2004, *Journal of Geophysical Research: Space Physics*, 109, doi: [10.1029/2003JA010282](https://doi.org/10.1029/2003JA010282)
- Young, M. A., Schwadron, N. A., Gorby, M., et al. 2021, *ApJ*, 909, 160, doi: [10.3847/1538-4357/abdf5f](https://doi.org/10.3847/1538-4357/abdf5f)
- Yu, F., Kong, X., Guo, F., et al. 2022, *ApJL*, 925, L13, doi: [10.3847/2041-8213/ac4cb3](https://doi.org/10.3847/2041-8213/ac4cb3)
- Zakharov, V. E., L'vov, V. S., & Falkovich, G. 2012, *Kolmogorov Spectra of Turbulence I: Wave Turbulence* (Springer Science & Business Media), doi: [10.1007/978-3-642-50052-7](https://doi.org/10.1007/978-3-642-50052-7)
- Zank, G., Le Roux, J., Webb, G., Dosch, A., & Khabarova, O. 2014, *ApJ*, 797, 28, doi: [10.1088/0004-637X/797/1/28](https://doi.org/10.1088/0004-637X/797/1/28)
- Zank, G., Li, G., & Verkhoglyadova, O. 2007, *SSRv*, 130, 255, doi: [10.1007/s11214-007-9214-2](https://doi.org/10.1007/s11214-007-9214-2)
- Zank, G., Rice, W., & Wu, C. 2000, *Journal of Geophysical Research: Space Physics*, 105, 25079, doi: [10.1029/1999JA000455](https://doi.org/10.1029/1999JA000455)
- Zhang, M., Cheng, L., Zhang, J., et al. 2023, *ApJS*, 266, 35, doi: [10.3847/1538-4365/accb8e](https://doi.org/10.3847/1538-4365/accb8e)
- Zhang, M., Qin, G., & Rassoul, H. 2009, *ApJ*, 692, 109, doi: [10.1088/0004-637X/692/1/109](https://doi.org/10.1088/0004-637X/692/1/109)
- Zhang, M., & Zhao, L. 2017, *ApJ*, 846, 107, doi: [10.3847/1538-4357/aa86a8](https://doi.org/10.3847/1538-4357/aa86a8)
- Zhao, L. 2023, arXiv preprint arXiv:2310.14677, doi: [10.48550/arXiv.2310.14677](https://doi.org/10.48550/arXiv.2310.14677)
- Zhao, L., Li, G., Ebert, R., et al. 2016a, *Journal of Geophysical Research: Space Physics*, 121, 77, doi: [10.1002/2015JA021762](https://doi.org/10.1002/2015JA021762)
- Zhao, L., Li, G., Zhang, M., et al. 2019, *ApJ*, 878, 107, doi: [10.3847/1538-4357/ab2041](https://doi.org/10.3847/1538-4357/ab2041)

- Zhao, L., Zhang, M., & Rassoul, H. K. 2016b, ApJ, 821, 62, doi: [10.3847/0004-637X/821/1/62](https://doi.org/10.3847/0004-637X/821/1/62)
- . 2017, ApJ, 836, 31, doi: [10.3847/1538-4357/836/1/31](https://doi.org/10.3847/1538-4357/836/1/31)
- Zhao, L., Sokolov, I., Gombosi, T., et al. 2024, Space Weather, 22, e2023SW003729, doi: [10.1029/2023SW003729](https://doi.org/10.1029/2023SW003729)
- Zheng, Y., Ganushkina, N. Y., Jiggins, P., et al. 2019, Space Weather, 17, 1384, doi: [10.1029/2018SW002042](https://doi.org/10.1029/2018SW002042)
- Zheng, Y., Jun, I., Tu, W., et al. 2024, Advances in Space Research, doi: [10.1016/j.asr.2024.05.017](https://doi.org/10.1016/j.asr.2024.05.017)
- Zhong, Y., Wang, Y., & Qin, G. 2024, ApJ, 974, 228, doi: [10.3847/1538-4357/ad70aa](https://doi.org/10.3847/1538-4357/ad70aa)
- Zhu, Y., & Shen, F. 2024, Universe, 10, 315, doi: [10.3390/universe10080315](https://doi.org/10.3390/universe10080315)
- Zhuang, B., Lugaz, N., Gou, T., & Ding, L. 2021, ApJ, 921, 6, doi: [10.3847/1538-4357/ac17e9](https://doi.org/10.3847/1538-4357/ac17e9)